Carotenoids and their role in the non-photochemical quenching of higher plants

by

Kieran Francis Fox

Submitted in partial fulfillment of the requirements

of the Degree of Doctor of Philosophy

May 2, 2019

Acknowledgments

I hereby acknowledge the following

Biotechnology and Biological Sciences Research Council for providing the funding for what I hope has been useful and impactful work.

Queen Mary University of London for providing a welcoming and supportive place of work.

My many colleagues and collaborators who have been crucial to my progress during my PhD. In particular Vytas, who has been patient with me and inspiring to work with. I will happily look back on many chats in sunny pub gardens and hope for many more in the future.

My supervisor for being a friend and mentor for four of the most enjoyable and fulfilling years of my life. You have provided me with support and advice at every turn and have gone above and beyond to help me grow as a scientist. Above all though I thank you for keeping my joy in science alive and well, and for the smile on my face as I walked into work ~~almost~~ every morning. My good friend Chris, I hope we will always be able to laugh together over stories of our exploits.

My parents for feeding my curiosity and sparking my love of science. I still remember sitting on a hotel bed, hearing about the forces which govern our universe, or crouching in the back garden and being shown the amazing relationship between ants and aphids displayed in front of me. To an impressionable young boy, having parents who where fascinated in the world around them was invaluable and I will forever be grateful for the time you spent instilling that passion into me.

Statement of Originality

I, Kieran Fox, confirm that the research included within this thesis is my own work or that where it has been carried out in collaboration with, or supported by others, that this is duly acknowledged below and my contribution indicated. Previously published material is also acknowledged below.

I attest that I have exercised reasonable care to ensure that the work is original, and does not to the best of my knowledge break any UK law, infringe any third party's copyright or other Intellectual Property Right, or contain any confidential material.

I accept that the College has the right to use plagiarism detection software to check the electronic version of the thesis.

I confirm that this thesis has not been previously submitted for the award of a degree by this or any other university.

Signature:

Date: May 2, 2019

Details of collaboration and publications:

1. Distortions of the xanthophylls caused by interactions with neighboring pigments and the LHCII protein are crucial for studying energy transfer pathways within the complex, K. F. Fox, W. P. Bricker, C. Lo, C. D. P. Duffy, *The Journal of Physical Chemistry B*, 2015, **119**, 15550-15560

2. The carotenoid pathway: what is important for excitation quenching in plant antenna complexes?, K. F. Fox, V. Balevičius, J. Chmeliov, L. Valkunas, A. V. Ruban, C. D. P. Duffy, *Physical Chemistry Chemical Physics*, 2017, **19**, 22957-22968

3. Fine control of chlorophyll-carotenoid interactions defines the functionality of light-harvesting proteins in plants, V. Balevičius, K. F. Fox, W. P. Bricker, S. Jurinovich, I. G. Prandi, B.

Mennucci, C. D. P. Duffy, *Scientific Reports*, 2017, **7**, 13956

4. A possible molecular basis for photoprotection in the minor antenna proteins of plants, K. F. Fox, C. Ünlü, V. Balevičius, B. N. Ramdour, C. Kern, X. Pan, M. Li, H. van Amerongen, C. D. P. Duffy, *Biochimica et Biophysica Acta Bioenergetics*, 2018, **1859**, 471-481

Abstract

Photosynthesis drives the majority of life on earth. It involves the conversion of light energy into stable chemical energy which can be used to fuel metabolic processes. The bioenergetics of light capture have been well characterised but this neglects the essential regulatory processes which deal with excesses in absorbed energy. Central to these is non-photochemical quenching which is the dissipation of excited state energy as heat. There have been many proposed models for how this occurs and how it balances with efficient photosynthetic turnover, most of which are contradictory and involve essentially the same experimental observations. The photosynthetic membrane must be able to quench energy when rate of absorption exceeds turnover rate at the reaction centre but reduce this mechanism when light is in lower supply. The main points of contention are the site of quenching within the photosynthetic membrane, the nature of the quencher and the switch mechanism. In this thesis I have formulated a simple model to explain this mechanism. I show how slow energy transfer to the naturally dissipative Cars, present throughout the membrane, is sufficient for deep quenching. I also propose, with some theoretical evidence, that small changes in the mutual orientation of pigments can have significant effects of the energetic pathways. These are potentially responsible for the switch between light-harvesting and dissipative states.

Contents

0.1 Aims

The processes of photosynthesis are generally well characterised through decades of research. However, the same cannot be said for non-photochemical quenching, which is at the heart of the protective mechanism for photosynthetic machinery. There is a very limited pool of knowledge which is generally agreed upon. Beyond that, there are almost as many models to explain this phenomenon as lab groups which study it. Details of the most pertinent parameters involved are discussed in Chapter 1 (along with some general background of the photosynthetic processes which surround it) and at the start of Chapter 6. My own investigation makes use of quantum chemistry to investigate the relationship between pigments within the light harvesting complexes of plants. I then use some theories of open-quantum systems to model the dynamics of excited state energy across each pigment. The details of these theories can be found in chapters 2 and 3 respectively. By observing how the probability of excitation for each pigment (or site) changes over time in my model, I am able to gain some understanding of how the excited state energy might evolve and be dissipated in the *in vivo* environments. My preliminary calculations can be found in chapter 5 which I use to construct my model in chapter 6. This research centres around the novel way in which I employ quantum chemistry to characterise the particularly interesting electronic states of a key photosynthetic class of pigment: the carotenoid. This peculiar molecule is the major cause of any lack of understand in the field and this is explained in chapter 4.

A full explanation of non-photochemical quenching (NPQ) is beyond the scope of this thesis but I hope to give some evidence for certain aspects as well as construct a general theory for the most important principles. In order to gain a better understanding of NPQ I will attempt to make the most complete and advanced model of the key pigment protein complexes yet. This includes advances on the field in quantum chemistry to create the structures and determine the wavefunctions. I will also look towards a more realistic set of parameters to define the pigments involved (including excitation energy and spectral density). It is very difficult to give any definitive answers into the NPQ mechanism for reasons I shall discuss throughout this thesis but by testing the limits of my model, I hope to gain some understanding on the most important factors and give some direction into further research to find the hidden answers to this intricate mechanism.

Chapter 1

Biological introduction

1.1 Photosynthesis

Photosynthesis is simply the synthesis of chemical compounds using light energy. However, this definition is broad and a more specific definition shall be defined for the purposes of this thesis.

> The conversion of free light energy into chemical energy by organisms for use in respiratory processes.

This process is the foundation for almost all life on earth and although there is some variation in how it is done, in the vast majority of cases it is performed with many similarities. The first consistency lies in the absorption of sun light as excited state energy, by a variety of pigments. While some Bacteria and Archae use proteins such as rhodopsin, the dominant pigment is chlorophyll (Chl). Light from the sun is emitted as a wide spectrum but is not consistent across the wavelengths. It is essentially black body radiation with certain absorption bands from molecules in the atmosphere. High energy ultra-violet light is mostly absorbed by ozone in the upper atmosphere leaving a spectrum stretching from around 400 nm to the lower energies. The visible section spans from 400 nm to 700 nm and accounts for the highest energy photons available to photosynthetic organisms on earth. It therefore accounts for the bulk of photosynthetic activity but there is still significant energy absorption in the lower wavelength infra-red, up to around 1000 nm, although at this point the energy of the photons is too low for most organisms

to generate useful chemical energy. Chl absorbs in the range 400 nm to 700 nm which is often called the photosynthetically active region (PAR). In addition to Chls there are a number of other absorbing molecules including carotenoids (Cars) and open tetrapyrrole bilin pigments. These often absorb in the regions that Chl does not such as green light and below the PAR. Sunlight is also inconsistent on a temporal axis and can vary in different environments and this is often reflected in pigment composition. Under water, much of the red light is absorbed by water molecules and the high energy blue light is scattered (scattering is proportional to the wavelength to the fourth power[1]). The missing energy wavelengths are the primary absorbing regions of Chl, leaving the mid-energy green as the dominant light. For this reason underwater photosynthetic organisms often contain a large number of green absorbing Cars such as peridinin (Per) and fucoxanthin.

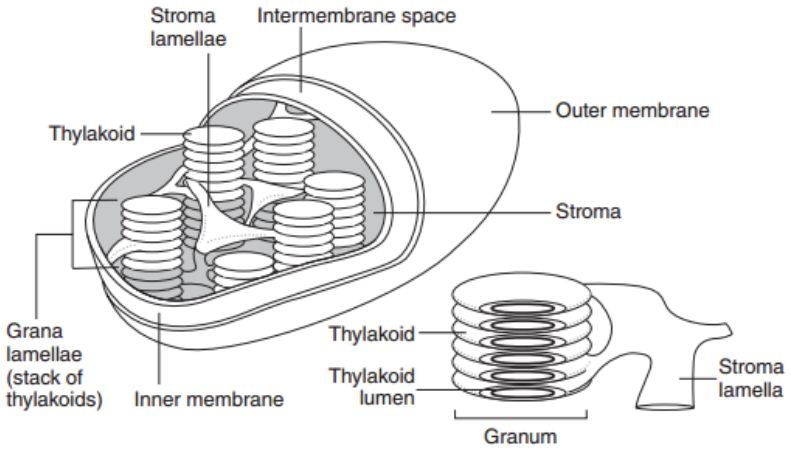

Figure 1.1: A schematic drawing of a chloroplast[2]. It allows us to see the stacked thylakoid membranes as well as the stroma lamallae which connects them.

The majority of the photosynthetic process, from the absorption of light energy to the conversion of this energy to chemical change on the molecular level and subsequent stabilisation, occurs in lipid bi-layers, making photosynthesis a primarily membrane based process. Subsequent formation of carbon based molecules happens in aqueous solution away from the membrane. In prokaryotic organisms, specialized membranes originating from the cyctoplasmic membrane are used for the primary processes and carbon compound formation happens in the cell cytoplasm. Eukaryotic organisms use special organelles called chloroplasts (figure 1.1) to contain this entire

process. Chloroplasts are mostly self contained, bacteria sized subsections of the cells and in fact descend from separate bacteria which formed symbiotic relationships with the larger organisms they resided in. Over time, these organisms joined to form one, in a process called endosymbiosis. The chloroplast contains thylakoid membranes, used for the primary processes of photosynthesis. Thylakoid membranes floating in the chloroplast cytoplasm (Stroma) are called stromal thylakoid membranes but in higher plants they are arranged in stacks called grana. The stacks are then connected by unstacked membranes called stroma lamallae.

1.1.1 The four stages of photosynthesis

The process of photosynthesis can be separated into four phases. The first of which is absorption of light energy and the delivery of the subsequent excited state energy to a reaction centre (RC). The RC is a specific arrangement of pigments with the key component being the 'special pair' of Chls. These are arranged in a specific way to form a dimer and only differ from a large number of other 'antenna' Chls spread out across the membrane, by the environment they reside in. The relatively dilute photon yield in sunlight when reaching the earth's surface[2] means that photon capture is a priority. In order to maximize this, each RC will have an antenna of various proteins[3], each filled with a range of pigments. The size of the antenna is determined by the light quality for each species and organism. The antenna forms a spatial funnel to transfer excited state energy to the RC achieved by an energetic downward slope of varying steepness. A more in depth discussion of this stage is provided in section 1.3 below. While there is a wide array of antenna across the many different photosynthetic organisms, the general structure of a protein containing light harvesting pigments, connected to a RC is always the same

The second is the conversion of the excited state energy absorbed by, or more often delivered to, the RC. RCs are always pigment proteins spanning a membrane containing a variety of non-covalently bound molecules (in most organisms this includes the special pair of Chls) where 'charge separation' occurs. As one of the dimer Chls is excited, it becomes a reducing agent as the redox potential of excited states can vary greatly from the ground. It then donates an electron to a nearby acceptor molecule, resulting in a positive charge on the Chl and a negative charge on the acceptor. This charge separation is the primary reaction and uses the conversion of excited

state energy into redox potential to start a chain of processes, leading towards useful chemical energy storage. At this point there is a danger of the electron taking the most thermodynamically accessible route of transferring back to its original Chl (charge recombination), where it would undergo rapid dissipation as heat. This would be disastrous for the organism as it would lose any energy it had captured from the original photon.

It is avoided by the third stage of photosynthesis. A series of 'secondary reactions' which involves the transfer of the electron, not back to the Chl, but to a subsequent set of molecules via kinetically favourable routes. The kinetics almost completely out-compete the thermodynamics of the recombination pathway and the charge separation is spatially increased to roughly the width of the membrane, at which point the redox energy is much more stable. This increased separation is the first stage of the electron transport chain (ETC) and varies across the gamut of photosynthetic organisms. The resulting charge may either re-reduce the original Chl in certain bacteria, or reach Nicotinamide Adenine Dinucleotide Phosphate$^+$ ($NADP^+$) at the end of the ETC, where it is converted to NADPH, a basic unit reduction power used in various metabolic processes. Part of the ETC involves the formation of H^+ ions which are localised on one side of the thylakoid membrane. This generates a proton motive force which is used by a final membrane protein ATP synthase, to generate adenesine tri-phosphate (ATP) as the basic unit block of energy. This entire process sacrifices much of the energy absorbed to give a high quantum yield of photons absorbed to products formed, often close to 1.0[2].

The set of secondary reactions described has much variation. Some bacteria use a cyclic ETC in which the donated electron is transported through a series of carriers to donor molecule which donates the electron back to the original Chl. In this case, only the protomotive force is used for ATP synthase and the redox potential is lost. The electron transport chain constitutes the most significant variations in the photosynthetic process, even amongst non-cyclic ETCs.

The fourth and final process is slower as the energy is now in a more stable state of ATP. Here carbon from CO_2 or more complicated carbon compounds is used to make sugars. This is done with a variety of different cycles in different organisms but the result is always the carbon compounds used by the organism for respiration. It is often termed the dark stage while the others are the light stages.

1.1.2 Photosynthetic organisms

A number of different organisms photosynthesise and each has variations in the light harvesting structure (antenna), the electron donor at the RC, the electron transport chain and the carbon source. Dispite this variation, they can be grouped in terms of their evolutionary ancestry using analysis of the RNA. This results in three basic groups: Archaea, Bacteria and Eukarya. There have, as of yet, been no species belonging to the group Archaea which use Chl for photosynthesis and so Eukarya (and to a lesser extent bacteria) will be the focus here. Using variations in the process of photosynthesis, Bacteria can be split into six categories[4, 5]. Five of which are anoxygenic: purple bacteria, green sulfur bacteria, filamentous anoxygenic phototrophs, helio bacteria and chloroacido bacteria[6], meaning they don't use H_2O as the primary electron donor. Instead they typically use sulfur containing compounds such as H_2S. They also gain carbon from a variety of carbon compounds such as pyruvate as well as CO_2. When they do use CO_2, some use the Calvin-Benson cycle, while others fix using the reverse tricarboxylic acid cycle or hydroxypropionate pathways. The size of antenna varies widely, with green sulfur bacteria having the largest due to their underwater habitat while the most simple photosynthetic organisms: heliobactera, having almost no antenna at all. The light quality in their environment also dictates the pigment composition with bacteriochlorophyll (BChl) a to g all present in certain species and Chl *a* rarely found.

Anoxygenic organisms typically do not use the donated electron in the transport chain to reduce NADP+ to NADPH but instead use the energy from the excited state and subsequent redox potential to create a proton gradient[2]. The most well characterized process and a good representative is that of the purple bacteria[7]. Here the proteins span the intra cytoplasmic membrane in invaginated vescicles. This creates pockets of periplasmic cytoplasm contained by the outer cyctoplasmic membrane. The excited Chl pair transfers its electron to a nearby accessory BChl . At this point there is rapid transport to a nearby BPhy and subsequently to a quinone *a* (Q*a*) and eventually to a final quinone *b* (Q*b*). Each stage of this transport happens slower than the last as the charge separation becomes more stable. The rate of transfer is always roughly 50× faster[7] than the reverse (leading to recombination). Quinone can be reduced twice and at Q*b* the charge separation is stable enough to wait for a second electron to

be delivered through the chain. The RC is re-reduced for this by electron donation originating from the cytochrome c_2 (Cyt c_2) at the same time as electron transfer from Qa to Qb occurs. The electron is transported to the special pair through a series of four hemes. Protons are delivered to the reduced Qb, from the periplasmic space, by a chain of protonatable amino acid residues. When Qb is fully reduced to neutral ubiquinole, it is released into the hydrocarbon portion of the membrane and is replaced by an oxidised quinol. This is how the proton gradient, used for the production of ATP, is formed. The overall reaction is given by equation 1.1

$$2\,\mathrm{Cyt_2(red)} + \mathrm{UQ} + 2\,\mathrm{H^+} + 2\,\mathrm{h}\nu \longrightarrow 2\,\mathrm{Cyt_2(ox)} + \mathrm{UQH_2} \tag{1.1}$$

electrons are then transported back across the membrane through the Cyt bc_1 complex to re-reduce Cyt c_2, creating the cyclic electron transport chain. Other anoxygenic bacteria use a very similar process, with changes to the pigments and protein structure.

Cyano bacteria is the final, sixth group of bacterial photosynthetic organisms[8]. It is the closest in the bacteria division to plant photosynthesis, with the vast majority using H_2O as the electron source and CO_2 for carbon. This makes cyano bacteria the only oxygenic prokaryotic organisms. The primary photon absorbing pigment is Chl a and phycobiliproteins found in antenna structures called phycobilisomes.

Eukayotic photosynthetic organisms consist of algae, with red and green algae being the main two types, as well as plants which can be divided up into vascular (trees, flower plants etc) and non-vascular (liverwort, moss etc). Cyano bacteria is thought to be an evolutionary ancestor of the chloroplasts found in eukaryotic organsims[9], resulting in a very similar photosynthetic process in all these organsism, thought there are many more divisions of algae resulting from secondary or even tertiary endosymbiosis events[10]. The main differences across all the oxygen evolving species lies in the antenna with much of the ETC remaining consistent.

1.2 The ETC of oxygenic photosynthetic organisms

The ETC in eukaryotes is usually non-cyclic, using water as an electron source and ending with NADP+ being reduced to NADPH. This process is the only biological process known to oxidise

water to molecular oxygen[11] accounting for all atmospheric oxygen. The overall reaction is shown by equation 1.2,

$$2\,H_2O + 2\,NADP^+ + 2\,H^+ \longrightarrow O_2 + 2\,NADPH + 4\,H^+ \tag{1.2}$$

with conversion of water to oxygen happening on the Lumenal side of the thylakoid membrane where the smaller volume enables a significant change in pH from the proton production. Cyt b_6f in plants (equivalent to Cyt bc_1 in bacteria) then creates the proton gradient (in conjunction with the PSII RC) necessary for ATP synthase to generate ATP. The entire process requires four electrons transferred and eight photons absorbed, one on each photosystem per electron transferred.

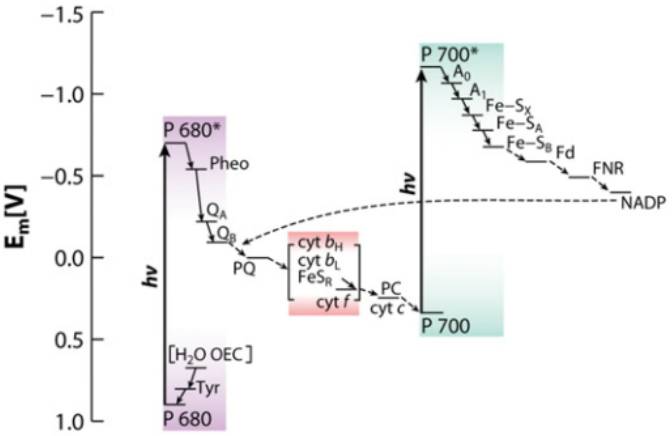

Figure 1.2: A schematic of the electron transport chain in higher plants (Z-scheme)[2]. We can see how most of the absorbed energy is lost in order to avoid recombination.

1.2.1 Photosystem II

The photosystem II (PSII) RC is the where the primary reaction takes place. It is much larger than that of purple bacteria, consisting of around 25 proteins[12]. However, the only essential ones are the two most core complexes: D1 and D2[13, 14]. The pigment composition of the D proteins is very similar to the RC of bacteria with 6 Chl *a* 2 pheophytin *a*, 2 beta carotene and

2 quinones. It is functionally the same and even has some sequential homology, especially at the reducing or acceptor side. Here the ETC chain works in the same way with the pheophytin accepting the electron and transferring it to the quinones which act as the two electron gateway (figure 1.2). Equation 1.3 shows the basic reaction.

$$2\,H_2O \longrightarrow O_2 + 4\,H^+ + 4\,e^- \tag{1.3}$$

The similarities break down at the oxidising side where the oxygen evolving function occurs. This process happens in another protein: oxygen-evolving complex (OEC).

1.2.2 Oxygen-evolving complex

The most unique, complicated and significant process in the ETC of higher plants is the oxidation of water by the oxygen evolving complex[15]. The essential reaction is

$$2\,H_2O \longrightarrow O_2 + 4\,H^+ + 4\,e^-. \tag{1.4}$$

Water is a very poor electron donor as oxygen is such a powerful electron acceptor. The redox potential of equation 1.4 is +0.82 V, so a particularly strong oxidant must be available. The actual mechanism for stripping the electrons from water is not properly understood. It is predicted that the key electron acceptor is a Mn complex which is progressively oxidised[16]. Cl^- and Ca^{2+} are necessary for this but the detail of the process is not known. The Mn centre is bound by ligand to the D1 protein and is stabilised by a nearby PsbO protein which also binds the Mn. After the RC chlorophyll (named P680 for its absorption peak) is oxidised, it is re-reduced in tens of nanoseconds by electron transfer from a nearby tyrosine in the D1 protein[17]. This is the connection between the RC and the OEC.

1.2.3 Cytochrome b_6f and Plastocyanin

Cyt b_6f is a set of transmembrane proteins that constitutes a complicated step in the electron transport chain[18]. Essentially it accepts electrons from plastoquinol and donates to a freely diffusible electron carrier in the lumenal space. In the case of higher plants this is plastocyanin

but in cyano-bacteria and green algae the plastocyanin is often replaced by Cyt c_2. In the process of electron transport, two protons are carried from the stromal side to the lumenal. This process is not fully understood but involves the oxidation of two molecules of ubiquinol and the reduction of a further one.

Plastocyanin will then reduce $P700^+$ (the RC) in PSI[19]. It is freely diffusible in the lumenal space and is therefore used to transport electrons large distances around the membrane[20]. It is able to dock to Cyt b_6f, accept an electron, and then disassociate and diffuse around the membrane. There it binds to PSI in order to donate an electron. It then repeats this process of binding and dissociating where needed.

1.2.4 Photosystem I

After the electron is transferred to plastocyanin, it is transferred to a docking site on Photosystem I[19] (PSI). PSI is a second RC and receives an exciton at its own special pair of Chls (P700 due to its distinct absorption peak at 700 nm). The PSI complex is a large set of proteins with a substantial antenna fused to the core, comprised of roughly 100 Chls and 22 beta-carotenes. In contrast to PSII which operates in a highly oxidising regime, PSI is much more reducing[12]. There is considerable evidence that the charge splitting reaction actually happens at an accessory Chl with the special pair quickly taking the positive charge, forming a strongly reducing redox potential of about -1.26V[21]. The electron is transferred to a nearby quinone and then on through three Fe−S centers[22] (figure 1.2). It is finally transferred to the soluble protein ferredoxin (Fd) which is a dual Fe core and holds one electron at a time.

1.2.5 Reduction of $NADP^+$

The final step of the non-cyclic ETC is at Ferredoxin $NADP^+$ Reductase (FNR) where two electrons are used to convert $NADP^+$ to NADPH through reaction 1.5[23].

$$2\,\mathrm{Fd\,(red)} + \mathrm{NADP^+} + \mathrm{H^+} \longrightarrow 2\,\mathrm{Fd\,(ox)} + \mathrm{NADPH} \tag{1.5}$$

In order for this two electron process to take place, it employs a flavin adenine dinucleotide to hold a single electron while waiting for a second docking of Fd.

1.3 Light harvesting

All Chl based photosynthetic organisms have an antenna of some sort[3, 24]. This antenna is almost always a pigment protein complex which is in some way connected (directly, distantly or temporarily) to the RC. In this way, excitons generated from the absorption of photon by pigments in the antenna, can be transferred to the RC for photochemistry. They are the most diverse part of the photosynthetic process and show signs of independent evolution in many different species. This matches the variety of photic environments that photosyntehtic organisms are found in. The first evidence for an antenna came in the 1930s when Emerson and Arnold flash saturated a pool of Chls and noticed that only one O_2 molecule was produced per 2500 Chl molecules. Many explanations were proposed, one of which was from Gaffron and Wohl who suggested that it was because the Chl molecules existed as one photsynthetic unit with energy being free to transfer around the pool. It was not until Förster proposed a mechanism for how this transfer could occur[25] in the 40s that the antenna theory became widely accepted.

The reason for the antenna is the relatively dilute photon content in sunlight. We can roughly calculate this using the flux of photons $I = 11\text{Å}^{-2}s^{-1}$. If the Chl has dimensions of roughly 10Å^2, it will be hit by approximately 1100 photons per second. We can now make a rough approximation of the average extinction coefficient across the spectrum, of $\varepsilon = 25mM^{-1}cm^{-1}$. This gives us a final value of 10 photons absorbed by a Chl per second[2]. This is already low considering the rate at which excited state energy is converted at the RC, but this represents an ideal situation. In many cases the chlorophyll will have a smaller cross section due to it angle with respect the the light source. In addition the flux may be lower according to the time of day or potential shadow. This would mean the rest of the expensive photosynthetic apparatus such as the enzymes involved in the Calvin-Benson cycle would remain unused for most of the time. Also as photosynthesis is a many electron process, intermediary products with excited states or charge, would have to remain in that state, waiting for a second photon to be processed. As they are not that stable, much of the energy would be lost. Therefore, many pigments are employed for the absorption of pigments for each RC.

1.3.1 Chlorophylls

Pigments are key to photosynthetic organisms as they are typically how energy is absorbed from the sun with the class of Chl being the most prevalent[26]. They are named Chl *a*-*f* and BChls *a*-*g* in order of their date of discovery. Chl *a*, the most common Chl in plants has a chemical formula of $C_{55}H_{72}N_4O_5Mg$ (figure 1.3). It is arranged in a roughly circular flat plane of carbons forming a ring around a central Mg. This Mg is coordinated to four N which form the point of four pyrrole rings consisting of the Nitrogen and four additional carbons. For this reason Chls are often termed tetra-pyrroles. Chl also has an additional fifth ring, attached to one of the pyrroles, and a long hydrocarbon chain attached to the adjacent pyrrole. This set up is closely related to the porphyrin ring but is less symmetrical. The rings are lettered a-e as shown in figure 1.3 and the outer edge of carbons are number clockwise 1-20. An extensive π delocalised network runs around the outside of the molecule but is broken by a reduced bond on the D ring between carbons 17 and 18. This reduction is the major difference from porphyrins and results in a new classification as chlorin. Two important axis pass through the molecule: the y axis through the nitrogens of ring A and C and the x-axis passing perpendicularly through the nitrogens of rings B and D. The entire Chl molecule contains three chiral carbons with BChls containing an additional two with almost all types of Chl and BChl enantiomerically pure. The main difference between Chl and BChl lies with the reduction of the c7-c8 bonds on the B-ring. This has the effect of reducing the conjugation and symmetry of the molecule, ultimately affecting the spectra. The various types of each simply have some functional groups on the edge replaced. Chl *c* is unusual in that the reduced bond on ring d is oxidised to a double bond and it is lacking the long hydrocarbon chain

Chls all contain two main regions of absorbance: one in the blue or near UV and one in the red or near IR (figure 1.4B). The red has two peaks, one with a slightly shorter wavelength one which loses energy rapidly to the lowest energy state. This state is relatively long lived, on the order of ns, and is the state used for electron transfer as well as energy storage. These low energy states are call the Q states where the high energy blue states are called the B states or Soret band. All of these transitions are π to π^*.

The two Q band spectral peaks can be explained using a simple four π molecular orbital

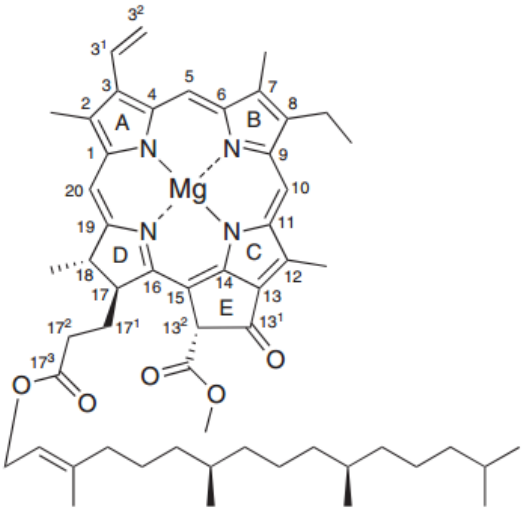

Figure 1.3: The structure of a Chl *a* molecule[2] with rings labelled A-E and carbons labelled 1-20.

(MO) picture (HOMO-1 to LUMO+1)[27] (figure 1.4A). In a perfectly symmetrical porphyrin ring, the HOMO and HOMO-1 would be isoenergetic, as would the LUMO and LUMO+1. The presence of the Mg at the centre disrupts this symmetry splitting the HOMO and HOMO-1. The reduction of the double bond on the D-ring then further reduces the symmetry, splitting the LUMO and LUMO+1 MOs. This splitting results in 4 different possible transitions instead of two. The Q states are built from a combination of these and many more electron configurations. However they can be said to be predominantly made of these four. The ground state is almost completely made of the electron configuration where the HOMO and HOMO-1 are fully occupied and the LUMO and LUMO+1 are not occupied. The lowest energy Q state is made primarily of a promotion of an electron from the HOMO to the LUMO. This has a large transition dipole from the ground state, lying along the y-axis of the molecule and is therefore called the Q_y state (figure 1.4A). The splitting of the HOMO/HOMO-1 and LUMO/LUMO+1 MOs have reduced the size of the HOMO to LUMO transition, resulting in a longer wavelength. The split is increased further still in BChl by the reduction of the double bond on the B-ring and the result is an even longer wavelength Q_y state. The second Q state is called Q_x as it roughly lies along the x-axis. It is mostly made up of the HOMO to LUMO+1 transition and has a shorter transition dipole

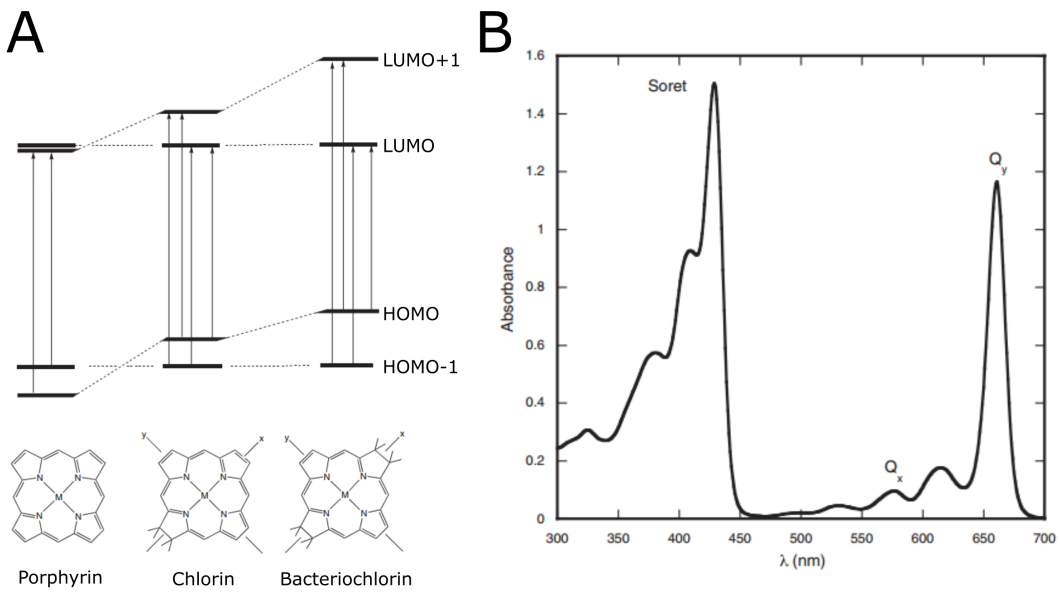

Figure 1.4: **A**. Shows the progressive splitting of the energy levels as functionality is added to Porphyrin[2]. **B**. A typical absorption profile for Chl a[2].

from the ground state.

Due to the larger size of the ground state to Q_y transition dipole, the highest chance of absorption occurs if the photon hits the molecule perpendicular to the y-axis. once it does, it will rearrange the π electrons along the y-axis. This rearrangement is followed by a rearrangement of the atoms to the excited state structure. As it rearranges, it falls in vibrational energy to the lowest vibrational energy level (0). When the state fluoresces, it does so most from the lower energy states due to Böltzman equilibration. The molecule then reaches a vibrationally excited ground state. The vibrational drop from the first excitation to the Q_y 0 point and the subsequent drop in energy from the vibrationally excited ground state to the ground 0 point results in a lower energy fluorescence than absorption. This is observed by a small increase in wavelength of the fluorescence peak compared to the absorption peak and is called the Stokes shift. It is a relatively small decrease as the reorganisation energy of the ground and Q_y states are quite small. Almost all the Chl emittance is from this state as the Q_x state loses its energy to the Q_y state too rapidly to fluoresce. The absorption peaks are altered when in the protein compared to solvent due to distortion including a pulling of the Mg out of the plain of the molecule. This can

result in changes of absorbance up to 100nm and is used to tune the direction of energy transfer as well as increasing the spectral cross-section of the antenna complex.

1.3.2 Carotenoids

Cars are found in all photosynthetic organisms[28, 29] and are found in almost all antenna complexes. There are hundreds of variations so a varied selection are shown in figure 1.5. However, they share some common structural features. The most significant is the long π conjugated backbone resembling polyenes. This is usually headed at either end with a ring, sometimes with an oxygen based group attached. Where an oxygen is involved as a functional group, the molecule is further categorized as a xanthophyll as well as a Car.

The conjugation brings the lowest absorption peaks down to the visible range and they have a particularly intense absorption peak at 400-500 nm. This is unusual as it is from the ground state (S_0) to the second excited state (S_2). The S_0 to first excited state (S_1) is strictly forbidden as it is a two electron excitation. The lifetime of the S_2 state is very short and undergoes internal conversion to the S_1 state in a sub picosecond timescale. The S_1 state also dissipates rapidly in approximately 10 ps to the S_0 state, though this transition is strictly non-radiative and instead dissipated as heat. Due to these rapid dissipation rates it is surprising that Cars can act as light harvesters at all as transfer to the Chl pool has to directly compete. However it has been show to effectively harvest energy from both the S_1 state as well as the S_2 state[30]. Cars that are longer than nine double bonds have a number of dark states in addition to the three states described[31]. The electronic states, with a focus on the unusual S_1, will be described in detail in chapter 4.

Bilins

Bilins are an unusual class of pigments found in pigment protein antenna complexes in that they covalently bond to the protein (figure 1.5). They are found in phycobillisomes of cyano bacteria and green algae and absorb in the 550-650nm wavelength range. They are made from splitting a heme, and as a result appear to be the four pyrrole rings of a typical heme, split apart and twisted to form a linear conformation (an open tetrapyrrole). They are linked to the protein usually at

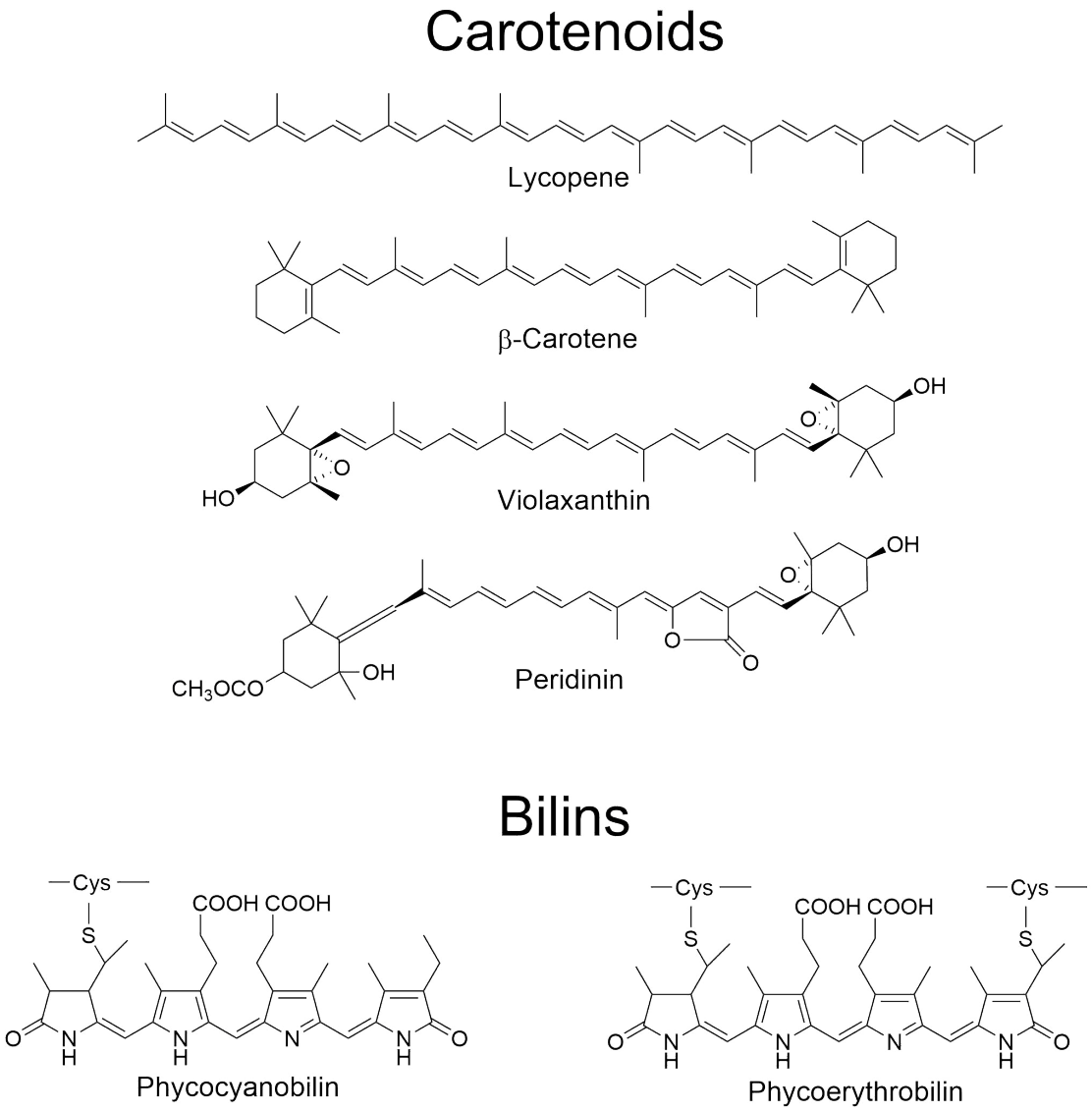

Figure 1.5: Schematics of commonly found Cars and bilins. We can see the variation in Cars with some having rings on the end, some having oxygen functional groups on the rings and some even having functional groups on the conjugated chain.

ring-A, but sometimes at ring-D as well, by a thioether bond to specific cysteine residues. These molecules are not relevant to the work in this thesis and are only mentioned for completeness.

1.3.3 Antenna complexes

The antenna can be thought of as an energetic and funnel. Specially programmed proteins hold the pigments in a specific spatial organisation. They also distort the pigments differently, affecting the excited state energy. Typically the peripheral antennas contain pigment which absorb at shorter wavelengths, with the more peripheral pigments in these absorbing at shorter wavelengths still. As the energy of these excited states can be described by an inverse proportionality to wavelength as described in equation 1.6, the further the pigment from the RC, the higher its excited state energy.

$$E = \frac{hc}{\lambda} \tag{1.6}$$

As downhill energetic transitions are thermodynamically more accessible than the reverse, a pattern of transfer towards the RC is promoted. The loss of energy is a sacrifice for higher efficiency of photon to charge separation. The higher speed of transfer to RC reduces chances of energy loss through dissipation, either by fluorescence, thermal dissipation or triplet formation. This energetic funnel can be a steep slope as in the case of phycobillisomes in bacteria and algae, or it may be relatively shallow as in the case of plants Other pigments typically absorb at different wavelengths to Chl and transfer their energy to the Chl pool.

There are two limiting cases as to how the antenna are arranged with respect to the RCs. A 'pool model' suggests that each RC is surrounded by a consistent set of antenna proteins, which transfer excited state energy directly and exclusively to that RC. On the other end, a 'lake model' suggests that the relationship between RC and antenna is more mobile. The main difference between the two extremes is that in the pool model, the exciton is transferred always to a particular RC whereas in the lake model it is 'free' to diffuse around and could find its way to a number of different RCs. In reality any system is likely to be somewhere between the two with variations dependent on the species. The 'connected units' model is an example of this, in which RCs are attached to a specific pool of antenna complexes which can transfer to other pools with lower probability. This has the advantage of being in the best configuration for

efficient transfer to the closes RC, but does not have to lose the exciton if the RC is damaged or is currently oxidised from recent photochemsitry. A second model called the domain model proposes a system where multiple RCs exist in an isolated pool of antenna proteins. This is most likely in organisms that have large antenna systems such as the green sulfur bacteria.

Types of antenna complex

The following will be a discussion of some of the more important or distinct antenna complexes. They can be simply categorised by a few common features. Most antenna span the lipid bilayer and are called integral membrane antenna complexes. However, extrinsic antennas do not and instead associate to a membrane protein from the surface of the membrane. Integral membrane antenna complexes can be divided into groups according to how they associate with the RC. Fused antenna are part of the RC and cannot be removed biochemically. Core can be removed biochemically but *in vivo* are consistently attached to the RC in a specific manner and exist in stoichiometric amounts to the RC. Finally, peripheral are present in variable amounts which allows the organism control due to their environment, they can attach to the RC but can also be mobile within the membrane.

Purple bacteria has two well defined and structured antenna complexes: light harvesting 1 (LH1) and light harvesting 2 (LH2). LH1 is a core antenna and is a ring of 16-18 protein subunits, surrounding the RC. LH2 is peripheral and is a smaller ring of 8-9 subunits. Each unit of LH2 contains 3 BChl a and 1 Car. One of the three Chls faces inward and is weakly coupled (1 ps transfer times) to the other two Chl pigments, with transfer described accurately by Förster theory. These two Chls are also arranged in a ring but are perpendicular to the third Chl. They are closer together and exhibit strong excitonic coupling. For this reason, excitations are rapidly (100 fs) delocalised around the entire ring. From here, excitations are transferred to a similar ring of Chls in LH1 (3 ps) which also has strong delocalisation. Finally it is transferred to the RC[32, 33, 34] with a much slower hopping time of 35-50 ps[35] with even slower (10 %) reverse energy transfer. This makes the whole process 'transfer-to-trap' limited as the speed of transfer between the pigments in the antenna complex does not significantly affect capture efficiency compared to this slow transfer to the RC (trap). The BChls have a higher

wavelength absorption profile, with a strong peak at 800. The slow transfer BChls in the LH2 ring are therefore called B800. The excitonic delocalisation of the small ring (B850) in LH2 brings this absorption band down in energy to 850. Finally the absorption of the BChl in the much larger LH1 ring (B875) is brought lower by the increased delocalisation to 875. This range of absorption bands creates a wider spectral cross section for the antenna complex. Each subunit of these proteins also contain a Car which is shown to exhibit ultra-fast transfer to the Chl pool through the S2 state. There is also evidence of transfer from the S1 state[36]. These two antenna complexes have also been shown to exhibit quantum coherence effects[37, 38].

The chlorosome is a general name for much larger antenna complexes, attached to the cytoplasmic side of the inner membrane and found in green sulfur bacteria, filamentous anoxygenic bacteria (FAB) and chloroacidobacteria. It contains around 200,000 BChl *c*, *d* or *e* pigments in close proximity to each other, with little to no protein. This creates a large excitonically delocalised block which transfers energy through a baseplate pigment-protein complex to the RC. Green sulfur bacteria and chloroacidobacteria also contain the FMO pigment protein antenna complex. This sits between the chlorosome and the RC, creating some diffusion space between the two. As these two have a PS1 RC and FAB does not, the diffusion space is likely to provide room for ferrodoxin to diffuse in and out.

Phycobilisomes are another example of extrinsic antenna complexes but are much smaller and more ordered. They typically consist of 2-3 protein subunits called billiproteins. They arrange in a fan like structure around a corebilliprotein which transfers energy to the RC. This antenna complex is the most clear example of the funnel system with the most distant antenna proteins absorbing at a short wavelength and each protein closer to the RC absorbs at slightly longer wavelengths.

Peridinin-chlorophyll protein (PCP) is an unusual antenna complex as it is water soluble and is freely diffusible in the thylakoid lumen space. It contains 4 keto-carotenoids (Per) as well as one Chl pigment in each unit. Transfer from Car to Chl has been shown to be fast and efficient due to its van-der-Waals contact. The Chl-Chl transfer is much slower[39] due to how much further away the pigments are (17A between subunits and 40-55 between complexes). PCP can temporarily bind to the membrane where it transfers its excited state energy to the Chl *a/c* of a membrane protein which transfers the energy to the RC.

1.3.4 Light harvesting in PSII

One of the most important antenna complexes in terms of global productivity is the light harvesting system II (LHCII) found in higher plants. It is responsible for the green, seen all around in flowering plants as well as ferns, mosses and others. It was first determined by electron microscopy[40] and electron crystallography[41] and finally its structure was revealed by x-ray crystallography[42]. Each unit contains three transmembrane helices which bind 8 Chl *a* and 6 Chl *b* as well as 4 Cars. There are two central luteins (Lut) arranged in a cross, a neoxanthin (Neo) which protrudes from the protein and finally a peripheral violaxanthin (Vio) which can de-attach and under go reversible de-epoxidation to zeaxanthin (Zea) (xanthophyll cycle). They are mostly peripheral proteins and can exist in varying proportions to the RC, depending on the species and conditions of growth. This gives plants great flexibility according to their photic environment. In addition to this they can move around in the membrane and can de-associate with the RCs.

LHCII is a peripheral antenna complex for PSII. However, they also form an integral part of the PSII supercomplex. This consists of a dimeric core of RCs which work independently. Immediately attached to these are the core antenna proteins CP43 and CP47. A number of antenna proteins form the remainder of the PSII supercomplex. There are two of each of the minor antenna: CP24, CP26 and CP29 immediately bound to the CP43 and CP47 proteins as well as a strongly bound and a slightly less strongly bound LHCII trimer on each side. The PSII supercomplex sometimes varies in size but is typically similar to the above description[13]. They are mobile within the grana stacks of the thylakoid membrane and associate with an increased number of additional peripheral LHCII trimers depending on the conditions. The minor antenna are composed from the same Lhc mutagenic family and share a lot of structural similarities with the LHCII monomer. Most of the Chl positions are preserved with the same coordinating amino acid residues[43]. CP26 shares the same pair of Luts, crossed at the centre of the protein while CP24 and CP29 have the Lut in 1 core position but a Vio in the other. They all possess the peripheral Neo apart from CP24 where it is absent[44]. LHCII units are the only proteins to contain the peripheral Vio.

These proteins are densely packed (average nearest neighbour inter-pigment distance $\sim 6-8$

Å[45, 42]) with a pigment to protein weight ratio of 1:2. This results in close inter pigment distances with the average Chl separation being around 10 Å. Therefore the EET exhibit some excitonic delocalisation in addition to slower Förster transfer processes. Typically the Cars transfer energy to the Chl pool and Chl *b* transfers energy to the Chl *a* pool due to the lower excitation energy of the Chl *a* Q_y state. This happens rapidly on a ps timescale with $> 95\%$ of the excitation energy in the Chl *a* pool due to Böltzmann equilibration. From there, the energy is typically localised on to a particularly low energy Chl *a* trimer Chl 610-612 termed the 'terminal emitter'[30, 46, 47]. This is located near the periphery of the protein on the stromal side and can transfer the energy between proteins towards the RC. Due to the structural similarities, EET happens in a very similar manner in the minor antenna, with energy rapidly localised on the same three Chls[48]. Interestingly steady state spectra fitting has shown these to not be the lowest energy Chls CP29, though they are still low[49].

1.4 Photoprotection

Photoprotection is an umbrella term for many processes which occur on very different timescales and in various area of the plant. However, they are all aimed at the reduction of photoinhibition

1.4.1 Photoinhibition

The antenna and suite of pigments provide a wide absorption profile, ensuring the plant can photosynthesise sufficiently in low light conditions, such as shade from clouds or other organisms. However, in combination with the high efficiency of photon absorbed to photochemical products produced, this results in a risk for the organism. In high light, the electron transfer processes and carbon fixing reactions are not able to keep up with energy capture[50]. This results in a build up of excited state energy in the Q_y band of the Chls as the usual 'trap' of the RC is not able to receive any energy (figure 1.6). Energy in the Q_y state is usually no problem on the timescale necessary for transfer to the RC. However, if this is extended considerably, some of the energy can undergo interconversion to triplet states which can form in the antenna or at the RC. These triplet states can react with oxygen radicals to form singlet oxygen species which are highly reactive. The RC has the additional problem of the large oxidative power needed to

drive the water splitting reaction. This can oxidise the pigments and protein around it if its lifetime is too long which may happen when a build up of reduced plastoquinone causes a lack of available electrons for $P680^+$. If the special pair does not oxidise its environment, it may undergo charge recombination, also resulting in triplet states[51, 52]. The resulting singlet oxygen species will then 'bleach' the RC, rendering it unable to receive excited state energy from the antenna. Damage to the D1 protein is particularly slow to repair and problems will persist for hours[53].

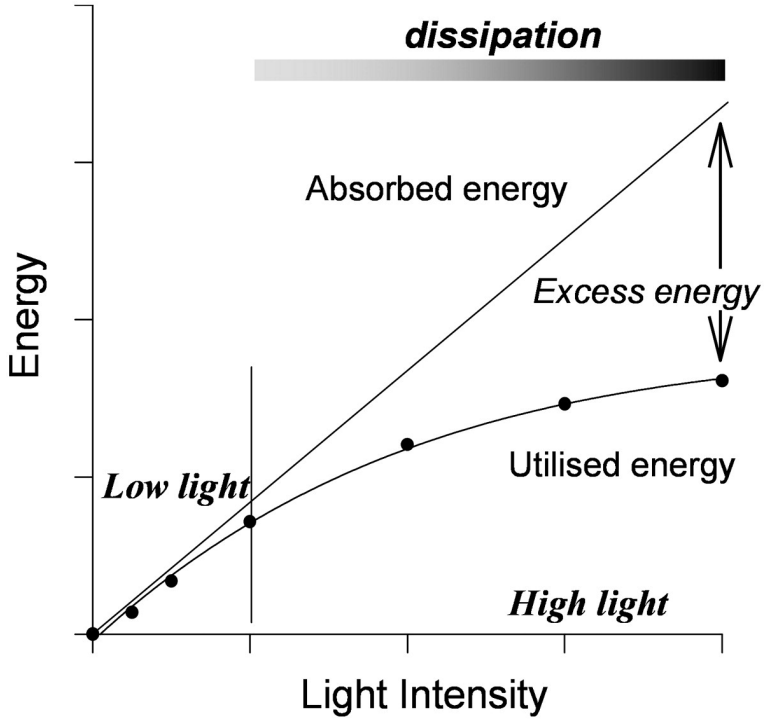

Figure 1.6: This figure from Ruban *et al.*[54] gives a basic understanding of how, as the light intensity increases, so does the gap between absorbed and utilised energy.

1.4.2 Prevention mechanisms

Plants must posses ways of dealing with the risk of photoinhibition and so employ a variety of strategies which can be categorised into preventing damage, scavenging the product of damaging processes or damage repair. Plants can move their leaves to reduce the surface area for light capture[55]. This can be done on a smaller scale with a reduced number of chloroplast or even pigments within the proteins[56]. This is a result of light dependent complex gene expression[57]

and is an effective method of adapting the plant to its environment, or the seasonal changes in light quality.

Plants also have a method for removing potentially harmful triplet Chls and singlet oxygen as they are formed. The excited state energy is transferred to triplet Car states where it dissipates to the grounds state. Transfer from the Chls is mediated through Dexter transfer meaning very small inter-pigment distances are necessary[58]. The lower energy Car triplet state is then very unlikely to transfer energy back to the Chl or any oxygen species. Typically the Luts will scavenge the triplet Chl state energy while the more peripheral Neo and Vio/Zea is more likely to scavenge the singlet oxygen energy[59]. However, the most efficient solution would be to prevent these states before they form. For this, plants have a fast acting mecahnism which is able to respond to moment-to-moment changes in the light intensity.

1.5 Non-photochemical quenching

The key photoprotective process in this thesis is called non-photochemical quenching (NPQ). In order for maximum response time, it must be a chemical change occurring at the site of photodamage: the thylakoid membrane, and is present as a feedback loop[60, 61]. An over-production of ATP will cause an increased population of H^+ ions which will inhibit electron transport protein cyt b/f as well as the oxygen evolving complex. There must therefore be a feedback loop at the photon capture and excited state energy deliver stage. In the membrane under normal circumstances the lifetime will be around 2 ns[62] with the RC trap closed. However in certain conditions, this lifetime significantly drops as can be seen by the rapid Chl florescence decay[63, 64]. This is NPQ and is simply the reduction of Chl fluorescence through non-photochemical means. It can be split into three processes, separated by their kinetics. qI is the slowest and is partly due to photodamage at the RC which quenches energy. However, this also has the effect of down-regulation of the genes expressing PSII. The next slowest is qT and is attributed to state transitions[65, 66]. The fastest process, which accounts for the bulk of NPQ is qE[67, 68].

1.5.1 The trigger

Chl fluorescence lifetime in LHCII was measured over a one hour illumination period. This exhibited some quenching but when the light source is turned off, only around 10% of the RCs were functioning[69, 54]. This form of NPQ is photoinhibitory quenching and is attributed to qI. However, if the membrane conditions are acidified, simulating the proton production from the water splitting process, almost all the RCs were operating after the hour of illumination. This is photoprotective quenching and is triggered by ΔpH. When qE is measured against ΔpH, there is a delay period between the change in pH and the activation of qE. This suggests that the ΔpH causes a large scale conformational change which takes some time to occur[70, 71]. This was initially proposed to happen at the RC[72] but time taken for the heat loss ($1.4\mu s$) is too quick for this to be the case[73]. It is therefore now thought to occur in the antenna. All four of the antenna proteins (LHCII, CP24, CP27 and CP29) were found to possess a similar quenching fingerprint, such as the 77K 700nm band[74, 75]. In addition to this, the removal of any one of the protein complexes from an organism reduces quenching by varying amounts, though it does not remove it all together[76, 77, 78]. This seems to suggest that quenching can occur in all four antenna proteins though there is still some debate concerning the minor antenna.

A potential cause for the conformational change which induces the quenching mechanism could be the presence of two glutamate residues on the lumenal side of each protein. These have been shown to bind DCCD[79] and would accept protons in acidic environments. However, the pKa of these residues lies around 4.0 which is too low for physiological conditions. In *vivo*, qE has also been shown to be linked to a process called aggregation. Betterle *et al.*[80] showed that qE came about in the membrane as result of dissociation of the LHCII units from the PSII RC. This brought the PSII RCs closer together and formed an aggregated group of LHCII proteins. Freeze fracture microscopy has also shown this LHCII aggregation and importantly it occurs on the same time-scale as qE[81].

1.5.2 Zeaxanthin

A link between ΔpH and aggregation was found in the form of the xanthophyll cycle[82]. LHCII possesses a peripheral Vio which can be removed from the protein, and reversible de-epoxidised

to Zea[83]. This process is promoted by the presence of protons and the presence of Zea strongly enhances qE[84, 85]. It was found that Zea is not necessary for qE to occur but that it increased the sensitivity of qE to ΔpH[86]. This is particularly important as it allows the plant to quench in low enough pH for the electron transport mechanisms to still be efficient, while at the upper end of the pH range ATP synthase is still able to produce ATP. This suggests that Zea does not quench itself but instead promotes the quencher somehow[87]. Membranes that have a greater concentration of Zea show greater mobility of the membrane proteins. Zea is the most hydrophobic antenna Car with few oxygen groups. It therefore has an effect on the tertiary and quaternary structure of the proteins increasing their mobility. In contrast Vio has relatively low hydrophobicity and hinders the process of aggregation[88].

In addition to this Zea also increases the rate at which qE forms and decreases the rate at which it relaxes[89]. Plants use this as a sort of memory effect. Because the epoxidation of Zea is a slower process than the reverse, Zea levels remain high after a quenching period has ended. This means that if a second quenching period is needed, the presence of the Zea will make the transition particularly rapid.

These findings prompted the LHCII aggregation model of qE[90] which consists of four different states. State I is the dark, or light harvesting state which has a population of Vio and no aggregation. When subjected to light, some aggregation may occur, though without the conversion of Vio to Zea, this is quite limited and we get a partially quenched state III. In prolonged light the Vio is converted to Zea which induces strong aggregation and deep quenching in state IV. The final state II is when the membrane returns to a light harvesting state but the lingering presence of Zea means there is still small amount of quenching due to increased aggregation compared to state I. This model explains a lot, including the relationships between the xanthophyll cycle, ΔpH, aggregation and qE. It also gives some explanation for the large range of membrane lifetimes we see in different photosynthetic organisms.

1.5.3 PsbS

PsbS was discovered as a smaller membrane protein in the 90s[91]. It exists in the thylakoid membrane and is stable without pigments suggesting it does not have role in light harvesting[92,

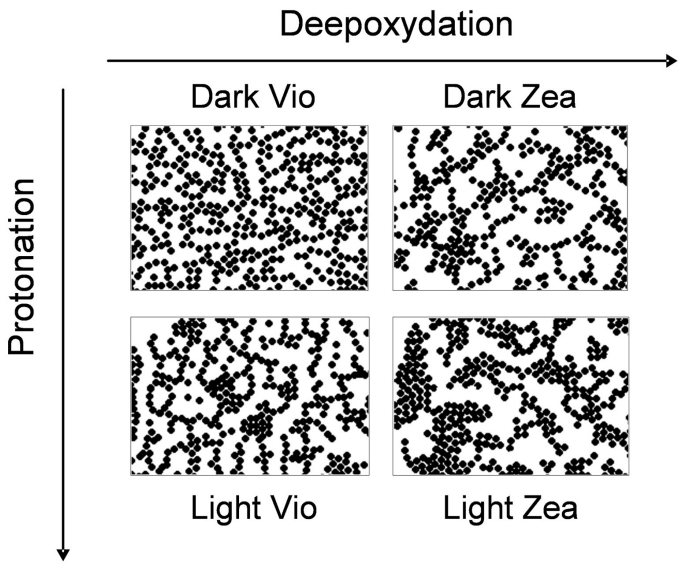

Figure 1.7: Figure taken from Ruban *et al.*[54]. Shows the patterning of LHCII units in intact spinach chloroplasts determined by freeze-fracture electron microscopy. We can see the combined effect of protonation and the presence of Zea on LHCII migration and aggregation.

93]. Its purpose seems to be linked to qE as mutant aribadopsis plants, grown without the gene for expressing it, exhibit almost no qE at all[94]. It was shown to have a stabilising effect on the rigidity of the grana stacks and can accelerate the stacking induced by Mg cations[95]. It also exhibits great mobility within the membrane, moving between the grana and the stroma lamallae[96]. Like the antenna proteins, it has two glutamate residues on the lumenal side which bind to DCCD[97]. However, the pKa of these amino acids is higher at approximately 6.0[97]. When in high light conditions it has been shown to monomerise, possible due to the acidification of the glutamates, whereupon it greatly increases the mobility of the other membrane proteins.

A final link between qE and protons can be seen in the membranes dependence on cations for organisation and specific lateral distribution. This is is particularly true for Mg which is responsible for the splitting of PSII and PSI, as well as the formation of the PSII supercomplexes[98]. The over-production of protons, released into the lumenal space may results in the neutralisation of negative point charges. This encourages the migration, through diffusion, of Mg cations into the stromal space. The membrane then becomes thinner, dehydrated and becomes more hydrophobic[99]. It is not yet clear if this has an effect on aggregation or qE but it is quite

possible.

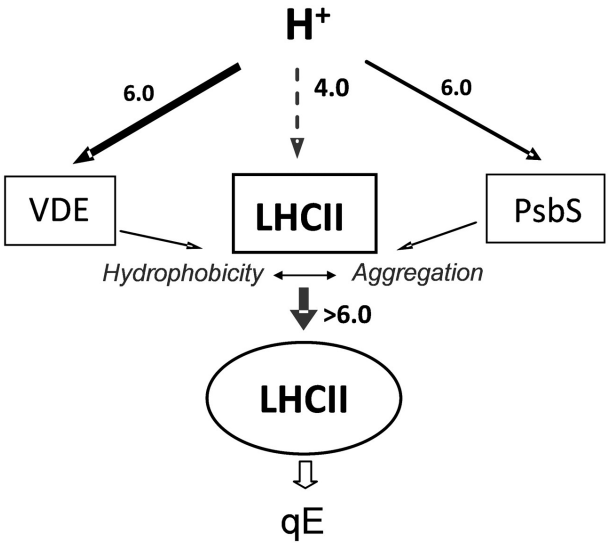

Figure 1.8: A potential scheme for how aggregation and consequently NPQ occurs from the trigger of protons[54].

The key here for both the xanthophyll cycle as well as PsbS is that the pKa of the relevant activation residues is around 6.0[97], which is well within the physiological range. This is in contrast to the pKa (4.0) of the glutamates on the lumen of the Lhc proteins[100]. One possibility is that acidification causes PsbS to increase mobility in the membrane. It also drives the xanthophyll cycle towards Zea which increases the hydrophobicity. The new environment in the membrane caused by these changes could have an effect on the pKa of LHCII, increasing it to within the physiological range[101] (figure 1.8). Studies on the qE dependence on pH in the presence of Zea and PsbS both show an increased sensitivity of qE to acidic conditions[97, 102]. Once LHCII is acidified, the protein would undergo some conformational change, inducing the formation of a new quenching trap. Alternatively, the protons could just drive aggregation and then this clumping of the proteins could cause the formation of the trap.

1.5.4 The trap

Chl fluorescence goes down over time due to a number of different processes. The first is internal conversion to the ground state of the Chl. This reduces the excitonic energy and releases it as heat. The second is transfer of Chl excited energy to a non-Chl pigment. There is also

the possibility of inter-system crossing to a low lying triplet state. However, this process is several orders of magnitude slower than the others and so effectively does not contribute to the reduction of fluorescence. NPQ is the rapid decrease in the fluoresce being emitted. This happens as a result of a reduction of the Chl excited sate energy. This obviously cannot be caused by an increase in the Chl fluorescence and must therefore be either an increase in the internal conversion, caused by some change to the environment, effectively turning the Chl molecule into a quencher. Alternatively it could be the increase of transfer to separate pigments. Chl in isolated LHCII has a fluorescence lifetime of around 4 ns which is reduced in the membrane to 2ns (when the RCs are closed with light)[103, 104]. There therefore already exists significant quenching which in the packed membrane must be kept in check during light harvesting periods. This is an impressive feat as the Chl pool is clearly in contact with some quenching pathway when entering the membrane as shown by the reduction of lifetime by half. Finally, when the membrane is acidified, the lifetime drops to around 0.4-0.6 ns[103, 104, 105].

There is substantial debate on the specific quencher, how many there are and how non-reversible the trap pathway is. One obvious possibility is the presence of the Cars. Energy would mostly be transferred to the lowest singlet excited state of Cars (S_1) which is roughly isoenergetic with the Q_y band. The S_1 has the same A_g symmetry as the S_0 state. In addition the transition is predominantly two-electron resulting in a heavily forbidden state transition by photons. However, the lifetime of the state is particularly low at around 10 ps due to internal conversion to the ground state, probably as a result of a conical intersection. Transfer from the Chl pool to the Cars would therefore result in the quenching of the excitation energy.

Transient absorption techniques have shown an instantaneous population of the Car S_1 state after excitation of the Chl Q_y state[106]. This can only be as a result of excitonic delocalisation between the two pigments. A low lying electronic state possessing character of both the S_1 and the Q_y states would be formed by the excitonic interaction and the S_1 character would result in quenching. The S_1 signal was predicted to be from Zea[106] which is unlikely to be directly involved in qE as described above. However, Liao *et al.*[107] showed the presence of the peak in species devoid of Zea so it is possible that other cars also exhibit this transfer.

With the presence of coherent transfer between Chl and Car the presence of charge transfer (CT) states becomes viable. This splitting of electron and hole on separate molecules is partic-

ularly likely in heterogeneous pairs. In this case the CT state could be lower than the low lying excitonic state and so may be populated. Charge separation can then be followed by charge recombination with a resulting dissipation of the energy. The population of these CT states would be evident with near infra-red cation Chl peaks[108]. This was detected by Flemming *et al.*[109] with a rise time of around 11ps, and attributed to Zea again. In the case of CP29 a similar state was found but was dependent on two Chl associated with the L2 site. They suggest a Zea cation[110, 111].

A final method of transfer to the Cars is through incoherent coupling. In this case the transfer is much slower and was shown to exist by Grondelle *et al.*[112] with a rise time of around 20-40 ps. This speed of transfer was described by Förster[25] in which the interaction comes from the dipoles of the two states. As the S_1 state has no dipole this should not be possible. However, small areas of positive and negative charge arise resulting from a state transition. While across the molecules, this may average out to a 0 dipole many small dipoles are localised on sections. If the Car and Chl are close enough the smaller dipoles could play a role in creating a path for incoherent transfer. The proposal here is that a conformational change to the protein affects either the molecule geometry or the spatial relationship between Chl and car, increasing EET. There is also potential for this to be through Dexter transfer as the molecules are close enough to make orbital overlap possible[113].

These quenching pathways all make use of the option of increased transfer to another pigments as a method for loss of Chl excited sate energy. The possibility of internal conversion in the Chl has also been proposed by some groups. The model given by Holzworth *et al.*[114] to fit TA data suggests that the loss of excited state energy comes from transfer to Chl-Chl CT state[105] which are known to have increased coupling to the ground state. This is possible in homogeneous pairs as the different anisotropic environments of the Chl, caused by the protein, have a significant effect on the Q_y energy. The presence of red-shifted Chl *a* states, which could be these CT states, have been suggested to be involved in quenching on multiple occasions[115, 116].

Summary

While there is a lot of disagreement in the field, most agree on some foundations of the NPQ process. Firstly that it is triggered by the change in pH caused by the natural proton production of the RCs. Secondly that the process occurs in the antenna. Third that some combination of the xanthophyll cycle, PsbS and aggregation have an effect on the antenna proteins resulting in a pathway toward quenching. This is usually described as a conformational change to the protein. It is also widely believed that the final step of quenching is the non-radiative dissipation between the Car S_1 and S_0 states.

Chapter 2

Quantum Chemistry

One of the primary goals of quantum mechanics is to solve the time-independent Schrödinger equation for molecules. This enables us to calculate their energy and from there, determine a range of other important properties. One property that is used repeatedly in this work is to find the equilibrium geometry of a molecule. There are two main approaches to solving the Schrödinger equation. An '*ab initio*' approach uses only fundamental constants as inputs and simply chooses from a range of methods for solving the Schrödinger equation to calculate other quantities. This can be computationally expensive and for larger systems it is impossible to get quantitative results in realistic timeframes. Often a 'semi-empirical' approach is used which will take a simpler form of the Hamiltonian as well as using certain experimentally obtained parameters. Both of these approaches will be discussed in this chapter.

Born-Oppenheimer approximation

Quantum chemistry is a computationally expensive process. In order to gain useful information in a reasonable time-frame, a number of approximations are employed. The first that we make is called the Born-Oppenheimer approximation[117] and it makes use of the large difference in the mass of the electron and the nuclei. This is significant as it means the electrons respond to changes in the positions of the nuclei almost instantaneously. We therefore regard the nuclei as fixed and solve the Schrödinger equation[118] for the electrons. Different arrangements of

the nuclei can then be adopted and the calculations repeated. This creates a Potential Energy Surface (PES) for the molecule and enables us to determine its equilibrium conformation.

In order to find the equilibrium geometry of a molecule, one must find the positions of the nuclei which give the lowest energy when solving the Schrödinger equation. If the positions of the nuclei are adjusted in any direction then the energy must go up. This lowest energy point is therefore flat on the PES. In a simple dimer system, the energy depends only on inter-atomic distance (R). We can therefore determine the equilibrium point at $\frac{dE}{dR} = 0$. At this point all the forces (f_i) exerted on the nuclei by the electron must cancel out. So in a more complex system, where the many nuclear coordinates are described by q_i, the equilibrium geometry is when

$$f_i = \frac{dE}{dq_i} = 0 \tag{2.1}$$

There are many computational techniques developed to find this point as soon as possible but they all essentially use the gradient of energy to nuclei coordinates to move iteratively towards it. In practice the exact equilibrium point will not be found but the calculation can be stopped once the change in energy is within a certain tolerance limit.

However, all of this depends on the Born-Oppenheimer approximation. On first consideration, this seems too great an approximation to make, but we will explore why this is not the case. If we consider a simple system of a H_2^+ in 1 dimension. The full Hamiltonian is

$$\hat{H} = -\frac{\hbar^2}{2m_e}\frac{d^2}{dz^2} - \sum_{j=1,2}\frac{\hbar^2}{2m_j}\frac{d^2}{dZ_j^2} + V(z, Z_1, Z_j) \tag{2.2}$$

where z is the location of the electron and Z_j is the location of the jth nuclei. The first term represents the kinetic energy of the electron, the second is the kinetic energy of the nuclei and the third is the potential energy of the system. The Schrödinger equation is

$$\hat{H}\Psi(z, Z_1, Z_2) = E\Psi(z, Z_1, Z_2) \tag{2.3}$$

but we attempt to solve when the wavefunction is of the form

$$\Psi(z, Z_1, Z_2) = \psi(z; Z_1, Z_2)\psi_n(Z_1, Z_2) \tag{2.4}$$

where ψ_n is the nuclear wavefunction and ψ is the electronic wavefunction which parametrically depends on the nuclear positions. We therefore get a different wavefunction for each set of nuclear positions. If we now look at the term arising from the kinetic energy of the nuclear position from equation 2.2,

$$\hat{H}_n^{ke} = -\sum_{j=1,2} \frac{\hbar^2}{2m_j}\Big(\frac{d\psi}{dZ_j}\frac{d\chi}{dZ_j} + \frac{d^2\psi}{dZ_j^2}\Big) \tag{2.5}$$

we see that it is non-zero as ψ depends on the nuclear coordinates. However, it is very small as the denominator contains the mass of the nuclei m_j and so we make the approximation that it can be separated from the rest of the Hamiltonian.

The Hamiltonian for a molecule in 3d space is now

$$\hat{H} - \frac{\hbar^2}{2m_e}\sum_i^n \sum_I^N \frac{Z_I e^2}{4\pi\varepsilon_0 r_{iI}} + \frac{1}{2}\sum_{ij}^n \frac{e^2}{4\pi\varepsilon_0 r_{ij}} \tag{2.6}$$

with upper case indices for the nuclei and lower case for the electrons. The nucleus-nucleus term is omitted as it is usually treated classically and added at the end.

The Hartree product

The complicated part of equation 2.6 is the electron-electron repulsion term as it requires the positions of two bodies through the separation r_{ij}. If we assume that ψ is similar to ψ^0 where the electron-electron term is neglected, we can write out a new Schrödinger equation

$$\hat{H}^0\psi^0 = E^0\psi^0 \tag{2.7}$$

where

$$\hat{H}^0 = \sum_i^n \hat{h}_i \tag{2.8}$$

This is a sum of the core electron Hamiltonian which gives the energy of the ith electron. We can then write the wavefunction as a product of the n one electron wavefunctions of the form $\phi_a^0(i)$, which is the ith electron in the ath orbital.

$$\psi^0 = \phi_a^0(1)\phi_b^0(2)\ldots\phi_z^0(n) \tag{2.9}$$

We must now take spin into consideration and make sure the system obeys the Pauli principle[119]. To do this we use a spin-orbital $\chi_a(i)$ where the index a now contains a spin component. When describing the system simply as

$$\Psi = \chi_a(1)\chi_b(2) \qquad\qquad \Psi = \chi_a(2)\chi_b(1) \tag{2.10}$$

where χ_a and χ_b have opposite spin. According to the Paul principle, the total wavefunction should be antisymmetric with respect to interchange of any pair of fermions. In this case the electrons are interchanged but the wavefunction does not change sign resulting in the wavefunction being 0. For electrons, we therefore write the wavefunction as the anti-symmetric combination

$$\Psi = \frac{1}{\sqrt{2}}\big[\chi_a(1)\chi_b(2) - \chi_a(2)\chi_b(1)\big] \tag{2.11}$$

For larger systems we take the wavefunction as a Slater determinant[120] to ensure the Pauli principle is obeyed,

$$\psi^0(x;R) = (n!)^{-1/2} det|\chi_a(1)\chi_b(2)\dots\chi_z(n)| \tag{2.12}$$

where x is the position of the electron and R is the position of the nuclei. This is useful as if two rows are swapped the sign of the determinant must change. In addition if any two electrons share the same orbital, then two rows must be the same and so the determinant must equal 0. At this stage the energy of the system is equal to the sum of the one-electron energies.

2.1 Hartree Fock

We must now include the important electron-electron terms or electron correlation. The Hartree-Fock (HF)[121, 122, 123] approach represents an important first step in this process and many more accurate methods start with HF. In it, the electron correlation is treated in an average way as each electron is considered as moving inside an electrostatic field of the nuclei and $n-1$ other electrons.

In the case of the one electron system: Hydrogen, we construct a set of functions for the electron to be in. These are 3D mathematical functions of space in the coordinates r, θ and

σ. These functions make up the orbitals and the electron in Hydrogen sits in the '1s' orbital. The number '1' is the first quantum number and denotes the size of the orbital or energy of the electron. The letter 's' denotes the second quantum number and represents the shape of the orbital or the angular momentum of the electron. In polyelectronic systems, we adopt the orbital approximation where each electron is treated separately with its own wavefunction.

The atomic spin-orbitals (χ) are expressed with a numerical value for each of the three coordinates and a spin component. An example of these are the numerical atomic functions produced by Hartree and later turned into an analytical form by Slater. These take the form of a product of an exponential function in r and a spherical harmonic function of θ and σ with a normalisation coefficient. For each atom, the various types of spherical harmonic functions are all the same with changes in the radial exponential function. The Slater-type orbitals can be shown to be particularly accurate as they give good energies for the systems they describe (according to the variational principle in which the lowest energy is the most accurate). These atomic orbital functions can be transformed into a new basis to make them ortho-normal. When they are not orthogonal there will be an overlap between them called the overlap integral

$$\int dr \chi_i^*(r)\chi_j(r) = S_{ij} \tag{2.13}$$

We will now adopt the dirac notation and rewrite this as

$$\langle \chi_i | \chi_j \rangle = S_{ij} \tag{2.14}$$

Here the -ket $|\chi_j\rangle$ represents a vector and the bra- $\langle \chi_i|$ represents its adjoint. When describing molecules instead of atoms, we extend this process to describe the molecular wavefunction in terms of its molecular orbitals

$$|\Psi\rangle = \left\{ |\phi_1\rangle, |\phi_2\rangle, \ldots |\phi_n\rangle \right\} \tag{2.15}$$

In smaller more symmetric molecules these molecular orbitals are specific, symmetry adapted linear combinations of atomic orbitals. This tends to break down for larger (typically biological)

molecules. Expanding the molecular orbitals as a linear combination of atomic orbitals gives

$$|\phi_i\rangle = \sum_k c_{ik} |\chi_k\rangle \tag{2.16}$$

where i represents the molecular orbital and k represents atomic orbitals and can be increased in size to however big an expansion you want. Increasing the size will give more flexibility in creating the wavefunction and so will improve accuracy at a computational cost. A form of the Schrödinger equation can be written for the molecular orbitals

$$H |\phi_i\rangle = \varepsilon_i |\phi_i\rangle \tag{2.17}$$

which can be expanded in terms of atomic orbitals

$$H \sum_k c_{ik} |\chi_k\rangle = \varepsilon_i \sum_k c_{ik} |\chi_k\rangle \tag{2.18}$$

If we then multiply by each of the set of normalised atomic orbital functions ($\langle\chi_l|$) (including χ_k) and integrate over space we get

$$\sum_k c_{ik} \langle\chi_l| \hat{H} |\chi_k\rangle = \varepsilon \sum_k \langle\chi_l|\chi_k\rangle \tag{2.19}$$

The convention is to write

$$H_{lk} = \langle\chi_l| \hat{H} |\chi_k\rangle \qquad\qquad S_{ik} = \langle\chi_l|\chi_k\rangle \tag{2.20}$$

so equation 2.19 can be tidied up as

$$c_{ik}(H_{lk} - \varepsilon_i S_{lk}) = 0 \tag{2.21}$$

This creates a set of so called secular equations where the number of equations is the number of molecular orbitals. These will only have non-trivial solutions if

$$det|H_{lk} - \varepsilon S_{lk}| = 0 \tag{2.22}$$

This matrix can become quite complex with larger systems but it can always be simplified to a diagonal matrix to solve for the various values of ε. Evaluating all H_{lk} and S_{lk} terms and multiplying out the determinant gives the various eigenenergies which can then be plugged back into the secular equations to give the coefficients. S_{lk} represents the overlap integral of two 3D functions and can be evaluated relatively easily. H_{lk} contains the 1 electron Hamiltonian and so is harder to evaluate. This process is the root of most methods for solving the Schrödinger equation for a molecules and the main way in which methods differ is in the 1 electron Hamiltonian.

If we now go back to a simplified form of the Hamiltonian under the Born-Oppenheimer approximation (2.6) as our starting place, we have

$$\hat{H} = -\frac{1}{2}\sum_{i}^{n}\nabla_i^2 - \sum_{i}^{n}\sum_{I}^{N}\frac{Z}{r_{iI}} + \frac{1}{2}\sum_{ij}^{n}\frac{1}{r_i j} \tag{2.23}$$

We separate the electron correlation term and call the rest the 0th order Hamiltonian ($\hat{H}_0$). The electron density can be described as $\langle\phi_i(1)|\phi_i(1)\rangle$ and the interaction between two electrons is shown as $\langle\phi_i(1)|\frac{1}{r_{ij}}|\phi_j(2)\rangle$. We now split the electron-electron interaction into two parts: the coulombic attraction (J) and an exchange interaction (K), so that the total electron Hamiltonian of $H\phi_i = \varepsilon_i\phi_i$ looks like

$$H = H_0 + \sum_{j} J - \sum_{j}^{'} K \tag{2.24}$$

where the prime indicates only summing electrons of the same spin as dictated by the Pauli exclusion principle. This is called the Fock operator and the form of J and K is given by

$$J = \langle\phi_j(2)|\frac{1}{r_{ij}}|\phi_j(2)\rangle|\phi_i(1)\rangle \tag{2.25}$$

$$K = \langle\phi_j(1)|\frac{1}{r_{ij}}|\phi_i(2)\rangle|\phi_j(1)\rangle \tag{2.26}$$

Using this Hamiltonian we can now evaluate the secular equations to give us the molecular state wavefunctions to give the coefficients in equation 2.16. We start with a guess set of c_{ik} which we use to calculate ε_i. This can then be fed back into the secular equations to give new values for c_{ik}. This process is repeated until the accuracy cannot be improved according to the variational

principle. This states that for any trial wavefunction, the energy

$$\varepsilon = \frac{\int \Psi^* \hat{H} \Psi d\tau}{\int \Psi^* \Psi d\tau} \tag{2.27}$$

must be equal to or greater than the true ground state energy $\varepsilon \geqslant E_0$. Once the calculated energy has reached this point, within certain limits, it is called self-consistent.

2.1.1 Roothan equations

We have so far dealt with the one electron integrals on centred on the atomic coordinates. These are relatively simple to compute numerically due to their spherical shape. However, in molecular systems there are terms arising from the need to calculate 2-centre integrals or the overlap of two orbitals. In order to deal with these, we use a known set of basis functions to expand the spin orbitals, allowing us to transform the HF equations into matrix form. We use a set of M basis functions (θ) and express the spatial wavefunction as

$$|\Psi_i\rangle = \sum_{j=1} c_{ij} \theta_j \tag{2.28}$$

From this set we can obtain M linearly independent spatial wavefunctions. We now expand the Fock equation to

$$f_1 \sum_{j=1}^{M} c_{ja} \theta_a(1) = \varepsilon_a \sum_{j=1}^{M} c_{ja} \theta_a(1) \tag{2.29}$$

In a similar fashion to the Hartree equations, we multiply by unity and integrate over space to give

$$\sum_{j=1}^{M} c_{ja} \langle\theta| f_1 |\theta\rangle = \varepsilon_a \sum_{j=1}^{M} c_{ja} \langle\theta|\theta\rangle \tag{2.30}$$

If we simplify two terms

$$F_{ij} = \langle\theta| f_1 |\theta\rangle \tag{2.31}$$

$$S_{ij} = \langle\theta|\theta\rangle \tag{2.32}$$

we can rewrite as

$$\sum_{j=1}^{M} F_{ij} c_{ja} = \varepsilon_a \sum_{j=1}^{M} S_{ij} c_{ja} \tag{2.33}$$

We now have a set of M simultaneous equations corresponding to each number of i which we call the Roothan equations[124]. These can be expressed as a matrix equation

$$Fc = Sc\varepsilon \tag{2.34}$$

where c is an $M \times M$ matrix where the elements are c_{ja} and ε is a $M \times M$ diagonal matrix where the energies of the orbitals are along the diagonal. Again this only has non-trivial solutions if

$$det|F - \varepsilon_a S| = 0 \tag{2.35}$$

F contains operators for the coulombic repulsion between two electrons and a modification based on the exchange interaction.

$$\begin{aligned} F_{ij} = \langle \theta_i(1)| \, h_1 \, |\theta_j(1)\rangle + 2 \sum c_{lu} c_{um} \, \langle \theta_i(1)\theta_l(2)| \, \frac{1}{r_{12}} \, |\theta_m(2)\theta_j(1)\rangle \\ - \sum c_{lu} c_{um} \, \langle \theta_i(1)\theta_l(2)| \, \frac{1}{r_{12}} \, |\theta_j(2)\theta_m(1)\rangle \end{aligned} \tag{2.36}$$

which can be tidied up with simpler notation and written in full as

$$F_{ij} = h_{ij} \sum_{lm} P_{lm} \big\{ (ij|lm) - 1/2(im|lj) \big\} \tag{2.37}$$

where the matrix elements

$$P_{lm} = 2 \sum_{n} c_{lu} c_{um} \tag{2.38}$$

are referred to as the density matrix elements and represent the total electron density in the overlap region of θ_l and θ_m. The one electron integrals from the h_{ij} term only need to be calculated once but the two-centre integrals: P_{lm}, need to be solved iteratively which poses quite a challenge as the number is of the order M^4. It is made somewhat simpler with use of symmetry to identify identically 0 terms as well as some terms that are equal. Also as the

orbitals are centred on the nuclei, some overlap integrals can be approximated to zero due to inter-atomic distance. We now have a method for evaluating the wavefunction of a molecule and so its energy. We start by evaluating the individual molecular orbitals, their energy and the extent to which they contribute to the overall wavefunction. These are then further broken down into linear combinations of known functions. In each case we use a iterative method to increase the accuracy of the energies and coefficients called the self-consistent field.

2.2 Including electron correlation

Our current Hartree-Fock method is based on an important approximation: the electron-electron interactions are treated in an average way and specific changes are not taken into account. We say that HF does not include electron correlation and including this correlation is the focus of many methods.

Configuration Interaction

In the HF regime, we arrange the n electrons in the lowest level positions of the $2M$ spin orbitals. However, this is only one way to arrange the electrons and many more Slater determinants can be created by combinations including the $2M - n$ high energy orbitals. The initially calculated determinant is called the reference determinant

$$|\Phi_0\rangle = ||\,|\phi_1\rangle\,, |\phi_2\rangle \ldots |\phi_a\rangle\,, |\phi_b\rangle \ldots |\phi_n\rangle \tag{2.39}$$

and from this, electrons are promoted to higher energy orbitals. This is done in categories of single excitations,

$$|\Phi_a^p\rangle = ||\,|\phi_1\rangle\,, |\phi_2\rangle \ldots |\phi_p\rangle\,, |\phi_b\rangle \ldots |\phi_n\rangle \tag{2.40}$$

double excitations

$$|\Phi_{ab}^{pq}\rangle = ||\,|\phi_1\rangle\,, |\phi_2\rangle \ldots |\phi_p\rangle\,, |\phi_q\rangle \ldots |\phi_n\rangle \tag{2.41}$$

and so on. Configuration state functions (CSF) are created from these new determinants and a linear combination is used to described excited states or to better describe the ground state.

$$|\Psi\rangle = C_0 |\Phi_0\rangle + \sum_{a,p} C_a^p |\Phi_a^p\rangle + \sum_{a<b,p<q} C_{ab}^{pq} |\Phi_{ab}^{pq}\rangle + \dots \tag{2.42}$$

where C is the expansion coefficient. The accuracy limit for the HF regime is increased by increasing the size of the basis set. The remaining inaccuracy comes from the electron correlation. This reduced by using CI[125] and as more CSFs are included, the accuracy for the electron correlation increases. As both approach ∞ the solution approaches the exact solution. The difference between a HF^{SCF} energy and the corresponding full CI energy using the same basis set is called the basis-set correlation error.

2.2.1 Multi-configurational self consistent field

In typical CI calculations, the c_{ij} coefficients from equation 2.16 are fixed as the CI expansion occurs. In a multi-configurational method, both the c_{ij} coefficients as well as C from equation 2.42 (the basis set coefficients) are optimised simultaneously. In order to limit the size of the calculation, the lowest energy orbitals are labelled inactive, orbitals around the HOMO and LUMO are labelled active and particularly high energy, unoccupied orbitals are called virtual. This means we only take combinations of electrons in the 'active space' which is a reasonable approximation and makes the calculations feasible for larger molecules. Then a number of electrons are selected to occupy this space and combinations of electron positions are taken as CSFs. In complete active space SCF (CASSCF)(CASSCF)[126] all combinations of electron positions within this set of orbitals are considered. This is a particularly useful method when calculating excited states which are made up of a large proportion of determinants involving multiple electron excitations. With larger active spaces, even this may become too computatinally demanding. In this case we can restrict the number of electron combinations by, for example, only allowing double excitations or limiting the number of electrons which can occupy the higher orbitals.

2.2.2 Multi-reference

A final method for increasing the accuracy of the electron correlation energy that shall be discussed here is the multi-reference method[127]. In typical methods, the determinant with the electrons filling the bottom energy orbitals is taken as the reference. All further determinants are created by promoting electrons from the reference. In multi-reference, any determinants with large enough contributions to the total wavefunction are taken as a reference. This means single double etc. excitations are taken from these references as well. In this regime, if all double excitations are taken, we also include quadruple excitations. This will obviously increase computational expense but in many cases, fewer determinants are necessary to achieve the same level of accuracy. Multi-configurational SCF wavefunctions are used as reference states for this method.

2.3 Density functional theory

Calculating the many spin orbitals in large systems from the large basis sets necessary to obtain accurate energies creates computational difficulties. An alternative to the previously described methods which somewhat helps to alleviate these issues is the density functional theory (DFT)[128, 129]. Instead of calculating CSFs, it starts with the electron probability density (ρ) and calculates the energy of the system in terms of $\rho(r)$. Energy is said to be a functional of $\rho(r)$ as for each given r there is a corresponding energy. We need a set of one-electron equations from which the electron density can be obtained. W. Kohn and L.J. Sham[130] showed that

$$E[\rho] = -\frac{1}{2}\sum_{i=1}^{n}\int \Psi_i^*(r_1)\nabla_1^2\Psi_i(r_1)dr_1 - \sum_{I=1}^{N}\frac{Z_I}{r_{Ii}}\rho(r_1)dr_1 + \frac{1}{2}\int\frac{\rho(r_1)\rho(r_2)}{r_{12}}dr_1dr_2 + E_{XC}[\rho] \tag{2.43}$$

where the ground state electron density

$$\rho(r) = \sum_{i=1}^{n}|\Psi_i(r)|^2 \tag{2.44}$$

summed over all occupied Kohn-Sham (KS) orbitals[130]. E_{XC} is the only part for which the exact analytical form is not known. The KS orbitals are found by solving the KS equations. For the one electron orbital they look like

$$-\frac{1}{2}\nabla_1^2 - \sum_{I=1}^{N}\frac{Z_I}{r_{Ii}} + \int\frac{\rho(r_2)}{r_{12}}dr_2 + V_{XC}(r_1)\Psi_i(r_1) = \varepsilon_i\Psi_i(r_1) \tag{2.45}$$

where $V_{XC}(r_1)$ is the functional derivative of the exchange-correlation energy

$$V_{XC}[\rho] = \frac{\delta E_{XC}[\rho]}{\delta\rho} \tag{2.46}$$

The process of calculating the KS orbitals follows the SCF method where an initial ρ is guessed and the energy calculated from it. The KS orbitals are evaluated as a linear combination of a known basis set.

2.3.1 The exchange-correlation functional

The exchange-correlation functional is often split into the exchange term and the dynamic correlation term. Most DFT methods differ in how they deal with these terms and the various approximations account for the majority of the inaccuracy in calculating ground state energies. In the local density approximation (LDA)[131], the exchange correlation function is

$$E_{XC} = \int\rho(r)\varepsilon_{XC}[\rho(r)]dr \tag{2.47}$$

where $\varepsilon_{XC}[\rho(r)]$ is the exchange correlation energy per electron in a homogeneous electron gas where an infinite number of electrons are in an infinitely large space and a uniform positive charge retains electro-neutrality. Obviously this is a rather large approximation as the positive and negative charges of a molecule are not uniformly spaced out. Nevertheless, the predicted structural properties are surprisingly accurate. In the LDA approximation, the exchange and correlation functionals depend only on ρ and not on any derivatives. An early attempt to correct this with some gradient is called the generalized gradient approximation (GGA)[131].

A range of exchange-correlation functionals have been developed have all been developed

with names designating a particular combination of exchange and correlation functional. A popular method is BLYP which uses a combination of the gradient-corrected exchange functional developed by A.D. Becke[132] and the gradient corrected correlation function developed by C. Lee, W. Yang and R.G. Parr[133, 134]. Probably the most widely used method is B3LYP which uses the same functionals as BLYP but with Hartree-Fock corrections creating a 'hybrid' theory. Other exchange functionals include mPW[135], PW91[136] and PBE[137]. PW91[136] and PBE[137] are also names for correlation functionals as well as TPSS[138] and many more.

2.3.2 Time-dependent density functional theory

Time-dependent density functional theory (TD-DFT)[139] is useful for investigating changes to a system due to an electronic or magnetic field. This is particularly useful for excited state energies where the time-dependent Hamiltonian looks like

$$\Big\{ -\frac{\hbar^2}{2m_e}\nabla_1^2 - \sum_I^N \frac{Z_I}{r_{I1}} + \int \frac{\rho(r_2,t)}{r_{12}} dr_2 + V_{ext}(t) + V_{XC}(r_1,t) \Big\} \psi_i(r_1,t) = i\hbar \frac{d}{dt}\psi_i(r_1,t) \tag{2.48}$$

where the external potential $V_{ext}(t)$, the exchange-correlation potential and the density are all time-dependent. The goal is to find out how the density changes according to varying external potential.

TD-DFT assumes single excitations as the Kohn-Sham orbitals are non-interacting. This means that a double excitation is simply the Slater determinant of two electrons promoted from the ground state to two virtual orbitals. This however, does not hold for true interacting states. Instead, a linear combination of Slater determinants should be taken. Recent use of multi-reference TD-DFT has shown to be a promising method for correcting this error[140]. However, it is a particularly computationally demanding approach.

2.4 Semi-empirical

Semi-empirical is an alternative to the previous *ab initio* methods. The two-electron integrals (J and K) are the rate limiting step for calculations, even with effective use of gaussian basis set expansions. Semi empirical methods ignore some of these terms deemed to be too small to have a major effect and replace many others with experimentally derived parameters. One of the limiting factors of SE is the accuracy of the experiments, the parameters are derived from. This is alleviated somewhat by the ability to adjust any parameters to reproduce chemical qualities. Many of the methods differ in how these parameters are formulated as they are very inter-connected (changing the parameters to match one chemical property will have an effect on all other chemical parameters). It was first developed to calculate properties of π electrons[141]. The n_π electrons are treated separately to the n_σ electrons due to their different energies and distinct symmetry. The empirical π electron Hamiltonian is as follows

$$\hat{H}_\pi = -\frac{1}{2}\sum_{i=1}^{n_\pi}\nabla_i^2 + \sum_{i=1}^{n_\pi} V_i^{\pi,eff} + \frac{1}{2}\sum_{i,j}^{n_\pi}\frac{1}{r_{12}} \tag{2.49}$$

where $V_i^{\pi,eff}$ is the potential energy of π electron i within a field of nuclei and σ electrons. The last term is the repulsive force of all other π electrons. The core Hamiltonian is the first two terms so we can represent the full Hamiltonian as

$$H_\pi = \sum_{i=1}^{n_\pi} h_i^\pi + \frac{1}{2}\sum_{i,j}^{n_\pi}\frac{1}{r_{12}} \tag{2.50}$$

This is an approximation as the π and σ electrons are treated separately with the effect of the σ electrons only appearing in the $V_i^{\pi,eff}$ term. In the Huckel molecular orbital (HMO) theory[142], the H_π is treated as a sum of one electron terms.

$$H_\pi = \sum_{i=1}^{n_\pi} h_i^{\pi,eff} \tag{2.51}$$

The wavefunction of the system is then a product of the one electron wavefunctions which satisfies $det|h^{\pi,eff} - ES| = 0$ which is an analogue of the Roothan equations. When calculating the integrals, HMO uses some severe approximations.

1. All overlap integrals $S_{rs} = \delta_{rs}$.

2. Diagonal elements $h_{rr}^{\pi,eff} = \alpha$.

3. Off-diagonal elements $h_{rs}^{\pi,eff} = \beta$ when r and s are bonded but is 0 when they are not.

The α and β parameters are the terms derived from experiment and make the method semi-empirical. The HMO contains almost no treatment of the π-π repulsion and as a result is only qualitative at best. The Pariser-Par-Pople (PPP)[143, 144, 145] method was an early attempt at correcting this. It starts with equation 2.51 and writes the π electron wavefunction as a Slater determinant of π electron spin orbitals.

$$\Psi = ||\phi_a^\pi(1), \phi_b^\pi(1), \ldots \phi_z^\pi(n_\pi)|| \tag{2.52}$$

When we come to evaluating the two-electron integrals we make some approximations. We call the product of $\langle\phi_i|\phi_j\rangle$ the differential overlap. In the zero differential overlap approximation (ZDO), this is treated as 0 when $i \neq j$ and as a result $(ab|cd)$ becomes $\delta_{ab}\delta_{cd}(aa|cc)$. The integral is given as an empirical parameter. This greatly simplifies the Fock matrix.

2.4.1 Treatment of differential overlap

A number of semi-empirical methods have been developed which explicitly treat valence electrons and differ in which 2-electron integrals they treat as zero. In a closed-shell molecule with n_v valence electrons, the valence electron Hamiltonian is given by

$$\hat{H}_v = \sum_i^{n_v} h_i^v = \frac{1}{2}\sum_{i.j}^{n_v} \frac{1}{r_{ij}} \tag{2.53}$$

where h_i^v is the core Hamiltonian for the ith electron

$$h_i^v = -\frac{\hbar^2}{2m_e}\nabla_i^2 + V_i^{v,eff} \tag{2.54}$$

$V_i^{v,eff}$ is the effective potential energy for the ith electron in a potential field of the nuclei and all other inner-shell electrons. This process is analogous to the π electron model previously

mentioned and results in a set of Roothan type equations to be solved in a self-consistent fashion

$$F_{ij}^{v} = h_{ij}^{v} + \sum_{l,m} P_{lm}\Big\{(ij|lm) - \frac{1}{2}(im|lj)\Big\} \tag{2.55}$$

The zero deferential overlap approximation is known as the complete neglect of differential overlap (CNDO)[146].

$$(ij|lm) = \delta_{ij}\delta_{lm}(ii|ll) \tag{2.56}$$

In this case the two-electron integral is set to 0, even when the two electrons of different orbitals are from the same atom.

In the intermediate neglect of differential overlap (INDO)[146], the exchange integrals are retained for orbitals on the same atom. If we consider a diagonal element F_{ii}^{v}, the integral $(im|lj)$ becomes $(im|li)$. One contribution to this is $l = m \neq i$ giving $(im|mi)$. This would not be included in CNDO but is in INDO. For both of these methods, the remaining integrals are taken to be parameters that are adjusted until the results resemble those of a HF-SCF calculation.

Further advances parametrized with the aim of reproducing four gas-phase molecule properties: molecular geometries, enthalpies of formation, dipole moments and ionization energies. The first of these was modified intermediate neglect of differential overlap (MINDO)[147] which proved to be effective for hydrocarbons. Next to this came ZINDO[148], developed by M.C. Zerner which was optimised to reproduce the quantities of d-block elements of the first and second rows.

A significant increase in accuracy came with the neglect of diatomic differential overlap (NDDO)[146] where the differential overlap is only neglected when the basis functions belong to different atoms. Most subsequent methods are based on this and the introduction of modified neglect of differential overlap (MNDO) represents the first method to become widely used in predictive practice. The improved parametrisation of MNDO was further built upon by including hydrogen bonding in the parametrization process for the Austin Model 1 (AM1)[149]. It does not include d-orbitals in its basis sets and so is only useful for organic molecules or those including light metal atoms which do not possess any occupied d-orbitals. Various small modifications of these methods have been formulated for various specific systems or types of atom. The most

widely used of these is the protein model (PMX)[150] series which has proven to be particularly effective for studies on proteins. Because of the imprecise nature of the parametrisation, some earlier methods can work for certain molecules and so when choosing a semi-empirical method, it is often best to test a range of formulations.

An aspect of semi-empirical is that, although they are very approximate they include electron correlation both explicitly in the form of the various 2-electron integrals but implicitly as well through the parametrisation process. This means that when accompanied with methods for determining the excited states of molecules such as configuration interaction, they are able to predict the double electron excitations of certain molecules. This is particularly relevant for this thesis as the S_1 state of the Cars is primarily a two-electron excitation. The drawback is comes with a level of inaccuracy, inherent in the approximations made as time saving measures. For our work however, we have shown that while Semi-Empirical is not necessarily very accurate quantitatively, it follows the trends of more accurate and expensive methods well[151, 152].

2.5 ONIOM

With all of these available methods having particular advantages in accuracy or efficiency, a calculation set up to combine them can be particularly useful. ONIOM[153] is a procedure which separates a quantum chemical calculation into layers. Lower levels are treated with a cheaper method such as semi-empirical while higher layers can be treated with more expensive methods. A careful choice of the distinction between layers can provide the benefits of cheap methods by including a large number of atoms while still maintaining the accuracy of more expensive methods on the pertinent molecule/s. The technique also has the capability of combining quantum mechanical methods with molecular mechanics on lower levels. Molecular mechanics forgoes solving the Schrödinger equation and instead represents the forces between atoms using classical mechanics. The coupling of these two theories uses microiteractions[154] and a quadratic coupled algorithm[155] but as molecular mechanical methods are not used in this work, the reader is directed to the previous two sources for further reading.

Chapter 3

Exciton dynamics

3.1 The Frenkel exciton

This section will detail our description of the light harvesting complexes as fundamentally quantum systems. We have already seen how the structures and atom coordinates are dictated by quantum chemistry. We will now see how the key processes: absorption of energy, general dissipation from individual sites and inter-site transfer are all quantum processes. Any modelling splits the 'universe' into the system, which is simply the specific sites of interest, and the bath, which is everything else. There are then two key couplings which describe how the system evolves in time. Firstly, the coupling between the sites within the system which describes how the energy evolves within the system, reaching a thermal equilibrium. The second is the coupling of the system to the bath which is necessary for dissipation of energy.

Important to note that some of the methods described here (such as Redfield theory) are not used in this work. They are included to provide an overview of methods for evolving a system in time. The choice between methods such as Förster and Redfield represents a key topic of debate in this field.

3.1.1 The system Hamiltonian

Where the system is a pigment-protein such as LHCII, we must create a Hamiltonian to describe the excited states of the molecular aggregate as well as choose an appropriate method for propagating the system in time. We are interested in the state of the pigments only. We can therefore make the split between the pigments which we will call the system and the environment which we will call the bath. This follows the equation

$$\hat{H} = \hat{H}_s + \hat{H}_b + \hat{H}_{sb} \tag{3.1}$$

We can describe the system with the general Hamiltonian for the aggregate of N-molecules in the Born-Oppenheimer approximation as

$$\begin{aligned}\hat{H}_{agg}(R) = &\sum_{i}^{N}\sum_{\alpha}^{M}\Big(\frac{\hat{p}_{i\alpha}^2}{2m} + \sum_{k}^{K} V(\hat{x}_{i\alpha}, R_{ik})\Big) \\ &+ \frac{1}{2}\sum_{i\neq j}^{N}\sum_{\alpha\beta}^{M}\frac{\eta}{|\hat{x}_{i\alpha} - \hat{x}_{j\beta}|} + \sum_{i\neq j}^{N}\sum_{\alpha k}^{K}\frac{\eta Z_k}{|\hat{x}_{i\alpha} - R_{jk}|}\end{aligned} \tag{3.2}$$

The indicies i and j refer to molecules, α and β refer to electrons and k to nuclei. $\hat{x}_{i\alpha}$ and $\hat{p}_{i\alpha}$ are the coordinate and momentum operators of the αth electron of the ith molecule and $\hat{R}_{ik}$ is the position of the kth nucleus. Z_k is the charge of the kth nucleus and $\eta = e^2(4\pi\varepsilon\varepsilon_0)^{-1}$

In our modelling, we are only interested in two states for each molecule: the ground and first singlet excited states. We denote these states for molecule j as $\left|\Psi_j^{(g)}\right\rangle$ for the ground and $\left|\Psi_j^{(e)}\right\rangle$ for the excited state. These are then taken as the basis for building states of the whole system. This aggregate state is taken as a product of the state vectors of the individual molecules and is given by

$$|g\rangle = \prod_{j}^{N}\left|\Psi_j^{(g)}\right\rangle \tag{3.3}$$

for the ground state and

$$|i\rangle = \left|\Psi_i^{(e)}\right\rangle\prod_{i\neq j}^{N}\left|\Psi_j^{(g)}\right\rangle \tag{3.4}$$

for the excited states. This is the Frenkel exciton model[156], where electrons and 'holes' are taken in pairs together. It is most accurate when it is difficult for the excitons to freely move

about in a material and the electron-hole pairs are relatively strongly coupled as in our case where the excitons are localised to individual molecules. In the site representation, where the system is built from vectors describing individual pigments, the Hamiltonian is given by

$$\hat{H}_s = \sum_{i}^{N} \varepsilon_i \left|i\right\rangle \left\langle i\right| + \sum_{i \neq j}^{N} J_{ij} \left|i\right\rangle \left\langle j\right| \tag{3.5}$$

where ε represented the transition energy from $\left|\Psi_j^{(g)}\right\rangle$ to $\left|\Psi_j^{(e)}\right\rangle$ on pigment i and J_{ij} represents the coupling between two excited states on molecules i and j. The transition energy in the aggregate is given by

$$\varepsilon_i = \varepsilon_i^0 + \eta \sum_{j \neq i}^{N} \int dr_1 \int dr_2 \frac{\left[\rho_i^{(ee)}(r_1) - \rho_i^{(gg)}(r_1)\right] \rho_j^{(gg)}(r_2)}{|r_1 - r_2|} \tag{3.6}$$

which describes the transition energy when the molecule is in isolation (ε_0) with an additional term to describe how it is affected by the rest of the molecules. Here ρ_i^{gg} is the total charge density for the ground state of the ith molecule and ρ_i^{ee} is the same for the excited state. For neutral molecules, as in our system, these are 0. The coupling

$$J_{ij} = \eta \int dr_1 \int dr_2 \frac{\rho_i^{(eg)}(r_1) \rho_j^{(eg)}(r_2)}{|r_1 - r_2|} \tag{3.7}$$

is approximated as the Coulomb interaction between two molecules. $\rho_i^{(eg)}(r)$ is the transition charge density.

An aggregate containing N molecules has 1 ground state configuration and N singly excited states. There are more states if double excitations and so on are included but in light harvesting proteins, the rate of excitation is low so this can be safely ignored. The aggregate exciton eigenstate properties are given by diagonalising the Hamiltonian from equation 3.5. The eigenvalues are the energies of the excitons and are given along the diagonal of the matrix

$$\varepsilon = S^\dagger \hat{H} S \tag{3.8}$$

where S is the transformation matrix whose columns are the eigenvectors of $\hat{H}$. The N single

exciton states are described as

$$|\alpha\rangle = \sum_{i}^{N} S^{\dagger} |i\rangle \tag{3.9}$$

These transformations, change the basis set to the aggregate exciton vectors rather than the molecule state vectors. It gives us a diagonal Hamiltonian matrix with new exciton energies that differ from the energies of the individual pigments with contributions from the J values on the off-diagonal elements.

Davydov splitting

The best way to show how this happens is with a simple homodimer system[157]. In a system where there are two identical molecules which do not interact ($J = 0$), the Hamiltonian is written as a diagonal matrix with the energies of the state transitions on the diagonal elements.

$$\hat{H} = \begin{bmatrix} \varepsilon & 0 \\ 0 & \varepsilon \end{bmatrix} \tag{3.10}$$

The eigenstates of $\hat{H}\vec{C} = \varepsilon\vec{C}$ are obvious

$$\begin{bmatrix} 1 \\ 0 \end{bmatrix} and \begin{bmatrix} 0 \\ 1 \end{bmatrix} \tag{3.11}$$

both giving an energy of ε. However, in a coupled homo-dimer, these are no longer eigenstates

$$\begin{bmatrix} \varepsilon & J \\ J & \varepsilon \end{bmatrix} \begin{bmatrix} 1 \\ 0 \end{bmatrix} = \begin{bmatrix} \varepsilon \\ J \end{bmatrix} \neq \varepsilon \begin{bmatrix} 1 \\ 0 \end{bmatrix} \tag{3.12}$$

In order to solve for this coupled system we will create two new states and call them $|+\rangle$ and $|-\rangle$. These new states must be superpositions of the original states $|1\rangle$ and $|2\rangle$ such that

$$\begin{aligned} |+\rangle &= C_1^{+} |1\rangle + C_2^{+} |2\rangle \\ |-\rangle &= C_1^{-} |1\rangle + C_2^{-} |2\rangle . \end{aligned} \tag{3.13}$$

We can now form an expression for the energies of the new states from these coefficients C

$$\begin{aligned}\begin{bmatrix} \varepsilon & J \\ J & \varepsilon \end{bmatrix} \begin{bmatrix} C_1^{\pm} \\ C_2^{\pm} \end{bmatrix} &= E^{\pm} \begin{bmatrix} C_1^{\pm} \\ C_2^{\pm} \end{bmatrix} \\ &= \begin{bmatrix} E^{\pm} & 0 \\ 0 & E^{\pm} \end{bmatrix} \begin{bmatrix} C_1^{\pm} \\ C_2^{\pm} \end{bmatrix}\end{aligned} \tag{3.14}$$

This can be rearranged to give

$$\begin{bmatrix} \varepsilon - E^{\pm} & J \\ J & \varepsilon - E^{\pm} \end{bmatrix} \begin{bmatrix} C_1^{\pm} \\ C_2^{\pm} \end{bmatrix} = 0 \tag{3.15}$$

For this to have non-trivial solutions,

$$det \begin{vmatrix} \varepsilon - E^{\pm} & J \\ J & \varepsilon - E^{\pm} \end{vmatrix} = 0 \tag{3.16}$$

must be true. If we calculate the determinant we get the solutions

$$E^{\pm} = \varepsilon \pm J \tag{3.17}$$

which gives the energies of the $|+\rangle$ and $|-\rangle$ states.

In this case if the system is taken from the site-basis to an aggregate the coupling causes a mixing of the states. In the hetero-dimer case the two new energies can be obtained using a mixing angle which is a degree to which the two original molecules mix to create the new states. The mixing angle depends on the coupling and the energy gap as

$$tan\theta = \frac{2J_{ij}}{E_i - E_j} \tag{3.18}$$

The new eigenstates can be calculated using the transformation matrix

$$\begin{bmatrix} \cos\theta & -\sin\theta \\ \sin\theta & \cos\theta \end{bmatrix} \tag{3.19}$$

3.1.2 Coupling between sites

The rate of transfer is related to the spectral overlap but also a coupling term. This is denoted by a J_{ij} in equation 3.97 and must be calculated for each pair of pigments. The energetic coupling between a donor state (D) and an acceptor state (A) is given by the intermolecular transfer integral.

$$W_{DA} = J_{DA} - K_{DA} \tag{3.20}$$

It is divided into a coulombic interaction, modulated by an exchange term. The exchange interaction relies on orbital overlap and is reduced exponentially with increased intermolecular distance. It is therefore almost always much smaller than the coulombic part and is therefore neglected. This is why we use the coulombic coupling (J_{ij}) for the transfer rate. This will be discussed in further detail in the context of Car S_1 coupling in chapter 5.

There are a number of different methods for calculating this interaction. The most simple is the dipole-dipole interaction and usually proves to be effective when the inter-molecular distances are greater than the span of the molecules. It approximates the total charge densities associated with an electronic transition (ρ_i^{eg}) with a simple dipole (μ). This dipole then interacts with the transition dipole of another molecule according to its length and direction. This combined with a distance factor gives coupling. The dipole in the coordinate representation is

$$\hat{\mu} = \sum_{m\alpha} q_{m\alpha}(\hat{x}_{m\alpha} - R_m) \tag{3.21}$$

where the sum is over all charges (α) of the molecule (m) and R_m is the atomic centre. We can now express coupling in terms of two of these dipoles on states i and j

$$J_{ij} = \frac{1}{4\pi\varepsilon\varepsilon_0}\left(\frac{(\mu_{ig}\cdot\mu_{jg})}{|R_{ij}|^3} - 3\frac{(R_{ij}\cdot\mu_{ig})(R_{ij}\cdot\mu_{jg})}{|R_ij|^5}\right) \tag{3.22}$$

where ε_0 is the permittivity of free space and ε adjusts for the specific environment. This study relies upon knowing the couplings between the S_1 state of the Cars and other states. However, if the charge densities of the S_0 to S_1 transition are summed in the coordinate representation, the dipole is approximately 0. With the dipole-dipole approximation, this would give 0 for couplings but transfer has been shown to occur from the Car S_1 state to the Chl Q_y state. This is due to the interactions with the charge density of specific areas of the molecules. We therefore have to treat the charge densities in a more sophisticated manner.

The first of these is the monopoles approach which localises the charge densities associated with each atomic orbital onto the atomic coordinates. These are called atomic transition density moments (T_α) and the transfer integral (J_{DA}) is defined by the pairwise interaction of the T_a on two molecules. The dipole moment between the ground state ($|GS\rangle$) and the excited state ($|EX\rangle$) is defined by the dipole moment as

$$\begin{aligned}\vec{\mu}_M &= \langle GS|\,\hat{\mu}\,|EX\rangle \\ &= \sum_{i\in M} e\vec{r}_i\,\langle GS|\,\hat{N}_i\,|EX\rangle \\ &= \sum_{i\in M} e\vec{r}_i T_i \end{aligned} \tag{3.23}$$

summing over the i orbitals in molecule M where r_i labels the atomic coordinate associated with the ith atomic orbital. We can express the number operator in the second quantization formalism using creation and annihilation operators.

$$\hat{N}_i = \sum_\sigma \hat{c}^\dagger_{i\sigma}\hat{c}_{i\sigma} \tag{3.24}$$

where the creation operator ($\hat{c}_{i\sigma}$) creates an electron of σ spin in orbital i and the adjoint is the annihilation operator. The creation and annihilation operators in the atomic orbital basis can then be expanded as linear combinations in the molecular orbital basis

$$\hat{N}_i = \sum_{m,m',\sigma} \beta^*_{im}\beta_{im'}\hat{a}^\dagger_{m\sigma}\hat{a}_{m'\sigma} \tag{3.25}$$

where the operators are now creating and annihilating in the mth molecular orbital and β_{im} is the

ith atomic orbital coefficient of the mth molecular orbital. These can be obtained straight from the excited state calculation output. The total transition density moment (TDM) associated with molecule a is then the sum

$$T_a = \sum_{i \in a} \langle GS| \hat{N}_i |EX\rangle \tag{3.26}$$

If we define the ground and excited state (limited to single excitations) in the configuration interaction formalism (expanded upon in section 2.2) as

$$|GS\rangle = |\Psi_0\rangle \tag{3.27}$$

$$|EX\rangle = \sum_{a,r,\sigma} C_{a\sigma}^{r\sigma} |\Psi_{a\sigma}^{r\sigma}\rangle \tag{3.28}$$

where an electron of σ spin is promoted from the ath occupied orbital to the rth unoccupied orbital and Ψ_0 represents a state where the electrons fill the lowest energy positions. The C terms are the CI coefficients which can also be obtained from the excited state calculation output. The excited state can also be expressed as

$$|EX\rangle = \sum_{a,r,\sigma} C_{a\sigma}^{r\sigma} \hat{a}_{r\sigma}^{\dagger} \hat{a}_{a\sigma} |\Psi_0\rangle \tag{3.29}$$

and combining this with equation 3.25 gives us

$$T_i = \sum_{a,r,\sigma} C_{a\sigma}^{r\sigma} \beta_{im}^{*} \beta_{im'} \tag{3.30}$$

This is assuming the ground state is entirely the reference determinant and the excited state is made up of just single excitations. We can now calculate the TDM for any molecule from the excited state calculations. The transfer integral is now the pairwise interaction

$$\begin{aligned} J_{DA} &= \sum_{i \in D, j \in A} = V_{ij} \langle EX_A| \hat{N}_j |GS_A\rangle \langle GS_D| \hat{N}_i |EX_D\rangle \\ &= \sum_{i \in D, j \in A} = V_{ij} T_i^D T_j^A \end{aligned} \tag{3.31}$$

where V_{ij} scales the interaction according to

$$V_{ij} = \frac{e^2}{4\pi\varepsilon\varepsilon_0(|r_i| - |r_j|)} \tag{3.32}$$

where $|r_i|$ is the central coordinate of molecule i.

Finally, the Transition Density Cube method represents the most accurate way of determining coulombic coupling between two molecules[158]. In this the Transition density is apportioned out to a grid in 3D space around the molecule. At each intersection of the grid there is a point charge density. The transition density is then described as

$$M_{DA}(x,y,z) = \int_x^{x+\delta x} \int_y^{y+\delta y} \int_z^{z+\delta z} \Psi_{GS}\Psi_{EX} dxdydz \tag{3.33}$$

In this way the only limits on the coupling are the accuracy of the ground and excited state wavefunctions as well as the grid size. Reducing the distance between point charges on the grid towards 0 increases the accuracy of the coupling to exact (with exact wavefunctions). The coupling is given by the pairwise sum of all point charge interactions between donor and acceptor molecule.

$$J_{DA} = \sum_{i,j} \frac{e^2}{4\pi\varepsilon\varepsilon_0} \times \frac{M_D(i)M_A(j)}{|\vec{r_i} - \vec{r_j}|} \tag{3.34}$$

3.1.3 System-bath interaction

In order for this system to evolve in time, it must have some interaction with a bath. In its most simple form this can be the bath of photons but in order to describe a dissipative system such as a light harvesting complex, coupling to a thermal bath must be present. The bath represents the entire environment around the electronic states and encompasses the vibrational movements of the pigments as well as the protein around it.

In a complete description of the molecular aggregate, the bath Degrees of Freedom (DoF) are included. This is the vibrational movements of the molecules as well as the nuclear DoF of the protein/solvent. When they are coupled to the system they can induce relaxation and damping.

The bath Hamiltonian is represented as

$$\hat{H}_b = \hat{T}(\hat{p}) + \hat{V}(\hat{q}) \tag{3.35}$$

and the system-bath coupling is represented as

$$\hat{H}_{sb} = \sum_i^N \hat{Q}_i \Delta\hat{V}_i(\hat{q}) \tag{3.36}$$

where $\hat{T}$ and $\hat{V}$ are the kinetic and potential energies of the ith molecule nuclei. The $\hat{p}$ and $\hat{q}$ terms are the generalised momenta and coordinates of the bath. $\hat{Q}_i$ projects onto the ith site

$$\hat{Q}_i = |i\rangle \langle i| \tag{3.37}$$

and the energy gap operator is given by

$$\Delta\hat{V}_i(\hat{q}) = \hat{V}_i - \hat{V}_g - \left\langle \hat{V}_i(\hat{q}) - \hat{V}_g(\hat{q}) \right\rangle_b \tag{3.38}$$

This describes the energy gap between the ground and excited state, coupled to the interaction from the bath. It is represented by the final term which is averaged over the bath which we call the reorganisation energy.

$$\lambda_i = \left\langle \hat{V}_i(\hat{q}) - \hat{V}_g(\hat{q}) \right\rangle_b \tag{3.39}$$

the reorganisation gives us the extent of the interaction with the ith molecule and the bath. It also serves to renormalise the transition energies giving us the stokes shift. This means we can rewrite the system Hamiltonian to include this system-bath interaction as

$$\hat{H}_s = \sum_i^N (\varepsilon_i^0 + \lambda) |i\rangle \langle i| + \sum_{i \neq j}^N J_{ij} |i\rangle \langle j| \tag{3.40}$$

The bath DoF are usually much greater than the system DoF and so are usually dealt with in a separate manner. This is done with a statistical or thermodynamic approach where the key

parameter is temperature,

$$k_B T \equiv \beta^{-1} \tag{3.41}$$

including the Boltzmann factor. Fluctuations in the bath cause fluctuations in the pigments which affect the transition energies. This is represented by a correlation function

$$C_{ij}(t) = \left\langle \Delta\hat{V}_i(t)\Delta\hat{V}_j(0)\right\rangle_b \tag{3.42}$$

where $\Delta\hat{V}_i(t)$ is the energy gap operator and looks like

$$\Delta\hat{V}_i(t) = e^{-\frac{i}{1}\hat{H}_b t}\Delta\hat{V}_i(\hat{q})e^{-\frac{i}{\hbar}\hat{H}_b t} \tag{3.43}$$

in the interaction picture. The correlation function is derived from the spectral density of the bath $C''_{ij}(\omega)$. This is derived from the odd part of the Fourier transform of the correlation function. The relationship is given as follows

$$C_{ij}(t) = \int_{-\infty}^{\infty} \frac{d\omega}{2\pi} C''_{ij}(\omega)\Big[\cos(\omega t)\coth\left(\frac{\beta\omega}{2}\right) - i\sin(\omega t)\Big] \tag{3.44}$$

or

$$C_{ij}(t) = \frac{1}{\pi}\int_{-\infty}^{\infty} d\omega e^{i\omega t}\frac{1}{1-e^{-\beta\omega}} C''_{ij}(\omega) \tag{3.45}$$

The spectral density can be determined from fluorescence line-narrowing measurements or molecular dynamics simulations. It is assumed to have no overlap between separate pigments and so no interpigment coupling terms. A specific model for the spectral density of individual states can be used but a typical form is the over-damped Brownian oscillator

$$C''_i(\omega) = 2\lambda_i \frac{\omega\gamma_i}{\omega^2 + \gamma_i^2} \tag{3.46}$$

where γ_i^{-1} is the correlation time of ith molecule site energy fluctuations. I use this for the chlorophyll Q_y state but derive a specific shape for the Car S_1 state. This is discussed in detail in the next chapter. It should be noted that for the purposes of this thesis, the bath coordinates are traced out and so the only example of their presence is in the spectral densities of the states

and the reorganisation energies. This provides the impact the bath has on the system, and allows transitions between states that are not different in energy.

3.2 Evolution in time

I here note that the theory for evolution in time described below details the basics of this process but is not necessarily all used in this work. It is included as the theory and two limiting cases (Förster and Redfield) are very typical and it is useful to explain these procedures to show how the method I use fits in. We will be using a Förster theory for the EET transfer rates where appropriate and an approximation of Redfield to account for any coherence between states. The propagation in time is then conducted with a set of N (where N is the number of sites/pigments) equations containing the rates of EET in each direction. This is expanded upon at the end of this chapter.

With this interaction with the bath, the system can now evolve in time and we need a way to represent this with the wavefunction. The wavefunction must therefore be variable in the Schrödinger picture. For this to happen it is acted upon by the time evolution operator $U(t, t_0)$ to take the wavefunction from time 0 to t.

$$U(t, t_0) \left|\Psi(t_0)\right\rangle = \left|\Psi(t)\right\rangle \tag{3.47}$$

The basis of the wavefunction is transformed into a new set of orthonormal vectors spanning the proper Hilbert space.

$$B = \{\nu_1, \nu_2 \ldots \nu_n\} \tag{3.48}$$

The new wavefunctions are superpositions of the new basis set vectors with corresponding weightings

$$\left|\Psi(t_0)\right\rangle \rightarrow \sum C_n(t_0) \left|\phi_n\right\rangle \tag{3.49}$$

We don't need to know ϕ_n and can essentially represent the new wavefunction as

$$\sum C_n(t_0)\,|\phi_n\rangle \equiv \begin{bmatrix} c_1 \\ c_2 \\ \vdots \\ c_n \end{bmatrix} \tag{3.50}$$

The time evolution operator then acts on these weighting coefficients.

$$|\Psi(t)\rangle \to \sum C_n(t)\,|\phi_n\rangle \tag{3.51}$$

We can now plug equation 3.47 into the Shrödinger equation to give

$$\Big[i\hbar\frac{d}{dt}U(t,t_0)\Big]\,|\Psi(t_0)\rangle = \Big[\hat{H}U(t,t_0)\Big]\,|\Psi(t_0)\rangle \tag{3.52}$$

The wavefunctions cancel and the rest can be integrated to give

$$U(t,t_0) = U(t_0,t_0) - i\hbar\int_{t_0}^{t} d\tau \hat{H}(\tau)U(\tau,t_0) \tag{3.53}$$

Which can be given for time 0 to τ in the same way.

$$U(\tau,t_0) = \hat{I} - i\hbar\int_{t_0}^{\tau} d\tau_1 \hat{H}(\tau_1)U(\tau_1,t_0) \tag{3.54}$$

Equation 3.54 can then be plugged into equation 3.53 iteratively giving a time order expansion.

$$U(t,t_0) = \hat{I} + \sum^{\infty}\Big(-\frac{i}{h}\Big)^n \int_{t_0}^{t} d\tau_n \int_{t_0}^{\tau_n} d\tau_{n-1}\ldots\int_{t_0}^{\tau_2} d\tau_1 \tag{3.55}$$

This is very difficult to solve past the 2nd order and so is of little use. In order to solve it, we turn to perturbation theory. Here we create some 0th order Hamiltonian ($\hat{H_0}$) which describes most of the system, and add a perturbation.

For this we introduce the idea of the interaction picture where

$$H = H_0 + V(t) \tag{3.56}$$

and V(t) is the perturbation. This assumes that the majority of the Hamiltonian is described by a $0th$ order Hamiltonian which we can solve exactly and that the remainder is a 'perturbation' which effectively does not change the $0th$ order Hamiltonian. In this picture the time evolution operator changes with time as well as the wavefunction so

$$\langle A(t)\rangle = \langle \Psi_0 | \, U^\dagger(t) A U(t) \, | \Psi_0 \rangle \tag{3.57}$$

where

$$U(t) = U_0(t) U_I(t) \tag{3.58}$$

Equation 3.57 written with the $\hat{I}$ matrix written as the complex conjugate pair of the U_0 operators inserted

$$\langle A(t)\rangle = \langle \Psi_0 | \, U^\dagger(t) U_0(t) U_0^\dagger(t) A U_0(t) U_0^\dagger(t) U(t) \, | \Psi_0 \rangle \tag{3.59}$$

In this way we have $U_I(t)$ acting on Ψ and $U_0(t)$ acting on A. Now we can construct a very similar equation to 3.55 for $U_I(t)$

$$U_I(t, t_0) = \hat{I} - \frac{-i}{\hbar} \int_0^t V_I(\tau) d\tau - \frac{1}{\hbar^2} \int_0^\tau d\tau_2 \int_0^{\tau_2} d\tau_1 V_I(\tau_2) V_I(\tau_1) \tag{3.60}$$

where

$$V_I(t) = U_0^\dagger(t) V_S(t) U_0(t) \tag{3.61}$$

Here the perturbation term $V(t)$ is evolved by the 0th order Hamiltonian

$$V_I(t) = e^{\frac{i}{\hbar} H_0 t} V(\tau) e^{\frac{-i}{\hbar} H_0 t} \tag{3.62}$$

This means the first order operation for taking $|\Psi(0)\rangle$ to $|\Psi(t)\rangle$ starts with a transformation from time 0 to time τ with the transformation matrix $U_0(\tau)$. It is then scaled by the perturbation $V(\tau)$

constructed from equation 3.61. This is finally transformed to time=t with the transformation matrix $U_0(t)U_0^\dagger(\tau)$.

$$U_I(t,t_0) = 1 - \frac{i}{\hbar}\int_0^t d\tau U_0(t)U_0^\dagger(\tau)V(\tau)U_0(\tau) \tag{3.63}$$

$\hat{V}(t)$ is 0 when $t < 0$ and a constant matrix when $t \geq 0$

While this use of perturbation theory results in a unsolvable solution, a similar approach will be used in later sections to describe how to deal with more complicated systems. It remains a useful description of perturbation in a general sense.

3.2.1 Density Matrix

So far this has been a process where a system is described perfectly by a wavefunction or a superposition of eigenvectors. This is called a 'pure state' but for most realist cases, this is not possible as there are far to many variables. Technically (while debatable) the universe or a human body is a system and should be described by a wavefunction. However, this is clearly not feasible and so we use a different way to treat these systems. They can be divided into two cases: an ensemble which is simply a distribution of many states, or a subsystem which is treated as separate but connected to an averaged out environment. These are both called 'statistical mixtures'. This is an important change as it marks the loss of determinism in the process. Our observables are now probabilities of finding various outcomes.

In the ensemble model there are N states and a probability of finding the system in each state.

$$P_1 \left|\phi_1\right\rangle$$
$$P_2 \left|\phi_2\right\rangle$$
$$\vdots$$
$$P_n \left|\phi_n\right\rangle$$

The system can be described as $P_n\{\phi_n\}$ which is not a wavefunction $|\Psi\rangle$ where the states are in a super-position as the states are in no way correlated. An observable expectation value is then

given by

$$\langle O \rangle = \sum_n P_n \langle \phi_n | \hat{O} | \phi_n \rangle \tag{3.64}$$

These are $1 \times n$, $n \times n$ and $n \times 1$ matrices respectively which, when multiplied together, give a 1×1 matrix, or a scalar answer . Because it is a 1×1 matrix the trace is equal to the only element and so equation 3.64 can be written as

$$\langle O \rangle = \mathrm{Tr}\left\{ \sum_n P_n \langle \phi_n | \hat{O} | \phi_n \rangle \right\} \tag{3.65}$$

Due to the cyclic property of the trace this can be rewritten as

$$\mathrm{Tr}\left\{ \sum_n P_n | \phi_n \rangle \langle \phi_n | \hat{O} \right\} \tag{3.66}$$

where the part $\sum_n P_n | \phi_n \rangle \langle \phi_n |$ is called the density matrix ($\hat{W}$) and so we get the density matrix equation for an observable

$$\langle O \rangle = \mathrm{Tr}\left\{ \hat{W} \hat{O} \right\} \tag{3.67}$$

where the dimensions are that of the Hamiltonian. We can now transform this into a proper basis set of orthonormal eigenvectors by diagonalising $\hat{W}$ to give a $n \times n$ matrix where the rows and columns are the basis set eigenvectors and each element is given by $W_{ii} = \langle i | \hat{W} | i \rangle$ where $\hat{W}$ is represented by

$$\hat{W} = \sum P_n | \phi_n \rangle \langle \phi_n | \tag{3.68}$$

The equation for the elements of the new density matrix can then be given by

$$\hat{W}_{ii} = \sum_n P_n \langle i | \phi_n \rangle \langle \phi_n | i \rangle \tag{3.69}$$

We therefore have a diagonal matrix where the diagonal elements ϕ_{nn} are the probability of finding the system in the state represented by the eigenvector $|\phi_n\rangle$. These summed should equal 1 as it is certain the system will be in one of the states. This diagonal matrix is much easier to use. Any off-diagonal $\hat{W}_{12}$ terms arise if $\langle 1 | \hat{W} | 2 \rangle$ is non-zero which can only occur if ϕ_n is a superposition of the two states and it represents coherence.

The system has no well defined stationary state or eigenstates and instead evolves as a function of time. The density matrix can be described as a statistical mixture of states (equation 3.68). We can propagate these states in time with the time-evolution operator

$$\hat{W} = \sum_n U(t) P_n \left|\phi_n\right\rangle \left\langle\phi_n\right| U^\dagger(t) \tag{3.70}$$

which is simplified to

$$\hat{W}(t) = U(t)\hat{W}(0)U^\dagger(t) \tag{3.71}$$

This time evolution operator is very difficult to calculate so we need a more sophisticated method of propagating the density matrix in time. For this we use the Liouville equation

$$\frac{d}{dt}\hat{W} = -\frac{i}{\hbar}\big[\hat{H}, \hat{W}\big] \tag{3.72}$$

This is a commutator and looks like

$$\frac{d}{dt}\hat{W} = -\frac{i}{\hbar}\big(\hat{H}\hat{W} - \hat{W}\hat{H}\big) \tag{3.73}$$

when written out in full. The Liouville super operator can be written in shorthand as

$$\frac{d}{dt} = -\frac{i}{\hbar}\mathcal{L}\hat{W} \tag{3.74}$$

The Liouvillian operator is a rank 4 tensor matrix called a superoperator.

3.2.2 System-bath model

In the system-bath model, there is a conceptual division between the system and its environment. Both the density operator and the Hamiltonian are split in this way as both are a part of the Liouville operator (equation 3.74. The Hamiltonian is divided into three parts,

$$\hat{H} = \hat{H}_s + \hat{H}_s + \hat{H}_{sb} \tag{3.75}$$

where $\hat{H}_s$ is for the system, $\hat{H}_b$ is for the bath and $\hat{H}_{sb}$ is the coupling between the two.

For the density operator we can get rid of the bath, as it is unnecessary to treat it explicitly, by taking the reduced system density matrix (RSDM). This is done using a partial trace where only the bath parts are traced out and the remainder is still a matrix of the system part. It is represented as

$$\rho(t) = \mathrm{Tr}_B \, \hat{W}(t) \tag{3.76}$$

where the trace is

$$\mathrm{Tr}_B(\hat{W}) = \sum_i \langle b_i | \, \hat{W} \, | b_i \rangle \tag{3.77}$$

in a suitable basis set for the bath $\{|b_i\rangle\}$. Dimensionality of ρ is the size of the system and any system observable can be represented as

$$\langle O_s \rangle = \mathrm{Tr} \, \rho \hat{O}_s \tag{3.78}$$

We can write the RSDM at time a specific time as

$$\rho(t) = \mathrm{Tr}_B \, \hat{W}(t) \tag{3.79}$$

If we now write the Louville equation with the RSDM we get

$$\frac{d\hat{\hat{W}}}{dt} = -\frac{i}{\hbar}[\hat{H}_s, \hat{\hat{W}}] + \frac{i}{\hbar}[\hat{H}_{sb}, \hat{W}]. \tag{3.80}$$

This still includes the full density matrix and so is impossible to calculate. We therefore need some approximations to deal with this. The first and most simple one is to assume the bath is at equilibrium so that it can simply be represented thermally and separated from the RSDM. This gives

$$\hat{W}(0) \equiv \rho(0) \otimes \ \hat{W}_b^{eq}, \tag{3.81}$$

and if we assume the bath is a canonical ensemble we can write the bath density matrix as

$$\rho_b^{eq} \equiv \frac{e^{-\beta \hat{H}_b}}{Z} \tag{3.82}$$

where Z is the canonical partition function.

3.3 Approximate solutions

There are many different theories which vary in complexity to deal with the time-evolution of a system which are beyond the scope of this thesis. We will discuss two important limiting cases where a conceptually simple approximation is made. The basic idea is to use perturbation theory as was discussed in section 3.2. The first case takes the system-bath interaction as small and treats it as the perturbation. In this situation the coupling between pigments are much stronger than the electron phonon couplings and so we get coherence within the system. The second case is the opposite and describes the system when the system-bath interaction is stronger than the inter-pigment couplings. In this case the couplings are taken as the perturbation and any coherence is destroyed as it forms.

3.3.1 Quantum Master Equation

EET is naturally a dissipative process where energy is gradually lost by coupling of the electronic DoF to phonons. This is represented by the system-bath coupling and can vary from state to state. These dissipations have the effect of destroying coherence between the states. If the coupling to the environment is weaker than the inter-state coupling, a degree of coherence remains. This results in a number of important distinctions. The first is that the coherences between the states result in new excitonic states. These then form a new basis for the populations to be calculated in. This is represented in the original density matrix by the presence of non-zero off-diagonal elements. Within this system energy typically thermally equilibrates in a sub-picosecond time-frame.

The Hamiltonian for the system and the bath are lumped together and treated as the $\hat{H}_0$ in the interaction picture. The remaining $\hat{H}_{sb}$ term is treated as the perturbation V. If the density matrix is propagated by equation 3.71, in the interaction picture it is

$$\rho(t) = U_0(t)U_I(t)\rho(0)U_I(t)U_0^\dagger(t) \tag{3.83}$$

where the middle three terms are the interaction picture density matrix ρ_I. The interaction picture time-evolution operator is propagated by the interaction picture perturbation V_I so we can define a interaction picture Liouville operator.

$$\mathcal{L}_I(t)\cdot \equiv \big[V_I, \cdot\big] \tag{3.84}$$

so the interaction picture RSDM is

$$\begin{aligned}\sigma_I(t) &= \mathrm{Tr}_B\, \rho_I(t) \\ &= \Big\langle exp_+ - \frac{i}{\hbar}\int_0^t d\tau \mathcal{L}_I(\tau)\Big\rangle_B \sigma(0)\end{aligned} \tag{3.85}$$

Here we make the assumption that $\langle \hat{H}_{sb}\rangle = 0$ which makes $\langle \mathcal{L}_I(t)\rangle = 0$. This can be safely assumed by moving any non-zero part into the $\hat{H}_0$. This means we can write the equation for the RSDM as

$$\sigma_I(t) = \exp\Big\{\Big(-\frac{i}{\hbar}\Big)^2 \int_0^t d\tau_2 \int_0^{\tau_2} d\tau_1 \big\langle \mathcal{L}_I(\tau_2)\mathcal{L}_I(\tau_1)\big\rangle_B\Big\}\sigma(0) \tag{3.86}$$

To calculate an exponential superoperator is too difficult so we rewrite in the differential form

$$\dot{\sigma}_I(t) = \Big(-\frac{i}{\hbar}\Big)\int_0^t d\tau \big\langle \mathcal{L}_I(t)\mathcal{L}_I(\tau)\big\rangle_B \sigma_I(t) \tag{3.87}$$

From this we can see that the time derivative of the density matrix at time=t depends on the density matrix at time=t. This relationship we call time local nature. Now going back to the Schrödinger picture to get the full RSDM with respect to time

$$\sigma(t) = U_0(t)\sigma_I(t)U_0^\dagger(t) \tag{3.88}$$

As each depends on time we can take the time derivative

$$\begin{aligned}\dot{\sigma}(t) = &\Big(\frac{d}{dt}U_0(t)\Big)\sigma_I(t)U_0^\dagger(t) \\ &+ U_0(t)\sigma_I(t)\Big(\frac{d}{dt}U_0^\dagger(t)\Big) \\ &+ U_0(t)\dot{\sigma}(t)U_0^\dagger(t)\end{aligned} \tag{3.89}$$

The two U differentials are simply

$$-\frac{i}{\hbar}\hat{H}_0 U_0(t)$$
$$\frac{i}{\hbar}U_0^\dagger(t)\hat{H}_0$$

respectively. We have the $\hat{H}_0$ on both the left and the right side so we can write as

$$\dot{\sigma}(t) = -\frac{i}{\hbar}\big[\hat{H}_0, \sigma(t)\big] - \frac{1}{\hbar^2}\int_0^t d\tau U_0(t)\big\langle \mathcal{L}_I(t)\mathcal{L}_I(\tau)\big\rangle_B \Big\{U_0^\dagger(t)U_0(t)\Big\}\sigma_I(t)U_0^\dagger(t) \tag{3.90}$$

where the $\hat{I}$ operator is added in the curly brackets. We can therefore rewrite as

$$\dot{\sigma}(t) = -\frac{i}{\hbar}\big[\hat{H}_0, \sigma(t)\big] - \frac{1}{\hbar^2}\int_0^t d\tau U_0(t)\big\langle \mathcal{L}_I(t)\mathcal{L}_I(\tau)\big\rangle_B U_0^\dagger(t)\sigma(t) \tag{3.91}$$

We can see that the time evolution of the RSDM depends on two parts. The first term contains only the $\hat{H}_0$ and has no system-bath interaction. In addition, the bath has been traced out so it is simply the system. All the effect of the environment comes from the second term. The Liouville operators are propagated by the 0th order Hamiltonian. We want to evaluate the $U_s(t)\big\langle \mathcal{L}_I(t)\mathcal{L}_I(\tau)\big\rangle_B U_s^\dagger(t)$ which we call the dissipation kernel. The time-evolution operators denoted by $U_s(t)$ depend only on the system and not the bath. If we trace over the bath coordinates for the whole kernel we can add in bath time evolution operators in the form of $\hat{I}$.

$$\mathrm{Tr}_b\, U_b^\dagger(t)U_b(t)U_s(t)\mathcal{L}_I(t)\mathcal{L}_I(\tau)U_s^\dagger(t)\sigma(t)\otimes\rho_b^{eq} \tag{3.92}$$

Due to the cyclic property of the trace, the first $U_b^\dagger(t)$ term can be moved and the whole thing simplified to

$$\mathrm{Tr}_b\, U_0(t)\mathcal{L}_I(t)\mathcal{L}_I(\tau)U_0^\dagger\sigma(t)\otimes\rho_b^{eq} \tag{3.93}$$

We can now expand the Liouville operators as commutators to give

$$\mathrm{Tr}_b\, U_0(t)\big[U_0^\dagger(t)VU_0(t), \big[U_0^\dagger(\tau)VU_0(\tau), U_0^\dagger\sigma(t)\otimes\rho_b^{eq}\big]\big] \tag{3.94}$$

This can be simplified, bearing in mind that $V = \hat{H}_{sb}$

$$\dot{\sigma}(t) = -\frac{i}{\hbar}\left[\hat{H}_s, \sigma(t)\right] - \frac{1}{\hbar^2}\int_0^t d\tau \, \mathrm{Tr}_b \left[\hat{H}_{sb}(0), \left[\hat{H}_{sb}(\tau - t), \sigma(t) \otimes \rho_b^{eq}\right]\right] \tag{3.95}$$

The first term is called the coherent part and the second is the dissipative part due to the interaction between the system and bath. This is called the Redfield equation[159] and various methods for describing open quantum systems are derived from this. The most useful thing to note here is the total system density matrix $\hat{W}$ has been removed to make the equation solvable. Using the Redfield equation, you can now propagate the RSDM in time in sequential steps and determine observables at any value for time.

3.3.2 Forster regime

This is the opposite case where the coupling to the environment is much stronger than the inter-site coupling, resulting in all coherence being lost. In this regime the site basis remains and we can assume localisation of excitation energy on individual molecules. In such cases Förster resonance energy transfer (FRET) model[25] is an effective way of treating the dynamics.

Here the population on each site at time=t is given by the corresponding diagonal element of the density matrix $\rho_{ii}(t)$. These are governed by a set of rate equations which dictate transfer between each pair of sites.

$$\frac{d}{dt}\rho_{ii}(t) = -\sum_{j \neq i} k_{ij}\rho_{ii}(t) + \sum_{j \neq i} k_{ji}\rho_{jj}(t) \tag{3.96}$$

Rate of transfer from site i to j is given by k_{ij} and is weighted by the population on the donor site. In the FRET model, rate of transfer is given by

$$k_{ij} = \frac{|J_{ij}|^2}{2\pi}\int_{-\infty}^{\infty} d\omega \tilde{F}_i(\omega)\tilde{A}_j(\omega) \tag{3.97}$$

where $\tilde{F}_i(\omega)$ and $\tilde{A}(\omega)$ are the fluorescence and absorbance profiles of state i/j. The J term represents coupling and in the Förster regime this is simplified to the coulombic interaction. The

tilde denotes the Fourier transform and the functions in the time domain are represented as

$$F_i(t) = e^{-i(\varepsilon_i^0 - \lambda)t - g_i^*(t)}$$
$$A_i(t) = e^{-i(\varepsilon_j^0 - \lambda)t - g_j(t)} \tag{3.98}$$

The line shape function $g(t)$ links the acceptor and donor profiles back to wavelength as it is defined in terms of the energy gap correlation function from equation 3.45.

$$g_i(t) = \int_0^t dt_1 \int_0^{t_1} dt_2 C_i''(t_2) \tag{3.99}$$

3.3.3 Fermi's Golden Rule

We now look at the derivation of the Forster equation where the perturbation is the coupling between sites. We assume that we have solved the Schrödinger equation for the $0th$ order Hamiltonian,

$$H_0 \left|k\right\rangle = \varepsilon_k \left|k\right\rangle \tag{3.100}$$

If at time=0 the state is $|l\rangle$, we need to be able to find the probability of it being $|k\rangle$ at time=t. $|l\rangle$ is an eigenfunction of $\hat{H}_0$ so it stays stationary and we use V to evolve the state to a superposition of eigenstates. The probability of finding the system in state $|k\rangle$ is then given by

$$P_k(t) = |\left\langle k\right| U(t) \left|l\right\rangle|^2 \tag{3.101}$$

$\langle k| U(t) |l\rangle$ can then be expanded as

$$\left\langle k\right| U(t) \left|l\right\rangle = \left\langle k\right| \left\{ U_0(t) - \frac{i}{\hbar} \int_0^t d\tau U_I(t-\tau) V(\tau) U_0(\tau) \right\} \left|l\right\rangle \tag{3.102}$$

The states are eigenfunction of the $\hat{H}$ so if U is in the form

$$U_0(t) = e^{\frac{-i}{\hbar} H_0 t} \tag{3.103}$$

we can write equation 3.102 as

$$= \langle k| e^{-\frac{i}{\hbar}\varepsilon_l t} |l\rangle - \frac{i}{\hbar}\int_0^t d\tau \langle k| e^{-\frac{i}{\hbar}\varepsilon_k(t-\tau)} V_{kl} e^{-\frac{i}{\hbar}\varepsilon_l \tau} |l\rangle \tag{3.104}$$

The first term is removed as the inner product of the orthogonal eigenstates is 0

$$e^{-\frac{i}{\hbar}\varepsilon_l t} \langle k|l\rangle = 0 \tag{3.105}$$

The integral term can then be simplified with the term $\langle k| V |l\rangle$ and the t term taken out of the integral with respect to τ.

$$= -\frac{i}{\hbar} V_{kl} e^{-\frac{i}{\hbar}\varepsilon_k t} \int_0^t d\tau e^{-\frac{i}{\hbar}(\varepsilon_l - \varepsilon_k)\tau} \tag{3.106}$$

Here the $V_k l$ term represents a coupling between the k and l states and is an off-diagonal element. Equation 3.106 can then be integrated and simplified to

$$= -\frac{V_{kl}}{\varepsilon_k - \varepsilon_l}\Big[e^{-\frac{i}{\hbar}(\varepsilon_k - \varepsilon_l)t} - 1\Big] \tag{3.107}$$

If we use angular frequency as the energy gap where

$$\omega_{kl} = \frac{\varepsilon_k - \varepsilon_l}{\hbar} \tag{3.108}$$

and simplify using Euler's formula, we can find an expression for the probability of the system being in state k (equation 3.101).

$$P_k(t) = \frac{|V_{kl}|^2 t^2}{\hbar^2} sinc^2\Big(\frac{\omega_{kl} t}{2}\Big) \tag{3.109}$$

As the energy gap goes towards 0, the $P_k(t)$ goes to $\frac{|V_{kl}|^2 t^2}{\hbar^2}$, and it falls off as the energy gap increases. The width of the function depends on $\frac{2\pi}{t}$ as $sinc(\pi) = 0$. This means that as time increases, the height of the function also increases, but it also gets narrower which can be represented as a Dirac delta function. So when t is large, we can rewrite as

$$P_k(t) = \frac{2\pi}{\hbar}|V_{kl}|^2 \delta(\varepsilon_k - \varepsilon_l) t \tag{3.110}$$

This would suggest that as $t \to \infty$, so does $P_k(t)$ which cannot be as $P_k(t)$ cannot be greater than one. This relationship therefore falls off at larger values of t. This results in a period of time between the short times where the sinc function cannot be represented as a delta function, and longer times where $P_k(t)$ increases past 1 which we call the stationary phase. Because we defined $P_k(t)$ as 3.101, we can obtain the rate of transfer from state $|l\rangle$ to state $|k\rangle$ from

$$k_{kl} = \frac{d}{dt} P_k(t) \tag{3.111}$$

as Fermi's golden rule.

$$k_{kl} = \frac{2\pi}{\hbar} |V_{kl}|^2 \delta(\varepsilon_k - \varepsilon_l) \tag{3.112}$$

This shows that the rate of transfer from one state to another is related to how close in energy they are as well as some coupling factor. The $\delta(\varepsilon_k - \varepsilon_l)$ function is there to ensure the conservation of energy and any energy gap can only be overcome with an interaction with a third party (often a bath), to either give or receive energy. We can now see how equation 3.112 gives us the Forster equation with the delta function replaced by the overlap of $\tilde{F}_i(\omega)$ and $\tilde{A}(\omega)$.

3.3.4 Our approach

For the model used in this work, FRET is taken as the standard approach for energy transfer. This is because the sites in our system exhibit weak coupling and so experience rapid dephasing. However, there are some small 'blocks' of Chls which are much more strongly coupled. Here FRET does not give a good description of the dynamics and so we employ a 'block diagonalisation' method to account for the coherence and movement away from the site basis.

Light harvesting complexes will typically exist in an intermediate range where electron-phonon couplings are roughly equivalent to inter-pigment coupling. In such a system there are inaccuracies involved with treating either as the perturbation and so there are a number of theories which exist to deal with this. For the purposes of this thesis we will simply describe the approach taken within. For the light harvesting complexes studied here: LHCII and CP29, the majority of the dynamics are described well by the slow Förster approach. However there are certain groups or pairs of Chls which are particularly strongly coupled. In these cases, a

new 'domain' is set up, where the part of the Hamiltonian describing the block of pigments which exhibits coherence is treated separately. The block is diagonalised to determine a new basis which represents the excited states. Couplings between the remaining sites and these new excitonic states are then calculated and a simple instantaneous thermal equilibration within the block is assumed.

The energy transfer is modelled as changing site probabilities where a series of equations detailing the rate of EET in each direction (acording to Förster theory) adjusts these probabilities towards a steady state. In this way we can see the link between, structure, coupling, energy transfer and populations of excited state energy on each pigment. We can then make predictions about what happens to the energy in experimental conditions.

Chapter 4

Carotenoids

The general structure and function of Cars was discussed in section 1.3.2. We will therefore discuss the important spectroscopic properties which dictate the behaviour of Cars in light harvesting complexes. The absorption spectra (figure 4.1a) of Cars reveals a large peak in the low energy range of the visible spectrum. This corresponds to the S_0 (ground states) $\rightarrow S_2$ transition and has an extinction coefficient (ε) in the order of 10^5 M^{-1} cm^{-1}[160]. This signal typically exhibits a three peak structure, corresponding to the three lowest energy vibrational states ($0-0$, $0-1$, $0-2$). In addition, there is a set of many peaks in the higher energy blue to UV region accounting for the excitations to the higher order states (S_n). These may play a role in UV protection but are unimportant for light harvesting and NPQ. They do however, prove useful for determining the properties of the lower energy states. Finally there are a number of states which are optically 'dark' and do not show up on the absorption spectra. Interesting this includes the lowest energy singlet state (S_1).

I will describe the symmetries of the states in section 4.3 in detail and will just highlight the key elements here. The states are described by the symmetry group C_{2h} which stems from an idealized way of describing linear polyenes, the parent analogues of Cars. This means it has a 2-fold rotational symmetry as well as a perpendicular mirror plane and crucially a centre of inversion. This gives the states either A_g or B_u symmetries with the parity symbol (g/u) denoting symmetric or non-symmetric under inversion respectively. States are then divided into

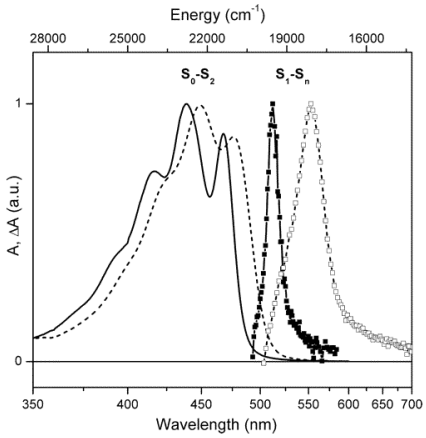

(a) Absorption spectra of Vio. $S_0 \rightarrow S_2$ (ground-state absorption) and $S_1 \rightarrow S_N$ (excited-state absorption)[161].

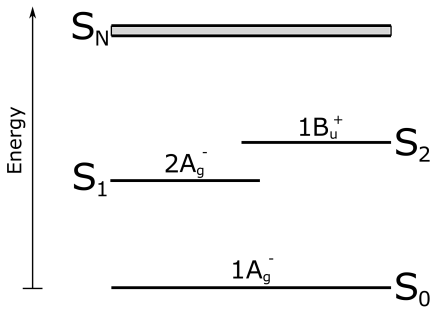

(b) Energy levels of key Car molecular orbitals

Pariser symmetry groups of (+) or (−). This stems from models of linear polyenes and gives an indication of the states ionic (+) or covalent (−) nature. It also crucially indicates whether the state is made up primarily of a single excitation determinant or a double. This leaves us with four possible symmetry states: nA_g^+, nA_g^-, nB_u^+, nB_u^-, with the n being the number of the state when ordered according to energy (the principle quantum number). With the ground state being $1A_g^-$, selection rules suggest that only excitations to nB_u^+ states should be allowed due to the Laporte rule which states that transition from orbitals with the same angular momentum are not allowed. These labels prove useful to explain certain spectroscopic properties of the states but for a couple of reasons are not as binding as is often suggested. The Pariser labels are based on models of polyenes which assume zero differential overlap between the p_z orbitals of the conjugated chain. In addition the C_{2h} symmetry is broken in the case of Cars due to their addition complexity with respect to linear polyenes. In reality the symmetry group is more often C_2 or even C_1. This will be discussed further in the section on symmetry (4.3).

4.1 The S_2 energy

We will start with a relatively brief discussion of the S_2 state ($1^1B_u^+$) as it does not play a major role in the research part of this thesis. A transition from the ground state is responsible for the

strong absorption peak in the blue-green spectral region. The $S_0 \rightarrow S_2$ energy gap is reduced with increased conjugation length (N) and for naturally occurring Cars with a $N = 7 \rightarrow 13$ the peak is between 475 and 525 nm ($\sim$ 2.2 eV) giving Cars their bright colours of yellow to orange. Solvents with high polarizability can red-shift the S_2 peak as much as 40 nm.

It is typically characterized by a triple peak arising from vibrational coupling from the C-C and C=C stretching modes, though this detail can often be lost on Cars where the interaction between the methyl groups on the side of the conjugated chain is large. An example of this is β-carotene for which the conjugation extends into the end rings. This causes the ring to be particularly stable in a *cis* conformation[162] where it has a strong steric interaction with the nearest methyl. This interaction leads to a broader distributions of conformers, resulting in the observed reduction in vibrational structure[163, 164]. For this reason *cis*- Cars often have particularly low resolution. The energy gap between these peaks is roughly ~ 1350 cm^{-1} resulting from the two symmetric vibrational modes of the conjugated chain ~ 1150 cm^{-1} (C-C stretch) and ~ 1600 cm^{-1} (C=C stretch)[161].

4.2 The dark states

As well as the S_2 state, there is another 'dark state' which is integral to the Cars excited state dynamics. The lowest energy singlet state (S_1) is optically dark and therefore does not show up on the absorbency profile. In addition there is a signal which can be found on the shoulder of the S_1 called the S^*. Finally there are two more dark states which are just above the S_2 in energy, but depending on the Car, can be lower to interact with the S_2.

4.2.1 S_1 energy

The energy of the S_1 state ($2^1A_g^-$) is much more difficult to determine as it is optically forbidden. There have been many techniques employed to provide accurate energy gaps. As with the S_2, the energy goes down with increased conjugation, though at a steeper rate. In shorter Cars ($N < 8$), the energy gap is low enough between states to allow for sufficient mixing to see a S_1 peak and so the energy can be reasonably accurately determined from simple absorption spectra. The change in energy as the conjugation length increases enabled early guesses at the S_1 energy of longer

Cars via extrapolation. Cosgrove *et al.*[165] and DeCoster *et al.*[166] used this relationship to put the S_1 energy of β-carotene at between 13000 and 14000 cm^{-1}. These guesses were further improved by the application of the energy gap law which relates the energy of a state with its non-radiative decay leading to a refined S_1 energy of 14100 cm^{-1}[167].

One method for actually measuring the energies of longer Cars was through the distinctive $S_1 \rightarrow S_N$ transitions, as where the N state was of B_u symmetry the transition from both the ground state and the S_1 state would both be visible. However, this proved to be ineffective as these peaks are so broad as to remove any vibrational detail and so the $0-0$ transition is impossible to obtain. In addition to this there is often heavy overlap with various transitions making the peaks even harder to read[168, 169].

After this, efforts in determining the S_1 energy were mostly concentrated on increasing the sensitivity of the detection apparatus so that the small S_1 peak could be detected. The low quantum yield of the order of 10^{-5} to 10^{-7} as well as overlap with the dominating S_2 peak made this particularly difficult. The $0-0$ origin of the $S_0 \rightarrow S_1$ peak is the part that is obscured by the red tail of the strong S_2 emission band. With the $0-2$ peak being most visible, the $0-0$ transition energy has to be approximated based on knowledge of the vibrational splitting. However, useful energies have been measured this way with Anderson *et al.*[170] positioning the S_1 energy of β-carotene in CS_2 at 14200 ± 500 cm^{-1}. Despite having a high error, this is in good agreement with the energy-gap law approximations.

A further steady state technique, developed to obtain S_1 energies is based on Raman spectroscopy. This is done by observing the signature Raman peaks of around 1500 and 1150 cm^{-1} corresponding to the C=C and C-C stretching modes along the conjugated chain. When the excitation light is in resonance with an electronic transition of the studied molecule, the Raman peaks are greatly enhanced. By tuning the excitation light, a full set of excited states can be obtained. Hashimoto *et al.*[171] used this technique to derive a S_1 energy of 14500 cm^{-1} for β-carotene which, given its reasonable agreement with expected results, prompted the extension to further Cars. This technique also has the issue of the S_1 peak being obscured by the much larger S_2 peak. However, contrary to fluorescence measurements, signals can be reduced by self-absorption[172]. Thus by proper choice of concentration and the optical geometry of the experiment, the S_2 signal can be reduced to show the S_1 0-0 transition[172].

A third method involves using the $S_1 \rightarrow S_2$ transition in conjunction with $S_0 \rightarrow S_2$. A femtosecond excitation pulse, excites the S_2 state which then rapidly relaxes to S_1. The S_1 S_2 resonance can then be found by scanning the probe pulse according to the known relaxation times of the S_1 and S_2 states. This has proved to be effective for measuring S_1 energies. Incidentally it has also proved useful for exploring the $S_1 \rightarrow S_2$ gap, and has shown how complicated the relationship between state energy, conjugation length and functional groups can be. One interesting finding was the surprising S_1 energies of Vio and Zea. The energy of Zea ($N = 11$) is quite close to the expected using the energy gap law and extrapolation. Vio should be higher in energy due to its shorter conjugation length ($N = 9$) at ~ 15000 cm^{-1}, however, it was found to be around 14470 cm^{-1}[173].

The main issue with these methods is that they rely on specific solvents in order to detect certain peaks. A final two-photon excitation method for determining the S_1 energy goes some way to circumvent this. Early attempts to use two-photon excitation spectra proved promising but relied on the detection of the S_1 state fluorescence and so could only be used for Cars with an allowed S_1 such as Peridinin[168, 174]. This method has since been improved by pairing the two-photon excitation with detection of the $S_1 \rightarrow S_N$ transition[175, 176]. However, the 0-0 transition proved difficult to determine due to poor signal/noise ratios. The most useful application of the two-photon techniques was to apply it to Cars within light-harvesting complexes. Here the excitation can be paired with detection of emission from the (B)Chls as a consequence of EET. This has allowed some measurements of the S_1 state in its native environment such as LHCII[177, 176]. They determined the Lut S_1 energy at 15100 and more recently at 15300 cm^{-1}.

4.2.2 S_1 lineshape

The spectral lineshape describes the features of an energy signal. In the case of the S_1, there is no signal as the transition is optically forbidden so we call the shape it would produce a density of states (DOS). It can be found using a number of different procedures which mirror that of the energy. One particularly useful is using 2-photon absorption to create an absorption spectrum of the 2-electron S_1 state. The work of Walla *et al.*[176] provides us with such a spectrum of Lut

in octanol. The first thing to note is the broadness of the signal (figure 4.2). If it were to be fit with a simple gaussian, the full width at half height would be 2880 cm^{-1}. This tells us that there is a large reorganisation energy (λ). When the site is populated to a higher vibrational level, large nuclear shifts create the drop in energy as the state falls to the lowest vibrational energy. This also has the effect of creating a large Stoke's shift as it is equal to twice the reorganisation energy.

In my initial work[178] I used an overdamped Brownian oscillator to fit the entire two-photon line-shape for the spectral density in order to replicate this DOS.

$$C''_{car}(\omega) = 2\lambda_0 \frac{\omega\gamma}{\omega^2 + \gamma^2} \tag{4.1}$$

where the parameter γ, determines the correlation time of the site energy fluctuation and is fixed at $\gamma = 53$ cm^{-1}[179, 180]. The reorganisation energy is taken at a range of values from the lowest at 300 cm^{-1} to the highest at an enormous 3400 cm^{-1}. This spectral density posed two problems. The first was that in order to properly fit the spectra, the reorganisation energy had to be at the upper end of the range, but this is a totally unrealistic value and conflicts with other groups modelling of the DOS[181]. The second is that it does not take the detail caused by the vibrational levels into account at all and smooths over the whole signal. Our group (V. Balevičius Jnr.) therefore produced a new spectral density to solve these problems. The vibrational peaks associated with the C-C and C=C stretching modes can be very useful for describing various spectroscopic signals of Cars. With this is mind, these two stretching modes were used to describe the vibrational peaks of the S_1 signal. An ansatz-spectral density was constructed with two underdamped terms to describe these features plus an overdamped term to describe the remaining degrees of freedom.

$$C(\omega) = \sum_{i=1,2} 2\lambda_i \frac{\omega\omega_i^2\gamma_i}{(\omega^2 - \omega_i^2)^2 + \omega^2\gamma_i^2} + 2\lambda_0 \frac{\omega\gamma_0}{\omega^2 + \gamma_0^2} \tag{4.2}$$

In this thesis we study Lut, Neo and Vio and the reported values for the single (ω_2) and double (ω_1) stretching modes of each are used[182]. Lut: $\omega_1 = 1522$ cm^{-1}, $\omega_2 = 1156$ cm^{-1}, Neo: $\omega_1 = 1530$ cm^{-1}, $\omega_2 = 1156$ cm^{-1}, Vio: $\omega_1 = 1524$ cm^{-1}, $\omega_2 = 1156$ cm^{-1}. The remaining parameters

were obtained from a visual fitting of the 2-photon absorption spectrum: $\lambda_1 = \lambda_2 = 900$ cm^{-1}, $\gamma_1 = \gamma_2 = 300$ fs for the underdamped part and $\lambda_0 = 450$ cm^{-1}, $\gamma_0 = 53$ fs for the overdamped part. Both of these spectral densities are used within my work and the particular one used will be specified in each instance. The fitting for Lut can be seen in figure 4.2

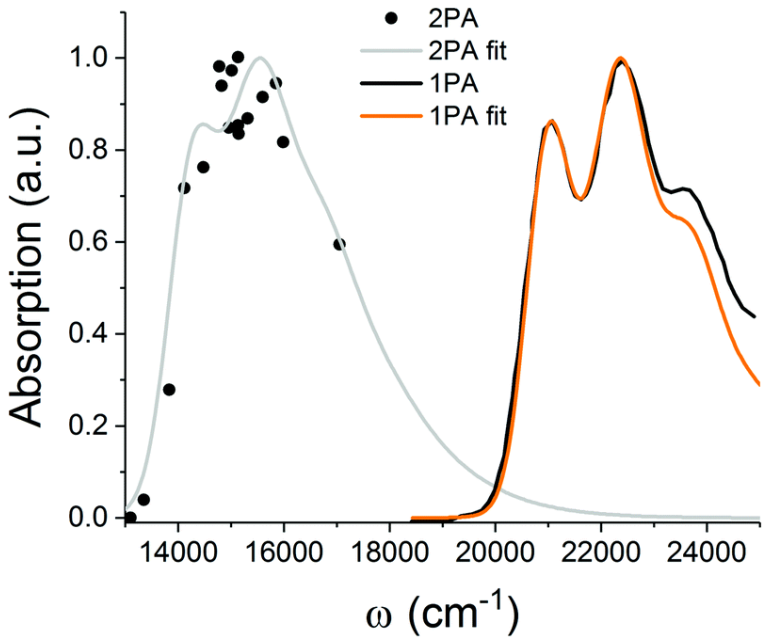

Figure 4.2: The fitting process of a spectral density to the two-photon absorption (2PA) of Walla et al.[176] and the S2 absorption (1PA) spectra.

4.2.3 Further states

Global analysis studies of the $S_1 \rightarrow S_N$ peak at 590 nm for the long Car spirilloxanthin[183], revealed a small shoulder at around 540 nm. This was tentatively assigned to new state termed S^* and showed a significantly slower relaxation time than its neighbouring S_1 state (6 ps compared to 1.4 ps). The peak is made more significant in longer Cars and is significantly more pronounced when incorporated into light-harvesting proteins. This shoulder has also been proposed to arise from a 'hot' ground state as a result of decay from $S_1 \rightarrow S_0$. This rapid process releases energy non-radiatively and so a highly vibrationally excited ground state is possible. The subsequent cooling is dependent on the ability for the energy to transfer away and through the solvent. This theory is supported by the high dependency of the amplitude of the S^* shoulder on the

solvent[184, 161]. For this reason it may be more appropriate to term it the S^* signal rather than state until further investigation reveals otherwise. While the nature S^* signal is an interesting problem and it may well have some connection to NPQ, understanding on it is currently very limited and so it was neglected for this work. It is my belief that it is simply incidental and results from the rapid non-radiative depopulation of the S_1 state.

There are two additional 'dark' singlet states which may have some effect on the photophysics of Cars. These are $1B_u^-$ and $3A_g^-$ which lie just higher in energy than S_2. They are of particular note as their energy lowers with respect to S_2 as the conjugation length increases. At $N > 10$ they are even lower in energy. This means there can be significant mixing of the states which may explain some of the dissipation rates for the S_2 state. They are both dark because, like the S_1, they are made up of two coupled triplet states resulting in a primarily two-electron nature. This correlation is denoted by the (-) Pariser's label. However, their effects do not have much relevance to this thesis and so the reader is directed to literature for further reading[185].

4.2.4 Relaxation schemes

The radiative $S_2 \rightarrow S_0$ lifetime can be calculated by the Strickler-Berg equation

$$\tau^{-1} = 2.88 \times 10^{-9} n^2 \frac{\int_{\Delta v_e} F(v) dv}{\int_{\Delta v_a} F(v) v^{-3} dv} \varepsilon(v) d \ln v \tag{4.3}$$

which gives an approximation of the lifetime of a state in the absence of any deactivation processes. Here τ is the radiative lifetime, n is the reactive index of the solvent, Δv_e and Δv_a are the experimental limits of the absorption and emission bands, ε is the extinction coefficient, v is the wavenumber and $F(v)$ describes the spectral distribution of the emission in photons per wavelength interval. It gives a lifetimes in the range of nanoseconds which in reality is almost completely out-competed by the rapid internal conversion to the S_1 state. Fluorescence up-conversion and transient absorption techniques have been employed, establishing this internal-conversion to happen in the range of 50-300 fs[161]. Because increasing the polarizability of the solvent reduces the S_2 energy, the S_2-S_1 energy gap is reduced and so the internal conversion is sped up. However, increasing the conjugation length does not produce this simple relationship. While it does produce the same reduction in S_2-S_1 energy gap, the change in internal-conversion

rate varies with Cars and does not always increase. It has been proposed that this is due to an variable number of accepting vibrational modes which compensate for energy gap changes. Nevertheless, dissipation from the S_2 state is always predominated by conversion to the S_1 state.

The rapid $S_1 \rightarrow S_0$ internal conversion is relatively well understood and is explained by their same symmetry. This causes strong vibrational coupling between the two states as both share the same a_g stretching modes. This was confirmed by femto-second transient absorption spectroscopy combined with picosecond transient Raman spectroscopy[161]. When the conjugated chain is labelled with ^{13}C, the lifetime significantly increases due to a distortion of the C=C stretching modes. This same increase is not observed for non-conjugated carbons or with ^{2}H labeling.

This cannot be used to explain the $S_2 \rightarrow S_1$ transfer rate as they have opposite symmetry. Therefore coupling of the vibrational modes is symmetry forbidden. The $50-300$ fs[161] rate was initially proposed to be due to a conical intersection but this on its own was shown to be unlikely as the transfer is predominated by the low energy vibrational states and any conical intersection could involve a large rearrangement from the 0 position[186]. It has since been shown likely that the conical intersection is aided by state mixing of the S_2 state with the $1B_U^-$ state which in longer Cars is almost the same energy[187]. Mixing with this state could then induce vibronic coupling with S_1 state due to the same (-) Pariser's symmetry.

4.3 Symmetry

We can see from the molecular orbital diagram that in general, the S_1 is the lowest singlet excited state, followed by the S_2 and two further singlet states. Above that we will simply describe other singlet states as S_n as they have no influence over the excited state dynamics in light harvesting systems. In the weak electron correlation limit, the states would arrange themselves alternating between A_g and B_u as the energy increases. However, the effects of correlation push (-) states down in energy and so this ordering is disrupted. The result is the second A_g state falls below the first B_u state[185] (figure 4.1b). The $1^1B_u^+$ state can easily be described in terms of molecular orbitals by a single $HOMO \rightarrow LUMO$ transition. However, the $2^1A_g^-$ state needs the involvement of highly excited configurations to describe it with any accuracy. If double excitations are included the reverse ordering is established and we see that

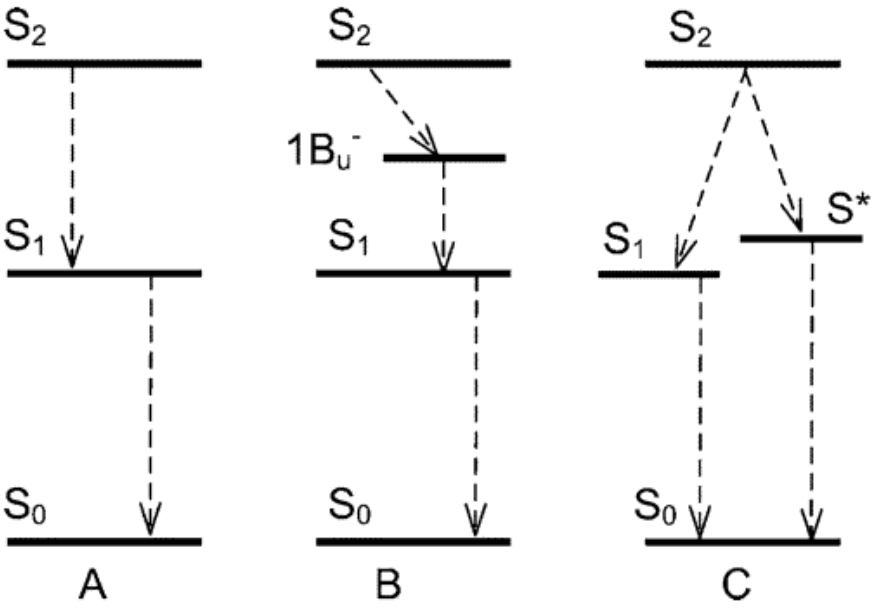

Figure 4.3: A schematic of three proposed relaxation schemes by Polivka and Sundström [161]

the $2^1A_g^-$ state is mainly made up of double $HOMO, HOMO \rightarrow LUMO, LUMO$. In order to achieve quantitatively accurate energies for this state, higher orders of excitations should be included but the state remains predominantly the same double excitation. This double excitation singlet state can also be seen as the coupling between two 1^3B_u triplet states. Aside from the ionic B_u^+ and the covalent A_g^- states mentioned, the final relevant dark state is the $1^1B_u^-$ state, made up of a combination of the triplet 1^3B_u and 1^3A_g. In longer Cars ($N > 9$), where the $1^1B_u^-$ state is lower in energy, it can interact with the B_u^+ (S_2) state.

There are a number of dark states which are dark due to two possible reasons. Those with (-) Pariser's symmetry have a two-electron excitation from the ground state and so are forbidden because of the Slater-Condon rule, others are simply dark as they break the symmetry selection rules. The S_1 ($2^1A_g^-$) state is dark due to both reasons. The Pariser's label indicates that the state is primarily made up of a doubly excited configuration. In addition any single electron character is not allowed as it is the same symmetry as the ground state and so would break the Laporte rule.

4.3.1 Alternacy symmetry

The Pariser symmetry labels originate from a molecule having particle hole symmetry. If a molecule has particle-hole symmetry then it is invariant under transformation of a particle into a hole. For this to be true, there are two major requirements. The first is that the lattice must be composed of two interconnected sublattices with only nearest neighbour coupling (figure 4.4) . This is held true in Cars by the alternating nature of the short-long bonds in the conjugated chain. Each carbon can be thought of as a site which interacts with two sites on either side of it, both belonging to the opposite sublattice. The result is that the energy levels are symmetric about the midpoint between the HOMO and LUMO. This means that the occupied orbitals going down in energy mirror the unoccupied orbitals going up in energy. The second is that the electron-electron interaction must be balanced by the electron-lattice couplings. This originates from the conjugated nature increasing the electron-electron interaction. These requirements are met perfectly in approximate models of linear polyenes such as Pariser-Par-Pople but in Cars it is broken down considerably. This stems from a different electron-electron interaction at the middle of conjugated chain compared to the ends. Functional groups containing hetero-atoms also disrupt this balance. However, the approximations are still useful as they describe the covalent/ionic nature of the states and predict the double electron nature of the S_1 state. This is crucial and we will now explore the key difference between a state which is primarily made up of a single excitation determinant compared to a double excitation.

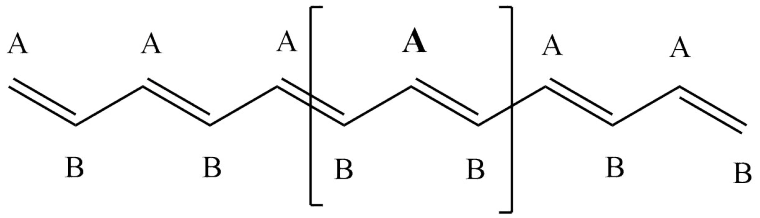

Figure 4.4: A schematic of a polyene (representing the Car backbone). Here we see how the conjugated chain can be thought of as two interconnected sublattices: A and B. Each carbon can then be assumed to have nearest neighbour interactions only. This is represented by the bold carbon from the A sublattice which can be described fully by the information inside the bracket

4.3.2 Single and double excitations

The transition density matrix (TDM) in the atomic orbital basis provides a useful way to map the charge localisation change during an electronic transition. From the ground state to an excited state we can represent it in the second quantization formalism as

$$T_{ij} = \langle GS| \, c^{\dagger}_{i\sigma} c_{j\sigma} \, |EX\rangle \tag{4.4}$$

between states i and j. The creation and annihilation operators labelled c are in the atomic orbital basis. Now when treating the states using CI singles, we can represent the ground and excited sate functions as

$$\begin{aligned} |GS\rangle &= |\Psi_0\rangle \\ |EX\rangle &= \sum_{\substack{a\in \ occ \\ r\in \ virt \\ \sigma'}} C^{r\sigma'}_{a\sigma'} a^{\dagger}_{r\sigma'} a_{a\sigma'} \, |\Psi_0\rangle \end{aligned} \tag{4.5}$$

where the creation and annihilation operators labelled a are in the molecular orbital basis. We can now rewrite equation 4.4 as

$$T_{ij} = \sum_{\substack{a,r \\ \sigma'}} C^{r\sigma'}_{a\sigma'} \, \langle \Psi_0| \, c^{\dagger}_{i\sigma} c_{j\sigma} a^{\dagger}_{r\sigma'} a_{a\sigma'} \, |\Psi_0\rangle \tag{4.6}$$

This is a useful way of expressing the transition as integrals are easier to compute when expressed as annihilation and creation operators. This is providing they are in the normal order, where all annihilation operators are on the right and all creation operators are on the left. However, the current form is expressed in both the atomic and molecular orbital basis. A molecular orbital can be expressed as a linear combination of atomic orbitals and vice versa.

$$\chi^{MO}_i = \sum_m \beta_{mi} \phi^{AO}_m \tag{4.7}$$

$$\phi^{AO}_m = \sum_i \alpha_{im} \chi^{MO}_i \tag{4.8}$$

This relationship is unitary as in $\beta_{mi} = \alpha_{im}$ and is true for both cre. and ann. operators. This means we can rewrite in terms of molecular orbitals

$$T_{ij} = \sum_{\substack{a,r \\ m,m' \\ \sigma'}} C_{a\sigma'}^{r\sigma'} \beta_{mi} \beta_{m'j} \langle \Psi_0 | \, a_{m\sigma}^\dagger a_{m'\sigma} a_{r\sigma'}^\dagger a_{a\sigma'} \, | \Psi_0 \rangle \tag{4.9}$$

We want to write this in normal order so we swap the middle two cre. and ann. operators according to the anti-commutation rules ($a_{m'\sigma} a_{r\sigma'}^\dagger = \delta_{m'r}\delta_{\sigma\sigma'} - a_{r\sigma'}^\dagger a_{m'\sigma}$).

$$T_{ij} = \sum_{\substack{a,r \\ m,m' \\ \sigma'}} C_{a\sigma'}^{r\sigma'} \beta_{mi} \beta_{m'j} \Big\{ \delta_{m'r}\delta_{\sigma\sigma'} \langle \Psi_0 | \, a_{m\sigma}^\dagger a_{a\sigma'} \, | \Psi_0 \rangle - \langle \Psi_0 | \, a_{m\sigma}^\dagger a_{r\sigma'}^\dagger a_{m'\sigma} a_{a\sigma'} \, | \Psi_0 \rangle \Big\} \tag{4.10}$$

We can see that the second term evaluates to identically 0 as $a_{r\sigma'}^\dagger$ is trying to eliminate from orbital r which in $\langle \Psi_0 |$ is unoccupied. We then turn to the first term which can be rewritten as

$$\langle \Psi_0 | \, a_{m\sigma}^\dagger a_{a\sigma'} \, | \Psi_0 \rangle = \langle \Psi_0(m,\sigma) | \Psi_0(a,\sigma') \rangle \tag{4.11}$$

If we assume the wavefunctions to be orthonormal, to get a non-zero answer we must assume that $m = a$ and $\sigma = \sigma'$. We can therefore finally represent the density spin matrix as

$$\begin{aligned} T_{ij}(\sigma) &= \sum_{a,r} C_{a\sigma'}^{r\sigma'} \beta_{mi} \beta_{m'j} \delta_{m'r} \delta_{ma} \delta_{\sigma\sigma'} \\ &= \sum_{a,r} C_{a\sigma'}^{r\sigma'} \beta_{ai} \beta_{r'j} \end{aligned} \tag{4.12}$$

We now have a way of calculating the transition spin matrix as we can easily obtain the CI coefficients of each CI configuration as well as the atomic orbital coefficient for each molecule orbital.

When higher orders of excitations are taken into account as is necessary for the S_1, this becomes much more convoluted though it still follows the same processes. Here the ground state

is represented as

$$\langle GS| = D_0 \langle \Psi_0| + \sum_{\substack{a,r \\ \sigma}} D_{a\sigma}^{r\sigma} \langle \Psi_{a\sigma}^{r\sigma}| + \sum_{\substack{a,b \\ r,t \\ \sigma\sigma'}} D_{a\sigma,b\sigma'}^{r\sigma,t\sigma'} \left\langle \Psi_{a\sigma,b\sigma'}^{r\sigma,t\sigma'} \right| + \dots \tag{4.13}$$

and the excited state in a similar way as

$$|EX\rangle = C_0 \langle \Psi_0| + \sum_{\substack{A,R \\ \sigma}} C_{A\sigma}^{R\sigma} \left|\Psi_{A\sigma}^{R\sigma}\right\rangle + \sum_{\substack{A,B \\ R,T \\ \sigma\sigma'}} C_{A\sigma,B\sigma'}^{R\sigma,T\sigma'} \left|\Psi_{A\sigma,B\sigma'}^{R\sigma,T\sigma'}\right\rangle + \dots \tag{4.14}$$

The transition from ground to excited state will constitute all possible combinations of these terms. The Car S_1 state is primarily made up of a two-electron transition from the reference determinant (the dominant determinant of the ground state). We can therefore describe the TDM for the S_0 to S_1 transition as mainly

$$T_{ij} = \langle \Psi_0| c_{i\sigma}^\dagger c_{j\sigma} \left|\Psi_{A\sigma,B\sigma'}^{R\sigma,T\sigma'}\right\rangle \tag{4.15}$$

Again we write in terms of ann. and cre. operators and expand in the molecular orbital basis.

$$T_{ij} = \sum_{m,m'} \beta_{mi}\beta_{mj} \langle \Psi_0| a_{m\sigma}^\dagger a_{m'\sigma} a_{t\sigma'}^\dagger a_{b\sigma'} a_{r\sigma'}^\dagger a_{a\sigma'} |\Psi_0\rangle \tag{4.16}$$

We then start the process of rearranging into normal order

$$= \sum_{m,m'} \beta_{mi}\beta_{mj} \Big\{ \delta_{m't}\delta_{\sigma\sigma'} \langle \Psi_0| a_{m\sigma}^\dagger a_{b\sigma'} a_{r\sigma'}^\dagger a_{a\sigma'} |\Psi_0\rangle - \langle \Psi_0| a_{m\sigma}^\dagger a_{t\sigma'}^\dagger a_{m'\sigma} a_{b\sigma'} a_{r\sigma'}^\dagger a_{a\sigma'} |\Psi_0\rangle \Big\} \tag{4.17}$$

We can immediately see that the second term is attempting to annihilate an electron from orbital t of the reference determinant. This does not exist and so the second term is 0. The first term

can then be arranged again into normal order to give

$$= \sum_{m,m'} \beta_{mi}\beta_{mj} \Big\{ \delta_{m't}\delta_{\sigma\sigma'}\delta_{br}\delta_{\sigma'\sigma'} \langle \Psi_0 | a^\dagger_{m\sigma} a_{a\sigma'} | \Psi_0 \rangle - \\ \delta_{m't}\delta_{\sigma\sigma'} \langle \Psi_0 | a^\dagger_{m\sigma} a^\dagger_{r\sigma'} a_{b\sigma'} a_{a\sigma'} | \Psi_0 \rangle \tag{4.18}$$

While it is now in normal order both terms are equal to 0. The first has a δ_{br} term which has to be 0 as b is an unoccupied orbital and r is occupied and so they cannot be the same. The second has an annihilation operator trying to annihilate an electron in orbital r of the reference determinant. There are no electrons in the unoccupied r orbital and so this cannot happen.

We have discussed at the top of this chapter, selection rules arising from symmetry cause the $S_0 \rightarrow S_1$ transition to be not-allowed. However, this shows us that the forbidden nature of this transition arises from a more fundamental reason. The S_1 state has almost no charge density at all and its 2-electron transition is the root cause. As a result, any bending of the molecule to reduce its symmetry will only have a minor effect on the $S_0 \rightarrow S_1$ transition.

4.3.3 Mixing the states

The reason for the S_1 ($2^1A_g^-$) being lower than the S_2 is the electron correlation, brought about by the particle-hole symmetry. Therefore any geometric alterations to the molecule which reduces this symmetry will likewise reduce electron correlation and bring the S_1 state up in energy. As the energy gets closer to the S_2 there will be some mixing between the states. This will introduce addition single electron character to the S_1 and significantly increase the transition density. However, as the S_1 dipole is never directly observable, it is unlikely that deformations in the protein are large enough to enact a significant amount of this mixing.

Chapter 5

S_1-Chlorophyll transfer

We have discussed why the S_1 state transition has a virtually zero transition density moment. However, there is repeated experimental evidence that it couples to the pool of Chl Q_y states. We will now discuss how this occurs including the various mechanisms proposed for the transfer of energy as well as the requirements for the necessary amount of transfer.

The transfer between S_1 and Q_y is important for Cars to act as a light harvester as the rapid relaxation from the S_2 state to the S_1 would mean that most ($\sim$ 60% according to van Amerongen *et al.*[30]) of the energy absorbed, by the S_2 state, would be lost through relaxation to the S_1 followed by non-radiative decay. There is also rapid transfer between the heavily allowed S_2 state and the Chl Q_x state which is very similar in energy. This is extremely rapid transfer, and has to be in order to compete with the $\sim$ 300 ps internal conversion from S_2 to S_1.

Energy transfer is dependent one two things: the overlap of the donor fluorescence (Density of States for non-fluorescing pigments) with the acceptor absorption profile and the coupling. The overlap changes with the state energy, the reorganisation energy and the shape of the spectral density. The coupling changes with the transition charges (often approximated with dipoles) associated with the specific states of the donor and acceptor pigments. The way in which we make predictions on what happens with light-harvesting and NPQ is with models which are in essence a series of transfer rates: inter- and intra- pigment energy transfer. It is therefor vital that we parameterise the spectral overlap and calculate the coupling as well as we can.

5.0.1 Neglecting overlap and dexter

Coupling is made up of two parts: the coulombic interaction with a correction for the exchange repulsion.

$$W_{DA} = J_{DA} + K_{DA} \tag{5.1}$$

In the majority of studies the exchange parts is neglected as it is assumed to be much smaller than the exchange part (and is often neglected for this reason). This is due to the exponential distance dependence created out of the multiple centre integral, resulting in an exchange part is only appreciable at very short inter-molecular distances. However, the validity of its exclusion could be disputed in the case of Cars, as they only exhibit appreciable coulombic coupling at short intermolecular distances, where the exchange interaction could be significant. The question is therefore if the densely packed LHCII constitutes short enough distances between pigments to necessitate the inclusion of exchange.

The coulombic part is defined as

$$J_{DA} = \sum_{\substack{i,j \in D \\ k,l \in A}} J_{ij,kl} T^D_{ij} T^A_{kl} \tag{5.2}$$

where $J_{ij,kl}$ is defined as

$$J_{ij,kl} = \int\int d^3r d^3r' \psi^*_i(r)\psi_j(r) \frac{1}{|r - r'|} \psi^*_k(r')\psi_l(r') \tag{5.3}$$

where $\psi_i(r)$ and $\psi_j(r)$ are atomic orbitals on the donor molecule and $\psi_k(r')$ and $\psi_l(r')$ are atomic orbitals on the acceptor. The T terms are elements of the transition density matrix in the atomic orbital basis, as defined in section 4.3.2. The ψ terms are atomic orbitals creating multiple centre integrals. As we have previously discussed, the transition density matrix elements are almost 0 due to the ground state being primarily the reference determinant and the S_1 state being primarily a double excitation. The exchange terms looks like

$$K_{DA} = -\frac{1}{2} \sum_{\substack{i,j \in D \\ k,l \in A}} K_{ij,kl} T^D_{ij} T^A_{kl} \tag{5.4}$$

where

$$K_{ij,kl} = \int\int d^3r d^3r' \psi_i^*(r)\psi_j(r')\frac{1}{|r-r'|}\psi_k^*(r')\psi_l(r) \tag{5.5}$$

We therefore see that the exchange interaction is also dependent on the density matrix elements which are almost 0. We can see that the question of neglecting the exchange interaction is therefore the same for Cars as it is the Chls. Previous Chl only models have assumed a 0 exchange interaction and have reproduced all steady-state and time-resolved spectra. The distances between Chl clusters are equivalent to the distances between Chl and Car and so we can use the Chl models as a test for the exclusion of the exchange interaction in our calculations.

The overlap interaction is a correction to the coupling when the states which describe the initial and final situation, in terms of donor and acceptor molecules, are not orthogonal.

$$|Initial\rangle = |EX_D\rangle\,|GS_A\rangle \qquad\qquad |Final\rangle = |GS_D\rangle\,|EX_A\rangle \tag{5.6}$$

The coupling including the overlap correction is then

$$W_{DA}^{overlap} = \frac{1}{1-S_{DA}^2}\Big\{W_{DA} - \frac{1}{2}(\varepsilon_D + \varepsilon_A)S_{DA}\Big\} \tag{5.7}$$

where

$$S_{DA} = \frac{1}{N}\sum_{\substack{i,j\in D\\ k,l\in A}} T_{ij}^D T_{kl}^A S_{ik} S_{jl} \tag{5.8}$$

and N is the number of electrons in the dimer and the intermolecular atomic orbital overlap integral is

$$S_{ik} = \int dr \psi_i^*(r)\psi_k(r) \tag{5.9}$$

where $i \in D, k \in A$. Again this is dependent on the transition density moments which for the S_1 state are almost zero. This time it is also dependent on the overlap of orbitals on opposing molecules and so dramatically decreases with distance. For this reason, as with the exchange interaction, the neglect of the overlap is as justified for Car as it is for Chls.

5.0.2 Coulombic coupling

In this thesis I define energy transfer as a function of coupling and spectral overlap. While the spectral overlap poses problems due to determining the line-shape and vertical excitation energy (discussed in chapter 4), calculations of coupling pose their own problems. We have shown in section 3.1.2 how we do this, even with the ~ 0 μ dipole of the Car S_1. The couplings therefore result from an interaction between the two transition density clouds. Local areas of negative and positive charge interact with molecules which are close enough for these areas to resist the effects of averaging due to distance (figure 5.4). The way in which coupling is varied can be split into three distinct but connected concepts: interpigment distance, spatial relationship between the two pigments and any distortions of the molecule. As discussed in section 1.5.4, the Cars are likely to play an essential role in the quenching of excess Chl singlet excited energy. There is also a proposed conformational change which switches plant light harvesting proteins between a light harvesting and a dissipative state. It is likely that this conformation change affects one or more of the three factors responsible for coupling. We therefore decided to investigate these three factors and their relationship to S_1-Q_y coupling to elucidate the switch mechanism at the trap.

The conformational change of the protein is not universally accepted. Barros and co-workers[188] contend that the quenching mechanism arises as a result of the interactions between the trimer units of the proteins rather than an internal change. However, the evidence for an internal change is overwhelming. Ilioaia *et al.*[189] observed quenching in spatially isolated trimers, suspended in acrylamide gel. In this case there can be no inter-trimer interactions and the only thing approaching this would be compression of the units caused by pressure from the gel. This may mimic the effect of aggregation. Further evidence of LHCII trimers exhibiting quenching came with the single-molecule spectroscopy of Krüger *et al.*[190]. They showed that isolated LHCII trimers went through a 'blinking' between the states, where the protein would exist in a bright or dark state for a period of time and go through almost instantaneous switches between the two. We shall assume that these metastable ($\tau \sim 1 - 10$ s) states represent the light harvesting and NPQ states respectively. This blinking was sensitive to environmental factors such as pH. In this case a lower pH would cause the protein to spend more time in the dissipative state while

still occasionally switching back and forth.

Explicit evidence for the conformational change and its connection with qE can also be found. Resonance Raman shows a distinct conformational change in both the Neo and Lut620 in LHCII when it undergoes a state switch. Names of the pigments used are from the crystal structure by Liu *et al.*[42] for LHCII and Yan *et al.*[191] for CP29. Time-resolved laser flash photolysis, flash-induced triplet minus singlet and absorbance detected magnetic resonance have all shown that the switch to the quenched state is associated with changes to the electronic interactions between Chl and Car pigments. Finally, Pandit *et al.*[192] used NMR to show that aggregation induced quenching in *Clamydomonas* involved chemical shifts for key carbons of the Chl macrocycle. They suggest that they originate from differences in the Chl-Car interactions.

5.1 Distance

When calculating the coupling using the TDC method, the point charges assigned to each cube on one molecule, interact with each point charge on the other pigment. This interaction is scaled by distance and so it stands to reason that interpigment distance should be a significant factor in the coupling. However, this is reduced by the range of possible motion for the pigments within the protein. The pigments in light harvesting proteins of plants are naturally surrounded by other pigments and the protein. The distance is consistent with van der Waals radii ($1 - 2$ Å as measured from the crystal structure[42]) and so there is little room for pigment movement. We will therefore examine if the coupling between S_1 and Q_y can be significantly affected given a realistic range of interpigment distances.

For this investigation I chose the interactions between the two Luts and their nearest neighbour Chls. This constituted the Lut620-Chl612 and Lut621-Chl603 pairs with the S_1-Q_y as the focus. They were originally chosen as I wanted to compare these two interactions as some mechanisms for NPQ propose them as significantly different with more energy transfer between the Lut620-Chl612 pair. This will be expanded upon in section 6.3. However, I also took the opportunity to investigate if movements within the pigment pocket could affect this. They provide a useful pair of example interactions as they are central to most proposed Car mediated quenching mechanisms.

In order to calculate the couplings between these pairs of pigments we needed starting structures. These were obtained from the crystal structure by Liu *et al.*[42]. For this investigation the pigments were then optimised using a 'cage' of the surrounding protein and pigment fragments (figure5.1). It is essential to optimise the crystal structures as, while they provide a useful starting point, the probabilistic nature of the atom coordinate assignments in crystal structure analysis means that important quantum mechanical parameters such as bond length and angle have significant inaccuracies. These are not relevant in observations of the general shape of the pigments but have important consequences for the ground and excited state wavefunctions. For a simple investigation of the effects of distance on coupling, vacuum optimised structures would be sufficient but my work also included a section on the different distortions between the two molecules. The cage was therefore used to preserve some of the individual distortion, unique to each pigment. As this is not relevant to the discussion on inter-pigment distance, I will discuss the cage process in detail in section 5.2. Pigments where optimised with DFT using a B3LYP functional and 6-31G* basis set while the heavy atoms of the 'cage' are fixed in position. The excited states were calculated using a semi-empirical approach to capture the electron correlation of the S_1 state and CAS-CI was used to give an accurate representation of the states. The work of Kusumoto[151] and Macernis[152] provide some benchmarking for the MNDO method and showed that it is of comparable accuracy to much more expensive methods such as symmetry-adapted cluster configuration interaction (SAC-CI) or CASSCF. It correctly identifies the important states with appropriate symmetry and single/double electron character. AM1 is a very similar mechanism and in our own comparison of the methods, AM1 gave the closest energy and dipole to experimental values. The active space was chosen at 6 orbitals as any increases provided minimal improvements in accuracy but considerably longer computation times. This is corroborated by the work of Macernis who report no improvement when and active space of 8 orbitals is used. The first description (equation 4.1) of the Car DOS was used for this study as it was conducted before we developed the second (equation 4.2). While this is a more primitive description, the data still represents qualitatively accurate data.

For each of the pairs the inter-pigment distance was varied by calculating the closest approach vector between the macrocycle of the Chl and conjugated backbone of the Car. The vector was then increased from the staring distance by units of 0.2 Å up to a maximum of 2.0 Å. This

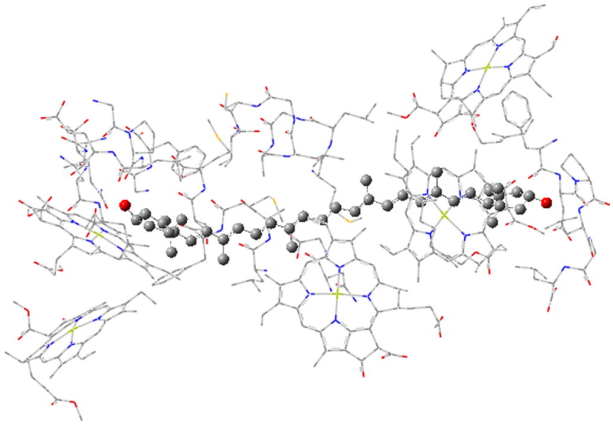

Figure 5.1: The cage optimisation file as displayed in Gaussview. The molecule fragments represented by lines make up the low level calculations while the central pigment, represented by balls is the high level.

maximum is likely much larger than the space in the pigment pocket would allow. The nearest neighbour protein sections are less than this but with 2 Å we have taken extreme movements of the protein into consideration. Shorter inter-pigment distances than the starting position were also not included as we wanted to investigate ways in which coupling could be reduced which would not happen at shorter distances.

We can see from figure 5.2 that the pairs of pigments have considerably different couplings. While this will be discussed in the next section we also see that in both cases the coupling reduces slowly with increased inter-pigment distance. In both of these cases, we see the expected reduction in coupling but we can also see that a large increase in the inter-pigment distance is needed to equate to the difference between the pairs. We can therefore conclude that larger changes in inter-pigment distances than are possible, are needed to have any significance on the function of the energy transfer pathways.

5.2 Distortions to the Car conjugated chain

The question of how distortions of the Car affect the coupling between the S_1 and Q_y state is much less trivial to investigate. We take the vacuum optimised 'planar' structure as our starting point. Under no restrictions from nearby pigments or protein the Car is free to assume its lowest energy conformation with any deviations from the true equilibrium point, arising from inaccuracies in

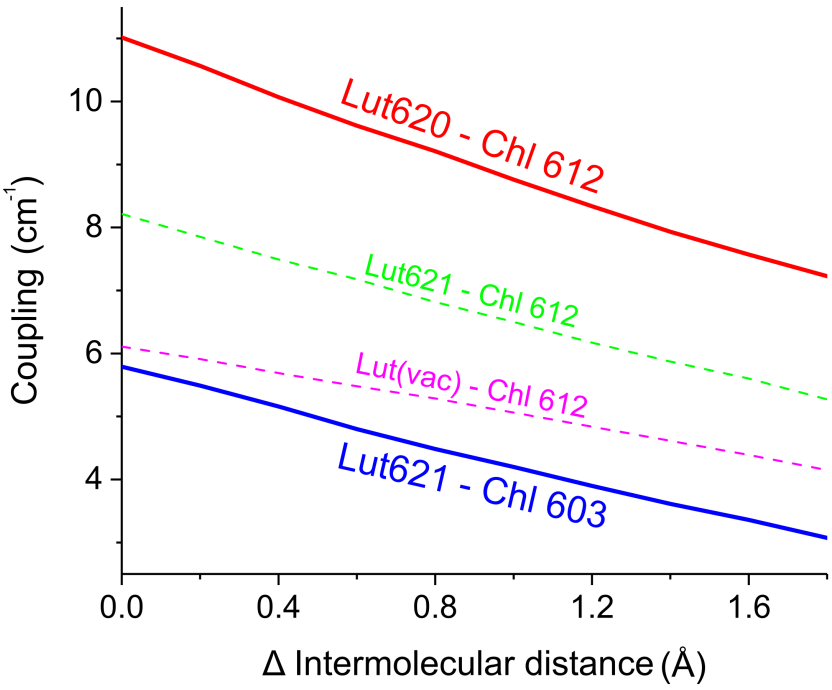

Figure 5.2: Couplings calculated when extending the distance between four Car-Chl pairs. The 0 mark represents the pairing as it is found in the crystal: the red and blue bold lines give a comparison of the L1 and L2 sites, or as it would be found with certain Cars superimposed into the position of another: the green and magenta dashed lines show the differences due to Car distortions. In the red and blue cases, the natural position of the Lut-Chl pair was taken from the crystal structure[42]. In the case of the magenta and green lines, these unnatural pairings were made by superimposing one Lut form on-top of another ensuring that there was a minimum difference in position of the conjugated chain carbons.

the method and basis set, being minimal. From this point the nuclear coordinates could distort in any direction due to external forces as long as it is thermodynamically viable. As they distort they will affect each other and so we are left with a multitude of different interconnected distortions which may affect the S_1 coupling in a variety of ways: they can break the C_{2h} symmetry, they can break the alternacy symmetry responsible for the two-electron excitation and they may affect the shape and dispersion of the TDC cloud.

One way to investigate this is to take the vibrational modes of the molecule as physically viable distortions and investigate how they affect the CI composition. This is beyond the scope of this thesis and may be something to include in further work. I will briefly discuss my own

expectations of such an analysis. It is often claimed that distortions which bend the molecule in any way will break the centre of inversion, thus inducing an allowed S_1 state. As we have previously discussed, this would do little to make the state transition more allowed and this is evident from the structure of many Cars. The geometry of many Cars already has functional groups which considerably break the centre of inversion and yet no S_1 signal is observed. An example of this is Neo which has a *cis* bond on one end of the conjugated chain, disrupting the centre of inversion. However, the S_1 state of Neo is still never directly observed.

In order to make the S_1 state allowed, the one-electron character should be increased. The two-electron character comes from the alternacy symmetry described in section 4.3.1. Therefore breaking this would increase the one-electron character and potentially make the S_1 state more allowed. If we look at the vibrational modes, the most easily accessible, low energy modes describe simple wagging or bending of the whole molecule. While these distortions are likely to be populated, they do little to disrupt the alternacy symmetry. The higher energy C-C (1156 cm^{-1}) and C=C (1522 cm^{-1}) stretching modes[182] are much more likely to do this but are not as highly populated at room temperature. The molecule is therefore quite resilient to breaking of the alternacy symmetry and so the transition from the ground state to S_1 is consistently not allowed.

5.2.1 Lut620 and Lut621

Within this investigation, I limited my research to investigating the potential size of the effect of realistic distortions on the S_1-Q_y coupling. Ruban *et al.*[112] predicted a significant increase in the amount of energy transferred to Lut620 compared to Lut621. This was partly expected to be caused by the higher chance of an excitation being localised on the Chls neighbouring Lut620, due to their lower Q_y energy. However, the Chls near Lut621 are not much higher (~ 60 cm^{-1}) and we would expect significant transfer as well. I wanted to investigate if this discrepancy could be understood in terms of the different distortions between the two Luts. While I will leave the discussion as to whether there really is a difference in the amount of energy transferred to the two Luts to the next chapter, this work provides a useful look at the effect that distortions can have on the Cars ability to couple to nearby Chls.

The difference in the structure between the two Luts is highlighted by the work of Chang and co-workers[191]. They use their crystal structure[42] to highlight the different degrees of twisting, claiming that Lut621 is significantly more 'twisted' than Lut620. The pigment is not planar with some harmonic oscillations as it would roughly be in solvent. The protein structure causes pressures on the molecule due to interacting cloud of elctron density. As the two Luts are in different positions within the protein, with a unique environment of amino acids surrounding them, this pressure is different (figure 5.3. They suggest that this difference in the crystal is similar to the thylakoid membrane. The crystal structure has been shown to give a good indication of the quenched LHCII conformation by Raman spectroscopy. The crystal shows the same features involved with Neo as quenched LHCII *in vivo*[193]. This will be further discussed in the next chapter but our purposes here, it is sufficient to know that the crystal structure gives us realistic conformation of the Luts in the quenched state.

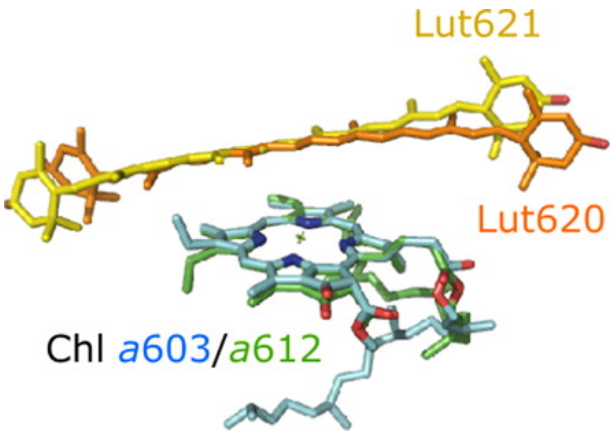

Figure 5.3: A comparison of the L1 and L2 sites in the LHCII crystal[42]. Here the Chls have been superimposed by fitting the 4 Nitrogen atoms of both Chls together.

My method for preserving the distortions found within the protein is to use a 'cage', made from fragments of protein and pigment, surrounding the central molecule. This is created from the crystal structure, with all atoms within 5 Å of the pigment in question included. At this point, any amino acids or pigments which have atoms included are taken in whole and any connected amino acids are also included to make sure that the ends of the fragments are far enough away from the central pigment. This ensures a limited effect from the unnatural ends of the fragments on the optimisation process. Connected amino acids in the case of protein and

portions of pigments are also included so that the electron localisation is properly calculated. The heavy atoms of the cage are frozen and the central pigment is left to optimise with no unphysical restrictions. There is a human judgement part of this process which could affect the pigment optimisation but this is limited as the heavy atoms of the cage are frozen, so the only affect the choice in the fragment cutting are with some small amount of electron density. Finally the hydrogen atoms of the cage are optimised to allow for the formation of potential hydrogen bonds which could affect the distortions of the molecule. This is done in a ONIOM environment so that the central pigment is optimised with a sufficiently high level of theory but the many hydrogens can still be optimised at a lower level without excessively increasing calculation time (figure5.1). The inner level is optimised using DFT and a B3LYP functional and a 6-31G* Pople basis-set. The outer level is optimised using a semi-empirical PM6 method which is used as it is specifically formulated for proteins. The method of using a cage to preserve distortions has been used in many studies before, including one on the Cars of LHCII[194, 195].

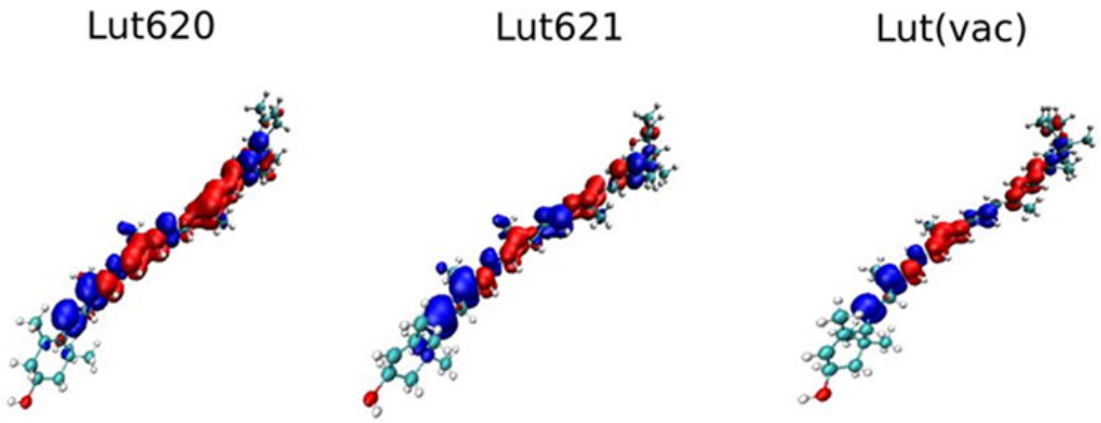

Figure 5.4: The TDC clouds of Lut620, Lut621 and Lut(vac). They have been magnified to most clearly show the shape.

We are left with Lut in three different geometries: the cage Lut620, the cage Lut621 and the vacuum optimised Lut (Lut(vac)). The cage optimised structures differ from the original crystal structure and have tended towards equilibrium. However, they have crucially kept some of the distortions unique to each Lut. Just as Chang and co predicted[191], the different binding pockets have resulted in distinct geometries. In order to show this, we have taken the dihedral angle at each point along the conjugated chain, giving us an indication of the 'twisting' of the

molecule. Figure 5.5 shows us the relatively straight backbone of the vacuum optimised structure with a small deviation as the conjugated chain moves into the ring at one end. By contrast the two Luts show deviation from the planar at many places along the backbone. This is especially true of Lut621 which is in accordance with the predictions of Chang and co-workers who claim that Lut621 is the most twisted. Lut620 seems to show twisting at only one end of the molecule. The result of this difference is difficult to assign to any symmetry breaking elements but can be clearly seen in the TDC clouds (figure 5.4). Lut(vac) seems to have the most constricted TDC cloud with the most distorted, Lut620 having the largest. This is a noticeable change to the TDC cloud but when compared to figure 5.6 we can see that the difference in distortions is negligible.

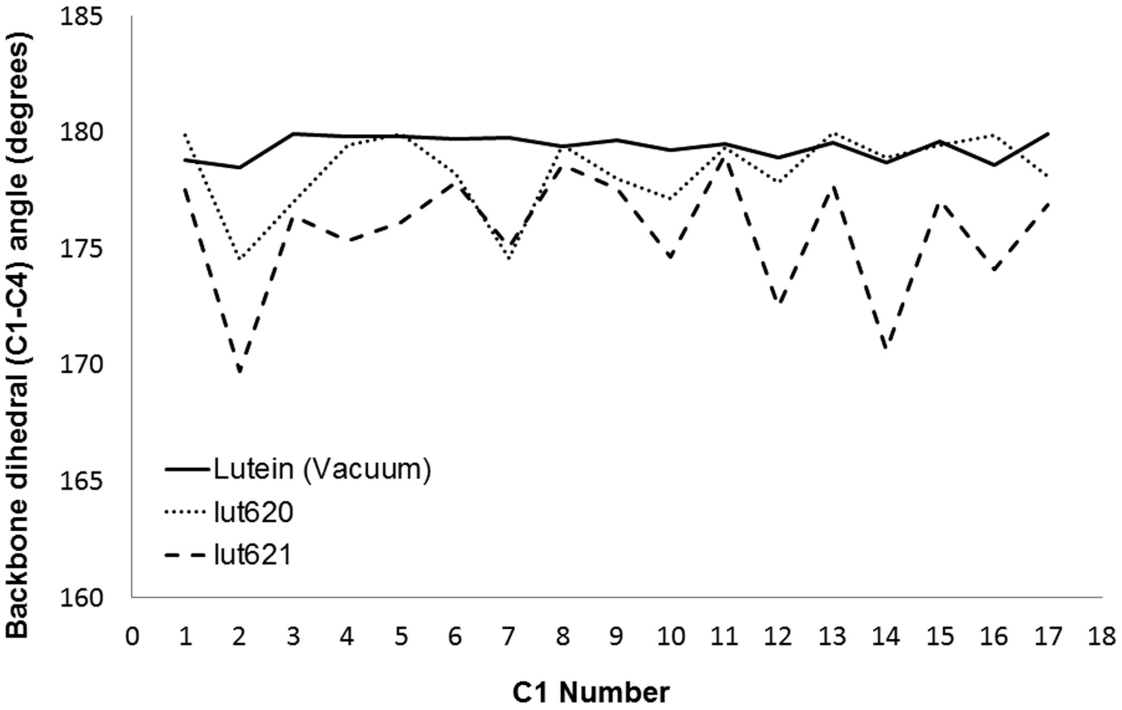

Figure 5.5: The dihedrals along the conjugated chain of all three Luts. 180° represents completely straight and any deviations from that indicates a buckled structure.

In order to compare these three geometries, I have superimposed all three onto the position of Lut620 and calculated the coupling with a vacuum optimised Chl612 (figure 5.6. This is to eliminate as much of the differences in spatial relationship and distance as possible. The result is a considerable difference in coupling between the three: Lut620-Chl612 11.0 cm^{-1}, Lut621-Chl612 8.2 cm^{-1} and Lut(vac)-Chl612 6.1 cm^{-1}. This is a surprising result when looking at how

similar the structures are. The calculated dipole of all three are virtually the same and the CI composition likewise shows little difference in the single electron contribution. However, in the TDC clouds we see the reason for the difference in coupling. Very small geometric differences seem to have had a significant effect on the size and shape of the TDC clouds and this has resulted in the coupling disparity. At the small inter-pigment distances relevant to Chl-Car coupling, the details of the TDC cloud shape is important. The red and blue parts represent the positive and negative parts and they interact with the equally complex TDC cloud of the neighbouring Chl. This is all in agreement with the work of Dreuw, Head-Gordon and co-workers[196, 197] who demonstrate that changes in the $\pi - \pi$ overlap present in Car-Chl interactions are crucial in defining the resonant interaction between the pair. The distortions in the carbons responsible for the $\pi - \pi$ interactions also have a significant effect on the TDC cloud as they are all located in the areas of high TDC density.

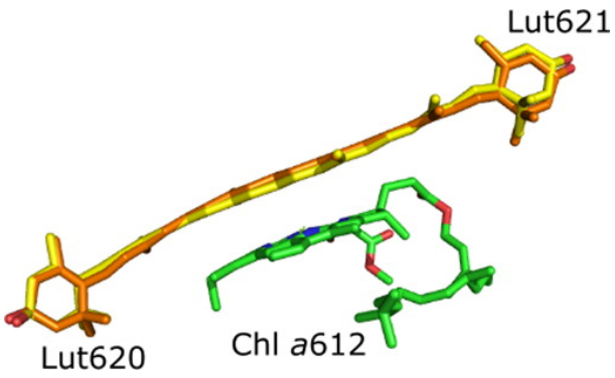

Figure 5.6: Lut620 and Lut621 have been superimposed by fitting the carbons of the conjugated chain together.

Finally if we include the distance relationship between the three pairs, we see a difference with the vacuum optimised pigment pair (figure 5.2). The coupling between Lut(vac) and Chl612 falls of less rapidly with distance than the cage optimised Luts. While this is not significant it hints at the intrinsically connected nature of the three ways in which coupling can change. Here it is possible that the vacuum optimised Car has produced a transition density cloud which is more dispersed than for the cage optimised Cars. The result is that the coupling interaction does not reduce with distance as rapidly.

5.3 Spatial relationship

In order to investigate the different spatial relationship between the two pairs of pigments: Lut620-Chl612 and Lut621-Chl603, we compared the difference in coupling between the two (the L1 and L2 site) with the difference when the two Luts were in a superposition (both in the L1 site). This effectively removes the affect the distortions have on the coupling. As we can see from figure 5.2 the difference in coupling is increased when spatial relationship is taken into consideration. Comparing the two structures, we see that there is very little difference in how the Lut is situated, relative to the Chl. This suggests that angular movements of the Car in relation to the Chl could be as important as distortions in determining the coupling. This is likely to be because it changes the way the positive and negative portions of the TDC clouds interact with each other. However, this preliminary study does not give a very good indication of the specifics of how spatial relationship affects coupling as this was not the original intention of the study.

We found that the particular pairing of Car and Chl found at the two Lut sites in LHCII can be found through the LHC structures. To investigate and significance of this, my collaborator set up a project to artificially manipulate the spatial relationship and see how it affects the S_1, as well as S_2, coupling[198]. The positioning of the Chls in light-harvesting complexes are very specific, with the aim of creating favourable excitonic energy transfer conditions. It is highly likely that the same holds true for the Cars and we hoped that this investigation would explain the positioning of the Cars in relation to their nearest neighbour Chl. While the following research was not lead by myself, I was involved with much of the work and discussions involved and so it shall be presented here.

We looked at all Car to closest-neighbour-Chl pairings in the major and minor light harvesting systems of PSII and the antenna proteins of PSI. There is strong structural homology between many of these, producing an L1 and L2 site (figure 5.7a-d). These sites are centrally located positions for Cars, occupied by Lut in most proteins including LHCII, but with some variation such as the Vio at the L2 site of CP29. In all pairings we superimposed the four nitrogen atoms of the Chl so as to achieve maximum spatial coincidence of the Chls. Interestingly this also corresponded to considerable coincidence of the Cars, with all being found on the same side of the Chl and with the same angle and distance (figure 5.7e-f). In order to investigate

spatial relationship without the effects of distortions, we optimised all pigments in a vacuum so that they came as close as possible to their lowest energy conformation. These structures were then superimposed back onto their unoptimised position. The excited states and couplings were calculated in the same way as the above sections.

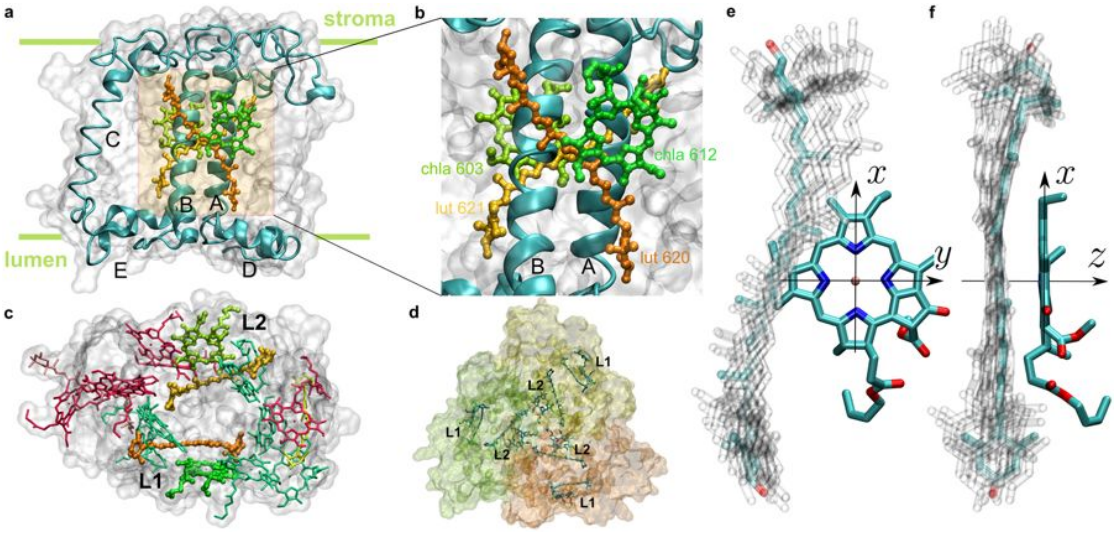

Figure 5.7: a-d. the positions of the key Cars in the L1 and L2 sites in Lhcb1 (a-c) and LHCII (d). e-f. All Car-nearest neighbour Chl pairs in the L1 and L2 sites have been superimposed onto each other via the Chl nitrogens, with the x, y, z axis shown.

We noticed that across the various pairs of pigments, the largest degree of movement was a rotation around the z-axis of the Chl. While the movements were still minimal due to the density of the protein, we chose this as the first method for changing the spatial relationship. We kept the L1 and L2 site pairs separate due to the slight differences in the pigment pockets and rotated the Chl around the z-axis (effectively moving the Car around the circumference of the Chl macrocycle). The couplings can be seen in figure 5.8 with the sign of the couplings being a result of the direction of the dipole and physically insignificant for Förster transfer. This showed significant change as the Chl is rotated with the area around 0 (the original position of the pairs) being particularly low. Other methods of altering the spatial relationship were tested but we did not find significant changes to the coupling and so they were not reported.

Much of this work was set in the context of NPQ in light harvesting systems; we wanted to know how pigments such as Cars, which naturally dissipate energy, could be present in such

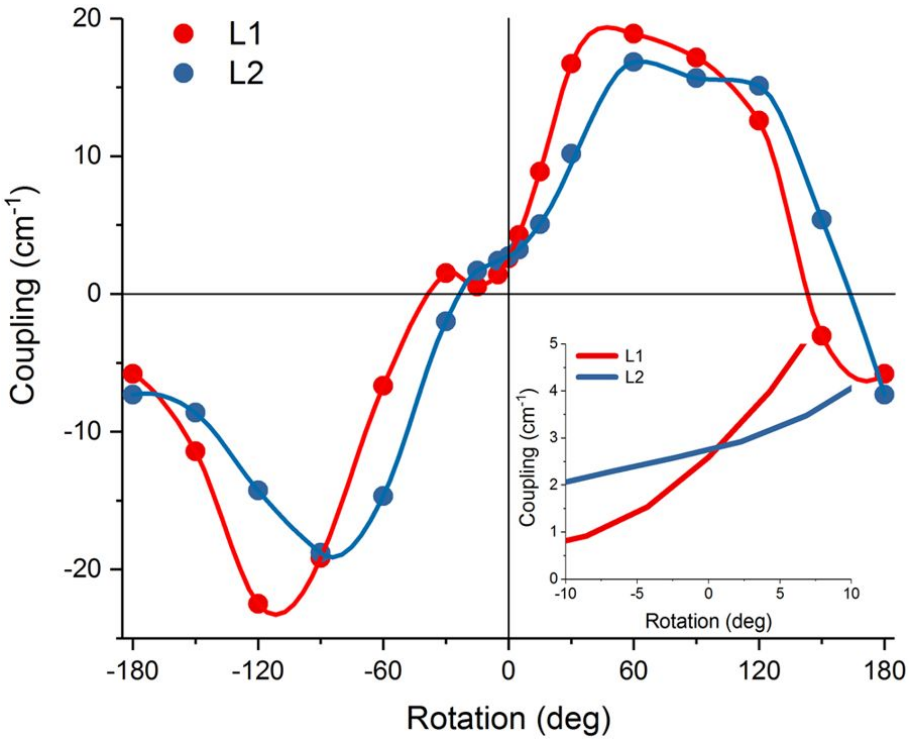

Figure 5.8: The coupling is calculated while the Chl is rotated around the z-axis. The inset graph shows the fine detail around the section which the *in vivo* is most likely to be found.

large numbers in the densely packed light-harvesting complexes without disrupting the light harvesting function. The Car needs to function as a light harvester, quench any triplet Chl states and potentially even quench any excess singlet Chl energy. The ability to function in these three roles may help to explain why the position of the Car in relation to the Chl is held so consistently. This mutual orientation represents the lowest possible resonant interaction between the two lowest singlet states, while still maintaining the π overlap necessary for triplet quenching. This helps to explain how the light-harvesting function of the proteins is not overly disrupted by the presence of Cars. As well as this, we see how sensitive the coupling is to certain changes in their orientation. This could explain how the Car is able to situationally quench singlet Chl energy. This will be discussed further in the next chapter on NPQ in LHCII and CP29.

Chapter 6

NPQ in the major and minor antenna

6.1 Theories of non-photochemical quenching

We have already discussed many aspects of the mechanism for the fast acting photo-protection: NPQ. Much of this is generally agreed upon with strong evidence of the involvement of proton gradient, the xanthophyll cycle and PsbS having an influence over aggregation and a conformational change to LHCII. However, beyond this point there is much dispute, with the site of the quencher being particularly debated. We will therefore detail some of the proposed theories before discussing our own thoughts on this complex process.

There are three ways in which the Chl singlet excited state energy can be quenched within the time-frame of NPQ. The energy can fluoresce, undergo internal-conversion to the ground state or transfer energy to another pigment. Chl in ethanol has a lifetime of ~ 5 ns with that being reduced to ~ 4 ns in LHCII. In the membrane the lifetime is further reduced to ~ 2 ns when the reaction centres are closed. The reaction centres are purposefully closed for these measurements as they form a pseudo quenching mechanism in that the Chl fluorescence is reduced by the processes of photosynthesis rather than NPQ. This 2 ns lifetime was originally attributed to quenching due to the charge separation at the RC followed by charge recombination. However,

Belgio *et al.*[62] showed that it was preserved in lincomycin treated membranes which contain no RCs. The new lifetime of $\sim$ 2 ns marks a drastic reduction in lifetime so that even in the light-harvesting state, there is considerable quenching in the membrane. At the concentrations found in the membrane ($\sim$ 1M), Chl would actually be expected to have an even shorter lifetime with concentration quenching effects occurring in Chl solution at $\sim$ 0.6M[199]. It is therefore remarkable that the system can light harvest at all. In addition, the Chl pigment are now in proximity to the Cars which have a short lifetime singlet state at a similar energy to the Chl *a* Q_y. The primary goal of the various NPQ mechanisms proposed is to explain the further reduction of the lifetime to $\sim 200 - 400$ ps in the thylakoid membrane, where all components are present.

6.1.1 Quenching site

The discovery of the effect of the xanthophyll cycle on NPQ prompted the proposal of the molecular gear-shift model. As Zea increased, so did quenching, fostering the idea of Zea as a site for quenching. The gear-shift model was built around the lower S_1 energy of Zea compared to Vio. It suggested that energy in the Q_y pool would not transfer to the high energy Vio which was proposed to be above the Chl *a* Q_y level. As Zea is formed, the new S_1 energy of Zea was proposed to be below the Q_y level due to its extended conjugation chain. The xanthophyll cycle therefore acts as a gearshift, with Vio acting as a light-harvester, transferring energy into the Chl pool, and the reverse being true for Zea. The system could then convert between the two as they are needed. However, it was later shown using TA and fluorescence spectroscopy that the S_1 energy of both Cars lies below that of the Chl Q_y[200, 201, 202], both in organic solvent and in LHCII itself. This means the Gearshift model is unlikely to work although there is some uncertainty in the S_1 measurements.

The first direct involvement of Carotenoids was measure by Flemming and co-workers who used transient absorption to show an instantaneous population of a Car S_1 state upon excitation of Chls[106] in the Thylakoid membrane. This was attributed to Zea, indicating rapid transfer from Chl to Zea followed by quenching. The instantaneous rise in S_1 has since been observed in LHCII aggregates devoid of Zea[107].In such a situation the two pigments would form one

quantum body with a pair of split states originating from the Q_y and S_1, explaining the instantaneous rise. In principle the lower energy state could act as a quencher if it possessed enough S_1 character to efficiently dissipate[203, 204].

A natural product of excitonic interactions is the presence of CT states. This is the localisation of the electron and the hole which make up the exciton, on opposing molecules. In a homodimer or any pair of pigments where the lowest singlet states are equivalent in energy, the CT states lie above the excitonic states and are relatively inaccessible. However, as the energy gap between the original states increases, the CT state lowers in energy and can fall below the excitonic states. At this point they can be populated and, under certain conditions, the excitonic interaction can fall apart, resulting in an anion and cation. This naturally then recombines through charge recombination and the energy is dissipated as heat. If the conditions for populated CT states between Car and Chl are met, then there must be a transient population of cations. These exhibit a distinct spectroscopic signature in the near infra-red zone ($\sim 900 - 1000$ nm)[108]. Flemming and co-workers found the presence of a cation signal with a rise time of ~ 11 ps in the thylakoids[109] using TA spectroscopy and attributed it to Zea. The size of this signal was found to scale with quenching[110]. This cation signal was also found in the PSII minor anetnna complex CP29 and was found to be assciated with the Vio a the L2 site[110, 111]. This signal was found to be dependent on the presence of two neighbouring Chls and so it was proposed that the CT states from by delocalisation of an electron across these two Chls. Wachtveitl and co-workers used two-photon ionization spectroscopy to create and observe a Zea cation in LHCII trimers[205, 206]. In addition, signals relating to Lut cations have been observed in the minor antenna complexes[207, 208]. There is little direct evidence of a link between these cations (especially Zea) and quenching[111, 205, 206] although these mesaurements are taken *in vitro* and there could be some change *in vivo* via some interaction with change in pH or PsbS as proposed by Flemming *et. al.*[111].

Excitonic interactions are not the only way for energy to transfer from Chl to Car. Transient absorption studies by Ruban *et al.*[112] shows a much slower rise of a Car S_1 signal, peaking at $\sim 20 - 40$ ps. This indicates slow incoherent transfer. They propose this transfer to be to the Lut at the L1 position in LHCII due to the presence of the $S_0 \rightarrow S_2$ bleach in the TA kinetics. The proposed mechanism for NPQ in this case is that a conformational change to the

protein alters the interaction between Chl and Lut to increase incoherent energy transfer. They propose that aggregation is likely responsible for this conformational change. It is also possible that the protonation of certain amino acid residues on the lumenal side of the protein aids. As we have previously discussed, a variety of changes to the pigments themselves, or their mutual orientation could in principle induce a significant increase in incoherent transfer. Ruban *et al.* propose that conformational change after protonation is identifiable by a specific twisting in the Neo. They then go on to suggest that this is indicative of a change which increases energy transfer to Lut620 in the L1 site from the neighbouring Chls. This Lut is next to the lowest energy Chls, often termed the terminal emitter, and hence they suggest Lut620 as being the primary site for quenching in NPQ.

While Cars provide a natural candidate for the quenching site due to their short S_1 lifetime, their involvement is still debated. Holzworth and co-workers contend that their is no direct evidence for the involvement of Cars in quenching and propose a Chl only model to explain an increase of energy dissipation[114]. They suggest that the red emitting states, formed during NPQ *in vivo*, indicate the presence of Chl cations formed from Chl-Chl CT states[105]. This would not normally not be possible for homodimers as they should have CT states that are thermodynamically unavailable. However, the anisotropic environment which creates the energetic funnel in the antenna, causes significant differences in energy between the Chls. This could lower the CT states in energy enough to be populated. Chl-Chl CT states are known to have an increased rate of internal conversion to the ground state enabling them to act as the quencher in the model proposed by Holzworth and co-workers.

Here it should be noted that all this spectroscopic data including ultrafast TA and fluorescence is conducted *in vitro* on potentially very complex pigment protein systems. This causes difficulties due to strong scattering and many overlapping spectral signals. This can be partially overcome by increasing the laser strength used but this in turn causes non-linear artifacts such as transient quenchers and singlet-singlet annihilation[209]. Many of the studies mentioned in this discussion of NPQ mechanisms have not eliminated singlet-singlet annihilation and van Oort *et. al.*[210] have shown that this can lead to misleading spectra. They show that these annihilation effects can create many of the states which have been used to explain quenching, in particular the interaction between Chl and Car at the L1 position. This may explain why there are so many

different interpretations of such similar spectroscopic data.

6.1.2 Minor antenna

Modulating ΔpH with artificial proton shuttles has given us a clearer understanding of the effect of a build up of protons in the thylakoid membrane. It gives us vital sensitivities of the response at various parts of the NPQ process to lumen acidification. As we discussed in section 1.5, the pKa of LHCII is around ~ 4.1 which is below physiological conditions. However, this is 1-2 units of pH higher in the presence of Zea for the monomeric antenna protein CP26. It may then be possible, as the monomeric minor antenna proteins need a smaller ΔpH to become protonated, they may be the primary site for quenching which spreads to LHCII. The minor antenna being a key site for quenching has been argued by the groups of Flemming and Bassi[111, 110].

Studies of DCCD binding has shown that the minor antenna readily accepts protons and exhibits high levels of quenching. Ahn *et al.*[111] have observed quenching in isolated CP29 clusters, proposing a CT transfer state between Chls and the centrally bound Zea at the L2 site. Another proposed method uses the structural homology between LHCII and CP29[48], suggesting that Lut620 forms a cluster with two nearby low energy Chls. Here excitonic interactions lead to dissipation of the energy by Lut, mirroring proposals for quenching in LHCII. Knock out mutants, which selectively remove individual minor antenna or the double knock out which removes CP26/CP29, have shown only limited reduction in NPQ[76]. From these studies, Miloslavina *et al.*[211] propose a mechanism whereby two independent quenching processes occur: one in the minor antenna CP29 and one in detached LHCII units. However, Holleboom *et al.*[212] show that quenching in the minor antenna is aggregation controlled and follows the same processes as LHCII. They believe that quenching in both the minor and major antenna is a result of excitonic Chl-Car interactions. Most recently, Dall'Osto *et al.*[213] have created a knock-out mutant which possesses no minor antenna at all. They also suggest that NPQ has a dual phase with one mechanism in the minor and another in the major. In their mechanism the minor antenna is able to form a particularly fast acting quenching pathway through CT states between the Lut and Zea in the L1 and L2 sites with their nearest neighbour Chls. Then in the major antenna, a slower form of NPQ can form which is dependent on Zea de-epoxidation.

6.1.3 Aggregation and conformation

While the main point of contention between the various mechanisms for NPQ is the site, the presence of aggregation is universally agreed upon. However, the nature of this aggregation is still being investigated. Spectroscopic *in vivo* evidence shows that aggregation associated with NPQ also consists of a separation of LHCII from PSII[105, 214]. Further structural evidence shows that PsbS is linked with disassociating a portion of the PSII supercomplex containing LHCII, CP24 and CP29[80]. It also shows that the distance between PSII core complexes becomes shorter. Freeze fracture experiments[81] support this and importantly highlights a clustering of LHCII units. Figure 6.1 shows a schematic of this process, with PSII core units coming together as the LHCII units which once separated them, aggregate into clusters. The initial assumption here is that the LHCII units disconnect from the RCs when in high light, reducing the size of the antenna. However, recent data has shown that the antenna is still energetically connected[215]. The model where the LHCII units stay connected to the core complexes is in line with the previously established relationship between NPQ and yield of PSII. Belgio *et al.*[215] shows that the actual size of the antenna for the RC goes up during aggregation and they propose a model of economic photoprotection to explain this. In their model, there are a large number of 'shallow' traps. These shallow traps are not particularly efficient quenchers and will only quench a significant portion of energy if the energy remains in the system for an extended period of time. This means that the quenching process only occurs when the RC is closed and will be outcompeted by the RC when it is open. In this way, even in the quenched state, the large antenna can avoid any unnecessary loss of energy while the RC is available for photosynthesis. Finally it is not clear if the aggregation process is the primary cause of NPQ or if it is simply a natural thermodynamic consequence of the inner-protein conformational changes[216]. A form of quenching has been observed in the highly unnatural system of isolated LHCII units[116]. In either case, pressure was exerted on the protein either through high hydrostatic pressure[217] or simply a removal of detergent[189] when in a gel. The necessity of such an unnatural condition makes it difficult to draw comparisons with the *in vivo* system. However in all cases we can say there is some pressure which could effect a change on the protein structure. This may suggest that the primary purpose of aggregation is to squeeze the LHCII units together. Perhaps in this

state, the interactions between pigments undergo a significant change as they are squeezed into certain positions.

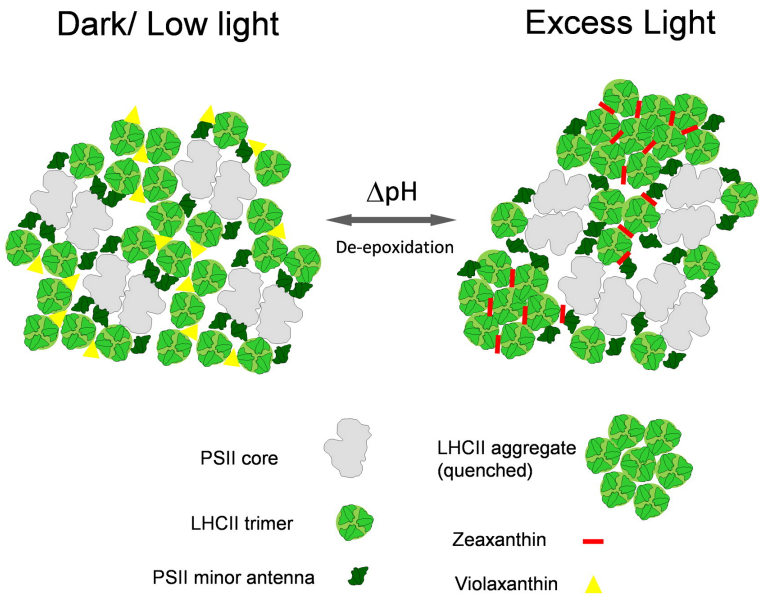

Figure 6.1: Figure taken from Ruban *et al.*[54]. Shows the current understanding of the structural reorganisation which occurs when switching to the NPQ state

Single-molecule fluorescence spectroscopy has been extensively used to show the state of the various proteins in the thylakoid membrane. The LHCII units were found to exist in distinct states rather than a scale of fluorescence emittance[190]. These are characterised as an emissive light harvest state, a dark quenched state and a further red state characterised by a broad peak at ~ 700 nm. The red state is thought to be due to mixed exciton-CT states from STARK[218], and hole burning spectroscopy[219]. The LHCII units were seen to rapidly switch between these states in a process known as 'blinking'. This blinking was found to be modulated by both Zea and protons, with the antenna units spending more time in a particular state based on its conditions. Blinking between states represents local conformational changes which extend beyond typical thermal fluctuations. Valkunas and co-workers[220] have built a set of models to explain the kinetics of the thylakoid. Within their model the light harvesting and photoprotective properties of the membrane are explained by the relative proportions of the LHCII units in the light or dark states. They show that only a small number of LHCII units need to be in a quenched state for the whole membrane to be photo-protective.

Chmeliov *et al.*[220] describe the red state as totally distinct from the quenched state and do not assign it any particular importance in photoprotection of the membrane. In contrast, the SMS work of Krüeger *et al.*[190] observes multiple red states, some of which it links to quenching. They propose that quenching occurs via several distinct pathways with the primary occurring in the dark state through incoherent transfer to Cars. The predominant red state at ~ 700 nm was attributed to a CT state at the L2 site and was found to be unrelated to quenching. However, additional red states at > 710 nm where found to be quenching pathways at the L1 site. They propose that the conformational change of the protein leads to strong coupling between the L1 Lut and the nearby cluster of Chls.

This chapter will detail my own investigations and findings into this hotly debated topic. My model is built with computational studies of LHCII, with a focus on what is necessary for the system to quench. I then move on to compare with CP29 which was chosen as a representative of the minor antenna due to the availability of a high resolution crystal structure.

6.2 Modelling

In order to investigate NPQ, we have built a model of quantum mechanical processes such as energy transfer and dissipation which rely on a set of parameters. Where possible these have been obtained from experiment but many have had to be calculated. The rate of transfer between pigments is dependent on coupling which is calculated using the ground and excited state wavefunctions of the two pigments. In order to calculate these wavefunctions, the nuclear coordinates are essential and so it is essential to have a set of coordinates for all the atoms which make up our system, excluding the bath. Our starting point for this is the crystal structures.

For LHCII we have used the structure by Liu *et al.*[42]. Pascal *et al.* showed that this structure is highly quenched relative to solvated LHCII and possesses many of the same spectral features as the *in vivo* photoprotective state. It is therefore assumed that the crystal structure represents a good approximation of quenched conformation of LHCII. Modelling should therefore provide insight into the quenching processes during NPQ. LHCII is by far the most studied of the plant antenna proteins but in 2011 Pan *et al.*[221] resolved a high resolution crystal of the minor antenna CP29. This enabled us to model CP29 as a representative of the minor antenna

as well as LHCII.

These crystals give a good representation of the bulk structure but for calculations which determine the quantum mechanical processes of NPQ, the fine detail of the pigment coordinates must be quantum mechanically optimised. This is because small deviations in key parameters such as bond length and angle, can have a significant effect on the ground and in particular the sensitive S_1 excited state wavefunctions. We employ a pair of strategies for this. The first is a simple optimisation in vacuum using the DFT functional B3LYP which gives good variational energies much more rapidly than more rigorous *ab initio* methods. The second is to use the same method on the pigment but treat this as the inner layer of an ONIOM calculation. The outer layer is made up of the surrounding pigments and protein fragments with frozen heavy atom coordinates and Hydrogen atoms optimised simply with a semi-empirical PM6 method. This process has been explained in section 5.2 and is used where we wanted to investigate the effect of the pigment distortions. We will call these two methods 'vacuum optimised' and 'cage optimised' respectively.

LHCII has been modelled atomistically by many groups in an attempt to understand the processes within. The excitation transfer and spectral dynamics are dependent on the methods used to describe the system-environment interaction. van Grondelle and co-workers[47, 222] used a modified-Redfield approach and was successful in reproducing steady state and transient absorption spectra although with some fitting procedures. Later Müh *et al.*[223] included a more detailed inclusion of the environment and was able to match the spectra without the need for extensive fitting. These models have been used to describe many of the processes involved in light harvesting with the work of Menucci *et al.*[224] proving particularly interesting. They showed the importance of dynamic pigment-protein interactions in defining the function of the complex though use of MD. However, these models failed to reproduce the fluorescence lifetime measurements of the crystal, in particular the considerable degree of quenching. This was theorised to be due to the absence of the Cars in these models. Duffy *et al.*[179] calculated an interaction between Lut620 and its nearest neighbour Chl, providing a potential source of dissipation which would explain the reduced fluorescence lifetime in the crystal. This was then later used in the first 'all pigment'[180] model of LHCII, giving a heavily quenched lifetime of ~ 100 ps. While this was much lower than experimental values, it enabled them to build evidence

towards the Ruban *et al.*[112] model of quenching.

The Chl dynamics have also been successfully modelled for CP29 by Müh *et al.*[49], again reproducing steady-state and transient absorption spectra. However, the understanding of the processes within this protein has not benefited from an 'all pigment' model in the same way as LHCII. We therefore aim to create an accurate model for both LHCII and CP29, expanding on the one by Chmeliov *et al.*[180]. We investigate many of the phenomena which determine the various models for NPQ in these antenna proteins.

6.2.1 Structures

In figure 6.2 we present the cage optimised structures of the four Cars in LHCII. The optimised structures of the CP29 Cars are compared to these in figure 6.14. The LHCII structures are compared to the crystal structure pigments[42] to show their similarity. There has been some deviation during optimisation with the pigments tending towards the planar but deviations fall well within the resolution limits. The largest differences are some small head rotation, probably due to an underestimate of the conjugation bonding strength in the calculation. However, The cage optimised structures have retained a significant degree of their distortions showing that the process has been reasonably successful. Finally the cage optimised Chls in LHCII, once repositioned into the original position, are effectively the same as the crystal. In our own computational comparison, we found not enough of a distinction between cage and vacuum optimsied Chls to warrant using the demanding cage procedure for CP29. These have therefore all been vacuum optimised.

For our LHCII structures we used bond-length alternation (BLA) to compare structures. Bond length alternation is a parameter which gives us an indication of how well the alternacy symmetry is observed. As this symmetry is dependent on two inter-connecting sublattices, the consistency of this along the conjugated chain is important in determining the excited state properties[225, 224]. BLA is defined as

$$\delta_n = (-1)^n\big(\bar{n} - (\bar{n}+1)\big) \tag{6.1}$$

where n is the bond number and $\bar{n}$ is the bond length. Plotting this (figure 6.3) we can see

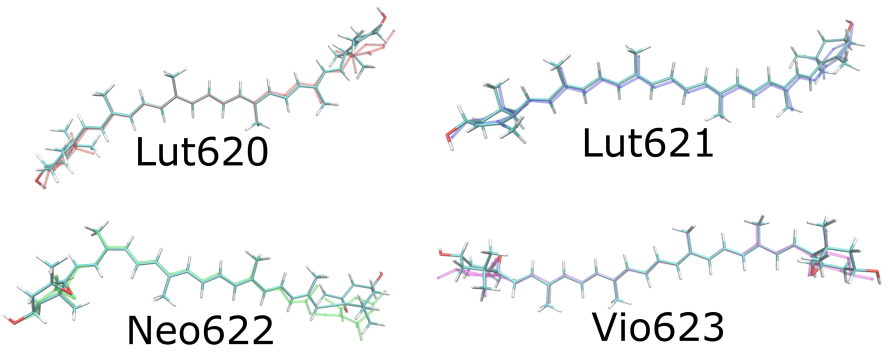

Figure 6.2: A comparison of the LHCII cage optimised Car structures, displayed in bold, with the original crystal structure, displayed as semi transparent behind.

that the cage optimisation was only partially successful. We have compared our cage method with the dihedral freezing technique used in previous models for Lut620. Duffy and co-workers optimised pigments in vacuum but with all dihedrals frozen in place. I argue that this causes artificial errors in the bond lengths and angles. These are then compared to the vacuum optimised structure which should give a reasonable BLA pattern. The BLA on the majority of backbone for the cage structures seems to be in good agreement with the vacuum but on one end it deviates. This is where the conjugated backbone moves into the head group. The optimisation step underestimates the effect of the protein relative to how energetically favourable a planar conjugated chain is. The dihedral issue is not observed in the dihedral freezing method as this forces the head turn. This loss of shape is problematic but for the majority of the backbone, the restriction free optimisation gives a more accurate shape. Additionally I expect that it would create more natural bond lengths and angles, even if they do not match the pattern of the crystal entirely.

6.2.2 Excited states

Table 6.1 shows the results of the excited state calculations on the LHCII pigments. AM1-MECI crucially gives a correct description of the Car S_1 states. This is manifest firstly in the almost zero dipole moment but also by being predominantly made up of a double HOMO→LUMO CI configuration. The excitation energies for all pigments are overestimated, compared to experi-

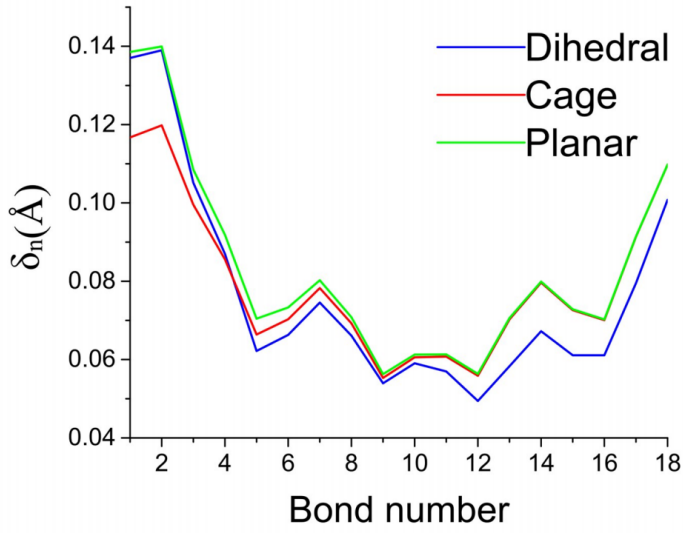

Figure 6.3: The bond length alternation plot of Lut620 optimised in three different ways. BLA is defined as $\delta_n = (-1)^n\big(\bar{n} - (\bar{n}+1)\big)$

mentally reported ranges. If we compare our Car S_1 energies to those obtained by Andreussi *et al.*[226] with their expensive MRCI/DFT approach, we see that they also overestimate energies but by not as much as our own (Lut - 17180 cm^{-1}, Vio - 17583 cm^{-1}, Neo - 18228 cm^{-1}). Importantly, however, our energies are overestimated by a single scaling factor of ~ 1.1 (Neo - ~ 1.14, Vio - ~ 1.11, Lut - ~ 1.11). Because of this we contend that it is reasonable to use our own calculated energies for the cage structures and scale them all in the same way. The energies and dipoles of the Chls are also overestimated but as the experimental values are very well known, we can simply scale our results to them. This is done by taking an average of our Chl values, working out the scaling factor to match it to experiment and applying it to each individual pigment. This retains the differences between them, caused by the cage optimisation process.

For CP29, all Chls were simply given the experimental energies and dipole moments as they were all vacuum optimised. Our calculated values for the Cars are very similar to those in LHCII, with only minor differences caused by the slightly different environments. The most important factor of the double excitation is preserved. We compare our results to the environmentally inclusive, spectrally fit Müh *et al.*[49] and find a similar ~ 1.11 scaling factor.

	Energy (cm^{-1})		Dipole (D)	
	AM1-CAS-CI	Exp.	AM1-CAS-CI	Exp.
Chl *a*	16695	14884[a]	7.55	4.58[b]
Chl *b*	17585	15362[a]	3.63	3.83[b]
Lut620	19538	14050[c] - 15300[d]	0.17	≈ 0
Lut621	19748	14050 - 15300	0.30	≈ 0
Vio622	20115	13700[c] - 15580[e]	0.18	≈ 0
Neo623	20250	>15000[f]	0.15	≈ 0

Table 6.1: LHCII parameters: **a**.[223], **b**.[227], **c**. $S_1 \rightarrow S_2$ absorption[228], **d**. 2-photon absorption[176], **e**. Fluorescence[229], **f**.[161]

	Energy (cm^{-1})		Dipole (D)	
	AM1-CAS-CI	Exp.	AM1-CAS-CI	Exp.
Chl *a*	17221	14884[a]	6.97	4.58[b]
Chl *b*	17497	15362[a]	4.93	3.83[b]
Lut	20313	14050[c] - 15300[d]	0.40	≈ 0
Vio	20420	13700[c] - 15580[e]	0.13	≈ 0
Neo	20557	>15000[f]	0.22	≈ 0

Table 6.2: CP29 Parameters: **a**.[223], **b**.[227], **c**. $S_1 \rightarrow S_2$ absorption[228], **d**. 2-photon absorption[176], **e**. Fluorescence[229], **f**.[161]

6.2.3 Couplings

Couplings were calculating from these excited states using the TDC method. We first present (figure 6.4) our LHCII couplings (lower left half) and compare them to those calculated by the Chmeliov *et al.*[180] (upper right half) study which used vacuum optimised Chls and Cars optimised with frozen dihedrals. The energies are presented along the diagonal to complete the Hamiltonian. The Chl couplings are taken from Müh *et al.*[223]. For the Car energies we used our own calculated as a starting point. These were then scaled down by a single scaling factor to ensure the Lut was at the experimental energy[176], maintaining the ratio between Car S_1 energies. While the energies have been overestimated, they contain some of the information from the distortions caused by the cage optimsation and by keeping the same ratio we preserve this. The Lut energy of 15300 cm^{-1}[176] was chosen as this was the spectra we derived our spectral density from. However, their energy was simply the middle point of a single broad peak while our own description takes into consideration the vibronic splitting (equation 4.2). The 0-0 peak can be taken as 1339 cm^{-1} below the centre of the single peak, resulting in a vertical excitation energy of 13963 cm^{-1} for Lut.

The cage optimisation has had very little effect on the Chl couplings with all important Chl-Chl interactions effectively the same as previous studies[223, 180]. The Chl-Car also broadly match those of the Chmeliov study[180] with the two key Lut-Chl interactions remaining strong. Lut620 is only significantly coupled to Chl $a612$ (6 cm^{-1}) and this is mirrored by the Lut621-Chl $a603$ interaction (7 cm^{-1}). The peripheral Vio is only weakly-coupled to Chl $a614$ (5 cm^{-1}). These are all around $\sim 40-50\%$ lower than the Chmeliov study. This is probably due to the cage structures tending towards the vacuum, resulting in lower dipoles. Unexpectedly we also report a significant increase in the Neo to Chl $a604$, Chl$b606$ and Chl $b608$ couplings (6, 7 and 9 cm^{-1} respectively). This must be due to complex interactions in the TDC fields. My work (chapter 5) has shown that only small deviations in structure are necessary for this.

Pigments	Chlb601	Chla602	Chlab03	Chla604	Chlb605	Chlb606	Chlb607	Chlb608	Chlb609	Chla610	Chla611	Chla612	Chla613	Chla614	Lut620	Lut621	Vio622	Neo633
Chlb601	15405	-36	-5	-2	0	2	-2	-2	-2	-4	-9	3	-7	-3	0	0	1	0
Chla602	-20	14940	18	6	-1	-6	5	5	18	-10	-2	11	-6	-2	0	-3	0	0
Chlab03	-3	26	14850	5	-1	-10	1	3	63	-9	-1	2	1	-7	0	11	0	0
Chla604	2	-4	-9	14820	-3	78	-18	-3	-7	5	-2	0	0	-3	1	-5	0	4
Chlb605	0	0	0	6	15465	11	1	-3	0	-2	1	2	1	0	0	0	0	-1
Chlb606	2	-5	2	62	-23	15385	13	3	13	-3	2	3	2	2	0	2	0	-4
Chlb607	1	-3	-4	7	-3	10	15225	-3	-6	-1	-2	-2	-1	-3	0	-2	0	0
Chlb608	-2	4	-2	-6	-1	-11	-2	15215	-14	40	-3	-1	-1	-1	0	0	0	-3
Chlb609	3	-4	88	-4	0	-16	1	-19	15475	-1	-3	-1	-1	-2	0	1	0	1
Chla610	3	-9	-6	-1	1	-1	0	30	1	14790	-30	-12	-7	-2	4	0	0	0
Chla611	-14	9	1	-2	1	-2	-1	4	-2	-17	14950	131	-6	-4	1	0	0	0
Chla612	0	-8	-1	0	-1	3	1	-3	0	3	89	14940	4	1	12	-1	0	1
Chla613	-4	10	0	0	1	-1	0	1	-1	-4	1	-4	14840	-60	-3	0	3	0
Chla614	2	-9	-4	2	0	2	1	-1	1	1	-1	1	-18	14940	-1	0	2	0
Lut620	0	-1	0	0	0	0	0	0	0	3	1	6	-1	0	13963	0	0	0
Lut621	1	-2	7	-1	0	0	-1	0	1	0	0	-1	0	0	0	14113	0	0
Vio622	1	-1	0	0	0	0	0	0	0	0	1	0	3	5	0	0	14376	0
Neo633	0	0	0	6	0	-7	0	-9	0	-1	0	0	0	0	0	0	0	14472

Figure 6.4: The couplings (cm^{-1}) between all pigments in LHCII. The lower left half are those calculated in this study. The upper right half are from Chmeliov *et al.*[180] for comparison. The phase (sign) of the couplings are not important as they get squared when calculating the transfer rates. The couplings between Cars and any other pigment are very small due to the small change in charge density associated with a transition between S_1 and S_0.

For the CP29 couplings we compare with those calculated by Müh *et al.*[49] in the upper right hand half6.5. There is good agreement between the Chl-Chl couplings but as no group has calculated S_1-Q_y couplings, we have nothing to compare ours against. The energies of the Chls were also taken from the Müh study with the Car energies being processed in the same way as our LHCII Car energies.

Pigments	Chl*a* 602	Chl*a* 603	Chl*a* 604	Chl*b* 606	Chl*b* 607	Chl*b* 608	Chl*a* 609	Chl*a* 610	Chl*a* 611	Chl*a* 612	Chl*a* 613	Chl*b* 614	Chl*a* 615	Lut620	Vio622	Neo623
Chl*a* 602	**14980**	14	6	5	6	-7	-26	-4	0	7	-1	0	34			
Chl*a* 603	-13	**14900**	0	-3	5	4	81	6	-1	1	2	-4	-2			
Chl*a* 604	5	0	**14810**	67	24	-4	-5	-1	-3	2	2	-2	-3			
Chl*b* 606	4	3	49	**15684**	20	-3	-6	1	-2	2	2	-1	-2			
Chl*b* 607	4	-3	16	18	**15439**	-3	4	0	2	-1	-1	-1	-2			
Chl*b* 608	-5	-3	-2	-1	-2	**15439**	27	38	5	-1	-2	1	5			
Chl*a* 609	20	87	4	-4	4	-19	**14980**	-1	4	-1	-3	1	6			
Chl*a* 610	-5	-7	-2	-2	0	45	2	**14920**	-31	14	5	0	-9			
Chl*a* 611	0	-1	3	2	2	-4	4	24	**14850**	73	-3	1	70			
Chl*a* 612	-7	0	-1	-1	-1	0	-1	-9	102	**14900**	1	0	-1			
Chl*a* 613	2	2	-1	-1	-1	1	-2	-4	-3	0	**14880**	-9	-4			
Chl*b* 614	0	4	-2	-1	-1	1	-2	0	-2	0	1	**15674**	0			
Chl*a* 615	-32	-1	2	2	2	-4	4	7	40	1	-1	0	**14980**			
Lut620	0	1	0	0	0	0	0	-8	-1	4	5	1	0	**13963**		
Vio622	-4	5	2	1	1	0	-1	0	0	0	0	0	0	0	**14376**	
Neo623	0	0	5	9	1	-10	1	1	0	-1	0	0	0	0	0	**14472**

Figure 6.5: CP29 couplings (cm^{-1}): bottom left corner are our original calculated values, top right are the Chl-Chl couplings calculated by Müh *et al.*[49] for comparison

6.2.4 Transfer rates

The transfer rates between pigments were calculated using the Förster equation using the detailed spectral density fitted by Balevicious Jnr. (equation 4.2). Pigment groups with hopping times shorter than 1 ps, were taken as blocks. Excitonic behaviour was assumed within these blocks. The new states were calculated by block diagonalisation of the original couplings. The eigenstates were then used to calculate new couplings between these new states and the other pigments. Rates within the block were set to an artificially high value from high energy states to lower ones with Böltzman weighted rates in the opposite direction. This creates a realistic distribution of exciton probability density on each individual pigment.

In LHCII the pigment blocks were block 1: Chl a610, Chl a611 and Chl a612 and block 2: Chl a613 and Chl a614. In CP29 they were block 1: Chl a602 and Chl a615, block 2: Chl a603 and Chl a609 and block 3: Chl a610, Chl a611 and Chl a612. The process of taking the original calculated couplings to final rates including the excitonic blocks will be shown for CP29.

Hopping times (ps) $\tau_{mn} = k_{mn}^{-1}$ are displayed (figure 6.6). Any larger than 1 ns is assumed to be completely outcompeted by other paths and so has just been shown as > 1 ns, however, the calculated value was used in our modelling. We can see that the Chl-Car hopping times never fall into the excitonic regime due to their low couplings. The blocks of Chls as described above are evident and their hopping times have been displayed in green.

The resulting blocks on the Hamiltonian have been highlighted and diagonalised with the labels of pigments representing the states which most resemble those pigments (figure 6.7). The

Pigments	Chl*a* 602	Chl*a* 603	Chl*a* 604	Chl*b* 606	Chl*b* 607	Chl*b* 608	Chl*a* 609	Chl*a* 610	Chl*a* 611	Chl*a* 612	Chl*a* 613	Chl*b* 614	Chl*a* 615	Lut620	Vio622	Neo623
Chl*a* 602	-	3	32	>1 ns	338	221	1	34	>1 ns	7	120	>1 ns	0.34	>1 ns	>1 ns	>1 ns
Chl*a* 603	2	-	>1 ns	>1 ns	1316	779	0.07	12	187	>1 ns	108	>1 ns	236	>1 ns	>1 ns	>1 ns
Chl*a* 604	19	>1 ns	-	35	49	>1 ns	52	115	54	312	309	>1 ns	93	>1 ns	>1 ns	>1 ns
Chl*b* 606	>1 ns	>1 ns	>1 ns	-	8	>1 ns	>1 ns	>1 ns	>1 ns	>1 ns	>1 ns	290	>1 ns	>1 ns	>1 ns	>1 ns
Chl*b* 607	>1 ns	>1 ns	>1 ns	2	-	147	917	>1 ns	>1 ns	>1 ns	>1 ns	519	>1 ns	>1 ns	>1 ns	>1 ns
Chl*b* 608	>1 ns	>1 ns	>1 ns	475	147	-	42	228	>1 ns	>1 ns	>1 ns	>1 ns	>1 ns	>1 ns	>1 ns	>1 ns
Chl*a* 609	2	0.18	157	927	127	6	-	>1 ns	53	485	209	>1 ns	23	>1 ns	>1 ns	>1 ns
Chl*a* 610	16	8	93	>1 ns	>1 ns	8	269	-	0.81	8	20	>1 ns	12	>1 ns	>1 ns	>1 ns
Chl*a* 611	>1 ns	276	94	>1 ns	>1 ns	396	31	2	-	0.03	38	>1 ns	1	>1 ns	>1 ns	>1 ns
Chl*a* 612	9	>1 ns	723	>1 ns	>1 ns	>1 ns	370	22	0.04	-	>1 ns	>1 ns	185	>1 ns	>1 ns	>1 ns
Chl*a* 613	98	129	435	>1 ns	>1 ns	>1 ns	97	35	31	>1 ns	-	>1 ns	298	>1 ns	>1 ns	>1 ns
Chl*b* 614	>1 ns	>1 ns	>1 ns	276	>1 ns	>1 ns	>1 ns	>1 ns	>1 ns	>1 ns	>1 ns	-	>1 ns	>1 ns	>1 ns	>1 ns
Chl*a* 615	0.49	503	235	>1 ns	>1 ns	183	19	39	1	201	532	>1 ns	-	>1 ns	>1 ns	>1 ns
Lut620	>1 ns	>1 ns	>1 ns	>1 ns	>1 ns	>1 ns	>1 ns	53	>1 ns	174	153	>1 ns	>1 ns	-	>1 ns	>1 ns
Vio622	225	106	534	>1 ns	>1 ns	>1 ns	>1 ns	>1 ns	>1 ns	>1 ns	>1 ns	>1 ns	>1 ns	>1 ns	-	>1 ns
Neo623	>1 ns	>1 ns	120	47	>1 ns	31	>1 ns	>1 ns	>1 ns	>1 ns	>1 ns	>1 ns	>1 ns	>1 ns	>1 ns	-

Figure 6.6: The hopping times (ps) between pigment j (top row) to pigment i (left column) as calculated from our original couplings. Hopping times below 1 ps have been highlighted in green.

Pigments (Blocks)	B1:Chl*a* 602	B2:Chl*a* 603	Chl*a* 604	Chl*b* 606	Chl*b* 607	Chl*b* 608	B2:Chl*a* 609	B3:Chl*a* 610	B3:Chl*a* 611	B3:Chl*a* 612	Chl*a* 613	Chl*b* 614	B1:Chl*a* 615	Lut620	Vio622	Neo623
B1:Chl*a* 602	**14922**	-13	4	3	3	-6	-7	5	4	-2	0	0	0	0	-2	0
B2:Chl*a* 603	-13	**14844**	-2	5	-4	8	0	-2	-7	2	-3	4	17	1	5	-1
Chl*a* 604	4	-2	**14810**	49	16	-2	-3	3	-1	0	1	-2	-3	0	2	5
Chl*b* 606	3	5	49	**15684**	18	-1	2	2	-2	0	1	-1	-3	0	1	9
Chl*b* 607	3	-4	16	18	**15439**	-2	-2	2	0	0	1	-1	-3	0	1	1
Chl*b* 608	-6	8	-2	-1	-2	**15439**	18	-10	44	-4	-1	1	2	0	0	-10
B2:Chl*a* 609	-7	0	-3	2	-2	18	**15036**	-2	2	1	-1	-1	7	0	-2	-1
B3:Chl*a* 610	5	-2	3	2	2	-10	-2	**14766**	0	0	2	-1	-3	-2	0	1
B3:Chl*a* 611	4	-7	-1	-2	0	44	2	0	**14923**	0	5	0	42	-8	0	1
B3:Chl*a* 612	-2	2	0	0	0	-4	1	0	0	**14981**	-2	1	-8	-2	0	0
Chl*a* 613	0	-3	1	1	1	-1	-1	2	5	-2	**14880**	-1	2	-5	0	0
Chl*b* 614	0	4	-2	-1	-1	1	-1	-1	0	1	-1	**15674**	-1	1	0	0
B1:Chl*a* 615	0	17	-3	-3	-3	2	7	-3	42	-8	2	-1	**14998**	0	3	0
Lut620	0	1	0	0	0	0	0	-2	-8	-2	-5	1	0	**13963**	0	0
Vio622	-2	5	2	1	1	0	-2	0	0	0	0	0	3	0	**14376**	0
Neo623	0	-1	5	9	1	-10	-1	1	1	0	0	0	0	0	0	**14472**

Figure 6.7: These couplings have been adjusted after the block diagonalisation between pigments with hopping times less than 1 ps. The new blocks are between new states instead of the original Cars. We have left the original Car label in as the new states can be said to be made up primarily of the original Car states. The three blocks have been highlighted with individual colours.

couplings within the blocks has been set to 0 as the rates will be chosen rather than calculated through Förster.

The final hopping times are now displayed with new pigment to state hopping times calculated from the new Hamiltonian (figure 6.8). The rapid hopping within the excitonic blocks ensures effectively instantaneous thermalisation within these domains. The hopping times between Cars and Chls is consistently 'slow' over all interactions with the shortest hopping time of $\sim$ 30 ps being much longer than any excitonic interactions. Most Car-Chl hopping times are far too large to compete with other transfer pathways or dissipation.

With our calculated transfer rates and experimentally derived dissipation rates we can set

Pigments (Blocks)	B1:Chl*a* 602	B2:Chl*a* 603	Chl*a* 604	Chl*b* 606	Chl*b* 607	Chl*b* 608	B2:Chl*a* 609	B3:Chl*a* 610	B3:Chl*a* 611	B3:Chl*a* 612	Chl*a* 613	Chl*b* 614	B1:Chl*a* 615	Lut620	Vio622	Neo623
B1:Chl*a* 602	-	3	36	>1 ns	503	152	7	37	17	66	>1 ns	>1 ns	0.01	>1 ns	>1 ns	>1 ns
B2:Chl*a* 603	2	-	167	>1 ns	465	165	0.01	164	8	84	48	>1 ns	2	>1 ns	>1 ns	>1 ns
Chl*a* 604	21	142	-	35	49	>1 ns	62	42	172	>1 ns	308	>1 ns	69	>1 ns	>1 ns	>1 ns
Chl*b* 606	>1 ns	>1 ns	>1 ns	-	8	>1 ns	>1 ns	>1 ns	>1 ns	>1 ns	>1 ns	291	>1 ns	>1 ns	>1 ns	>1 ns
Chl*b* 607	>1 ns	>1 ns	>1 ns	2	-	146	>1 ns	>1 ns	>1 ns	>1 ns	>1 ns	520	>1 ns	>1 ns	>1 ns	>1 ns
Chl*b* 608	>1 ns	>1 ns	>1 ns	472	146	-	48	>1 ns	33	>1 ns	>1 ns	>1 ns	>1 ns	>1 ns	>1 ns	>1 ns
B2:Chl*a* 609	13	0.03	189	>1 ns	514	7	-	529	209	>1 ns	>1 ns	>1 ns	7	>1 ns	>1 ns	>1 ns
B3:Chl*a* 610	17	112	34	>1 ns	>1 ns	172	141	-	0.01	0.01	81	>1 ns	85	>1 ns	>1 ns	>1 ns
B3:Chl*a* 611	17	11	299	>1 ns	>1 ns	3	120	0.02	-	0.01	20	>1 ns	1	>1 ns	>1 ns	>1 ns
B3:Chl*a* 612	88	164	>1 ns	>1 ns	>1 ns	231	976	0.03	0.01	-	120	>1 ns	5	>1 ns	>1 ns	>1 ns
Chl*a* 613	>1 ns	57	434	>1 ns	>1 ns	>1 ns	595	143	16	73	-	>1 ns	83	>1 ns	>1 ns	>1 ns
Chl*b* 614	>1 ns	>1 ns	>1 ns	277	>1 ns	>1 ns	>1 ns	>1 ns	>1 ns	>1 ns	>1 ns	-	>1 ns	>1 ns	>1 ns	>1 ns
B1:Chl*a* 615	0.01	3	173	>1 ns	402	552	6	265	1	5	148	>1 ns	-	>1 ns	>1 ns	>1 ns
Lut620	>1 ns	>1 ns	>1 ns	>1 ns	>1 ns	>1 ns	>1 ns	718	44	953	150	>1 ns	>1 ns	-	>1 ns	>1 ns
Vio622	857	121	550	>1 ns	>1 ns	>1 ns	737	>1 ns	>1 ns	>1 ns	>1 ns	>1 ns	307	>1 ns	-	>1 ns
Neo623	>1 ns	>1 ns	125	44	>1 ns	30	>1 ns	>1 ns	>1 ns	>1 ns	>1 ns	>1 ns	>1 ns	>1 ns	>1 ns	-

Figure 6.8: These are the final hopping times (ps), calculated from the adjusted couplings. Key hopping times from Chls to Cars have been highlighted.

up a set of excitation population equations. Each pigment has a set of transfer to and a set of transfer from rates, as well as its own dissipation rate. These can then be used to describe the excitation population dynamics.

6.2.5 Lifetimes

The population dynamics then enables us to calculate a lifetime for the protein as the energy is dissipated from each pigment. Without Cars, the lifetime is set to 4 ns, following the Chl dissipation rate in detergent solubilised LHCII trimers and monomers. As in the Chmeliov *et al.*[180] model, this is reduced to deeply quenched with the introduction of the Cars. We calculate a lifetime of 169 ps which roughly matches predicted lifetimes of 130 ps by Ruban *et al.*[112] or the deeply quenched individual timers in the Chmeliov *et al.*[220] model (50-100 ps). However, it does not match the original lifetime measurements of the crystal by Pascal *et al.*[193] of ~ 0.78 ns. The possible reasons why we have predicted a lifetime consistent with deeply quenched LHCII aggregates in NPQ rather than the relatively shallow quenched lifetime measured by Pascal for the crystal will be discussed in section 6.6.

For CP29 we decided to measure our own fluorescence lifetime using two-photon excitation fluorescence lifetime imaging (FLIM). This was performed by Dr C. Ünlü and Prof. H. van Amerongen with the crystals being created by Dr Xiaowei Pan and Dr Mei Li. Their methodology can be found in our paper on CP29[230]. We measured the lifetimes for the intact CP29 crystals as well as detergent solubilised (isolated) CP29 monomers and re-dissolved CP29 crystals. In

each case, an appropriate laser intensity was chosen to avoid distortion of the traces due to singlet-singlet or singlet-triplet annihilation. The kinetics in the fluorescence traces of solubilised and redissolved crystals are almost identical with a mono-exponential decay of 4.89 ns and 4.86 ns respectively (figure 6.9a). This is comparable to the ~ 4 ns lifetime of detergent solubilised LHCII trimers as well as the $\sim 4-6$ ns lifetime of free Chl *a* in the protein environment of a typical LHC protein. The decay kinetics of the crystal are significantly faster and require a bi-exponential fit (figure 6.9b). The main component (0.94) is deeply quenched with a lifetime of 150 ps and the second component (0.06) has a lifetime of 4 ns. The most likely explanation for this pair of exponentials is that there is a free Chl which is disconnected from the main CP29 complex. This has probably been disconnected from the periphery of the protein and now lies in between monomers. This is in line with the crystal from the PSII supercomplex[14] which shows 14 Chls while our own crystal only has 13. We should therefore point out that the loose Chl *a*615 in the crystal used in this study is a mistake compared to the *in vivo* structure. These results are in stark contrast to the initial reports of mono-exponential, weakly quenched crystals for LHCII which is surprising given their structural homology. This discrepancy will be discussed in detail in section 6.5.

We used essentially the same model to calculate the lifetime for CP29. The only difference was that the CP29 Chls were optimised in vacuum rather than using cages. Justification for this can be found in section 6.5. As with LHCII, the inclusion of the Cars causes deep quenching of the natural 4 ns lifetime of the Chls. We predict a lifetime of ~ 200 ps which is only slightly longer than our model of LHCII. Figure 6.9c shows our predicted trace next to the experimental ones with and without Cars. We also add a bi-exponential decay trace to account for the proposed presence of an additional unconnected Chl. This gives a major (~ 0.93) quenched component of ~ 200 ps and a minor (~ 0.07) unquenched component with a lifetime of 4 ns. Our calculated lifetimes match our measured ones very well as can be seen by plotting the decay traces against each other.

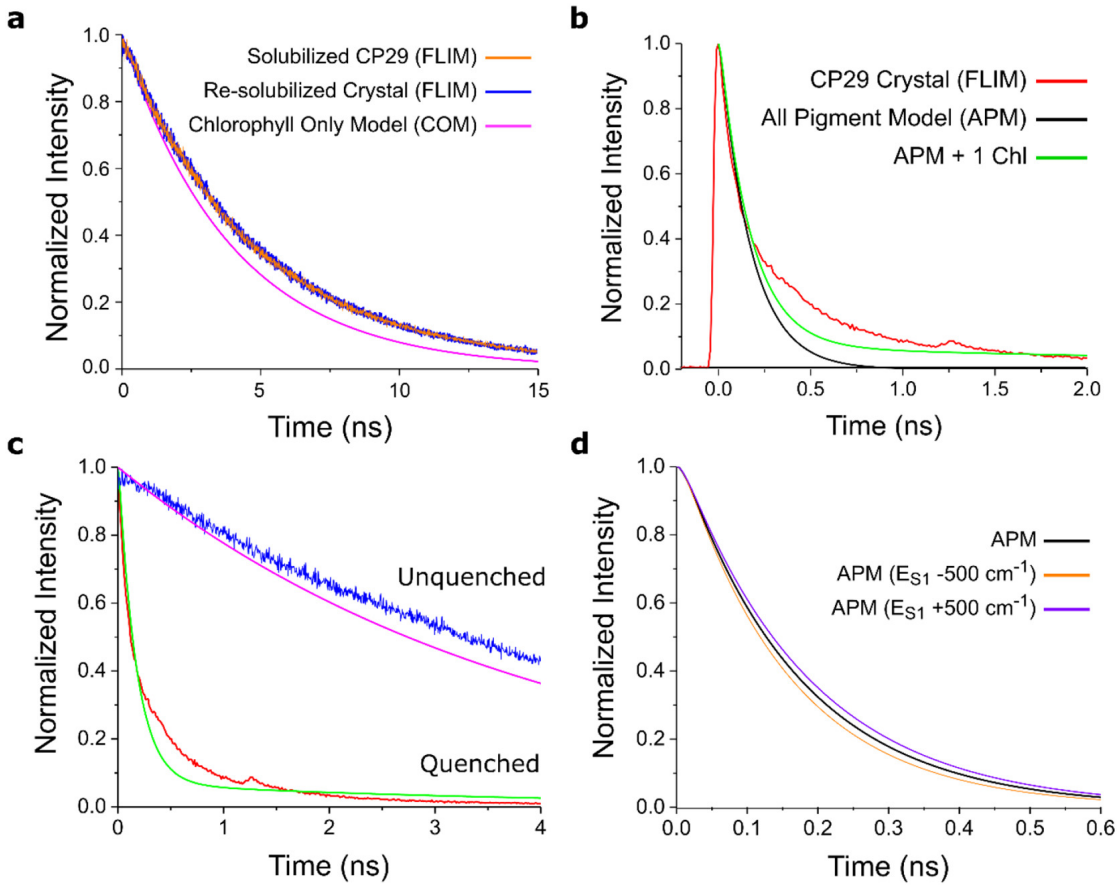

Figure 6.9: Fluorescence traces of CP29: **a**. solubilized monomers (orange), re-solubilized crystals (blue), simulated fluorescence trace for our model in wihc Cars are neglected (magenta). **b**. The crystal (red) with a feature at $1.0 < t < 1.5$ ns is attributed to weak reflection of the excitation beam due to placement of neutral density filters between laser source and sample. The trace as predicted by our model including Cars (black). The bi-exponential trace as predicted by our model with the inclusion of a disconnected Chl (green). **c**. A comparison of CP29 with and without Cars. The data presented is the same as from sections a. and b. following the same colour scheme. **d**. Here we show the traces when the energies of the Car S_1 states was changed by ± 500 cm^{-1}.

6.3 The quenching site

According to the Ruban *et al.*[112] model of NPQ, the Lut620 in the L1 position of LHCII is the primary quencher due to its proximity to the terminal emitter Chls. However, according to our models, there is significant excitation probability density on all Chl *a*s, leading us to believe that Lut621, in the very similar L2 position, would also quench a roughly equivalent amount. A plausible explanation for Lut620 being the predominant quencher came from the observations of Chang *et al.*[191]. While the L1 and L2 sites look symmetrical, Chang and co-workers showed that there are differences in the pockets, resulting in distinctions in the geometries of the two Luts (figure 6.10). My paper on the distortions of the xanthophylls[178] attempted to model this by using cage optimisations to preserve the different geometries and calculating the couplings with their nearest neighbour Chl (Chl *a*612 and Chl *a*603 respectively). The results (figure 5.2 in chapter 5) show a significant difference in coupling. This would appear to corroborate the Ruban model as the rate of transfer is dependent on the square of the coupling according to Förster. We were surprised to see how much the different geometries had affected the coupling and decided to apply the same cage mechanism to the whole protein.

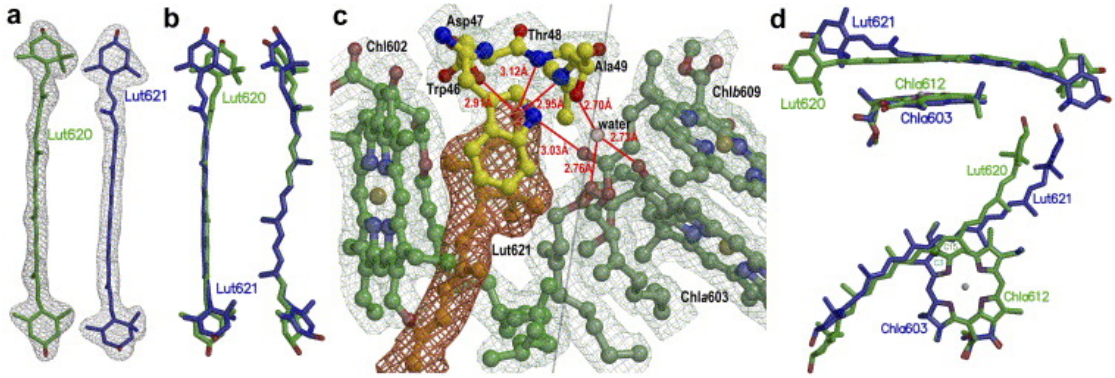

Figure 6.10: A figure taken from Yan *et al.*[191] which shows the difference between Lut620 and Lut621 in LHCII caused by the specific binding pockets.

The cages of the two Luts were redone along with all the other pigments. The results showed a drastic reduction in the coupling difference between the L1 (6 cm^{-1}) and L2 (7 cm^{-1}) sites with the Lut621-Chl *a*603 pair being the larger of the two. There are two possible explanations for this: firstly, the use of a cage optimisation on the Chl has distorted it enough to make this

large change in coupling. I believe this to be unlikely as the Chl Q_y state is not as sensitive to distortions as the S_1, due to the vanishing dipole of S_1 and its double dependence on symmetry. The second reason is that repeating the cage optimisation process has resulted in a different minima. The cages are large and complicated and it is likely that due to the small amount of randomness in the many optimisation steps, there has been a deviation at some point. This may call into question the validity of the cage process as it is potentially unable to replicate small but important distortions in the structure. However, I believe its use is valid for creating naturally distorted pigments, even if the distortions do not match the crystal exactly. We now have a selection of pigments which have reached an unconstrained minima, meaning the bond angles and lengths will not create any artificial issues with the excited states. They are also moved away from the completely planar which results in a more realistic symmetry. It is also worth remembering that while we are taking a single structure, even the crystal would have some movement and so attempting to assign a single set of structures to the properties of the crystal cannot be fully representative. We will therefore look for general trends and significant features rather than attempt to give accurate quantitative measurements.

When we calculate the portion of energy dissipated by each pigment in LHCII (Lut620 - 36%, Lut621 - 27%, Neo - 24%, Vio - 8%, Chl - 4%) (figure 6.12b), we see the similarity in coupling results in an expected similarity in the amount of energy quenched with discrepancy due to the proximity of the terminal emitter to Lut620. The surprising result here is the extent to which Neo contributes to the quenching. Neo is not expected to be a quencher in all models of NPQ and is often described as playing a structural role in the switch. Ruban *et al.*[112] noticed a correlation in Neo twisting with NPQ and this was later observed in the MD simulations of Liguori *et al.*[231]. Previous models predict low couplings between Neo and its neighbouring Chls (Chl *a*604 - 4 cm^{-1}, Chl *b*606 - 4 cm^{-1}, Chl *b*608 - 3 cm^{-1}). This was explained by the relative orientations, with the two L sites having a pair with a cofacial position and Neo not having this relationship. However, it does still have three Chls which are particularly close and I believe the proper treatment of Neo distortions has caused the TDC cloud to become less ordered. This has resulted in coupling with Chls which do not form the cofacial position (Chl *a*604 - 6 cm^{-1}, Chl *b*606 - 7 cm^{-1}, Chl *b*608 - 9 cm^{-1}) . The main reason we would not expect Neo to participate in the quenching is that two of these Chls are Chl *b*s. These have a higher energy Q_y and so

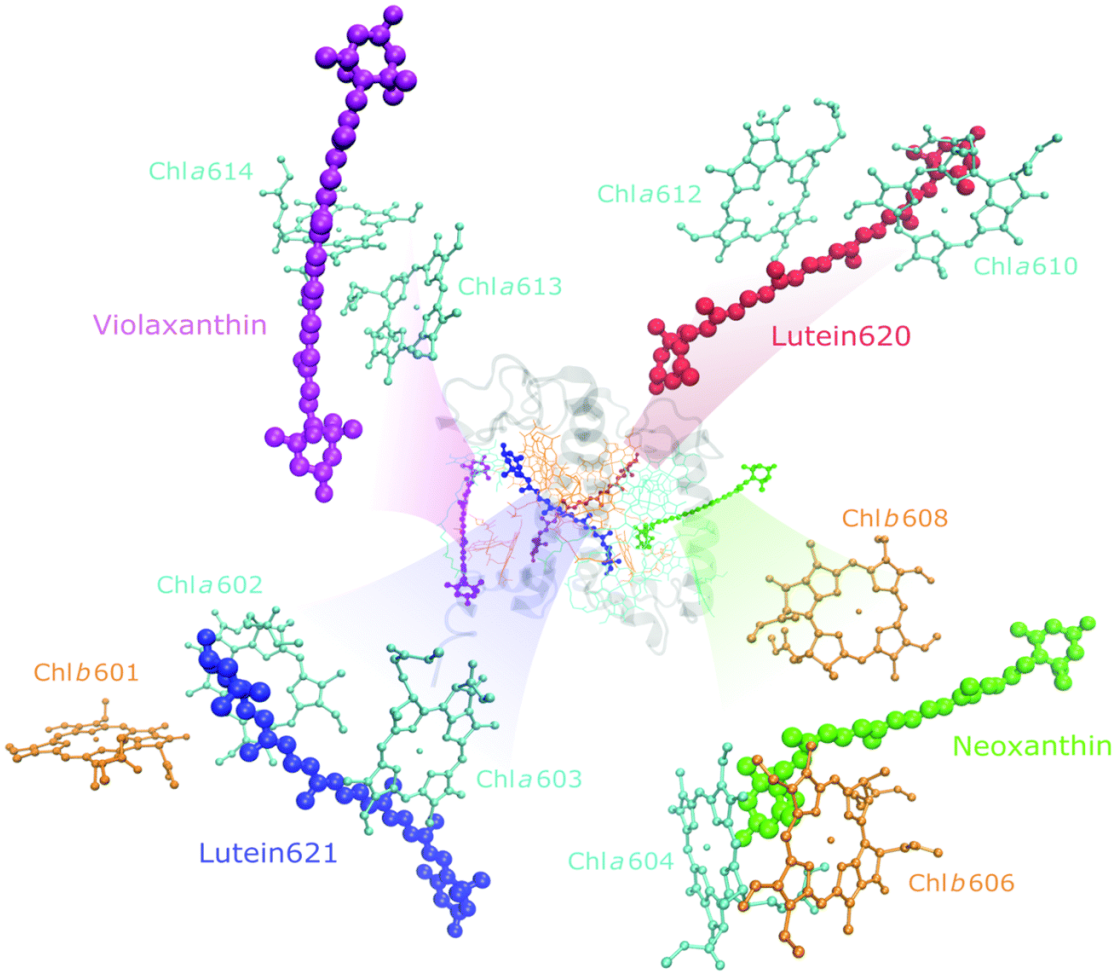

Figure 6.11: A schematic diagram of the LHCII monomer model structure used in our calculations. We have highlighted the 4 Chl–Car domains which are relevant when discussing potential quenching domains.

are less likely to be excited, instead transferring their energy to the Chl a pool. It is likely that in my model of isolated LHCII, the Neo has an elevated role in quenching as all pigments start with equal excitation probability density and it takes up to 500 ps for the lower energy Chl bs to lose essentially all of it (figure 6.15). There can therefore be significant transfer during this period. In the membrane, much of the energy in any one LHCII unit would have been transferred from neighbouring proteins and would be in the Chl a pool. However, the third Chl a is still significantly coupled to the Neo resulting in some quenching by Neo regardless.

If we compare the L1, L2 and N sites in CP29, we see the trend of increased coupling between

Cars and non-cofacial Chls continuing. The Lut at the L1 site is now coupled to Chl $a610$, Chl $a612$ and Chl $a613$. At the L2 site, the Lut621 is replaced with a Vio which we calculate as having significant coupling to both Chl $a602$ and Chl $a603$. We therefore predict that no special Car or Car-Chl relationship is needed for significant couplings. The only key aspect is a proximity due to the way in which the dipole ~ 0 S_1 state couples. The interactions with specific parts of the transition charge cloud become averaged out at great distances and as they start off small, only neighbouring Car-Chls can couple. We therefore predict that all Cars are sites of quenching but that those at the L1 and L2 sites quench significantly more due to their proximity to low energy Chl as. In this regime, the quenched state of the protein is simply one where the Cars are allowed to slowly quench from the Chl a pool. The light-harvesting state is the unique and difficult to determine one as it has to arrange its pigments in such a way as to avoid Q_y-S_1 interaction in a densely packed protein.

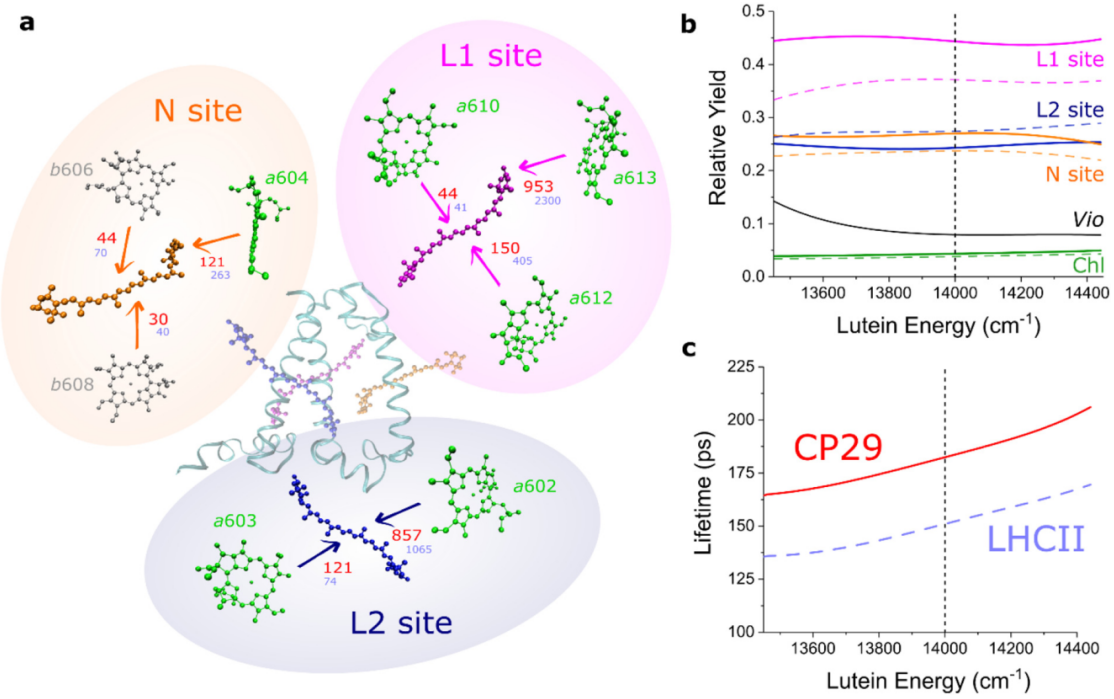

Figure 6.12: **a**. The key Car sites, expanded for clarity. Hopping times (ps) are displayed between the closest Chls for LHCII (blue) and CP29 (red). **b**. The relative quenching yield of the Cars in LHCII (dotted apart from Vio) and CP29 (solid). These have been plotted agaisnt Lut energy as a representative for each Cars S_1 energy scaling. **c**. The Chl fluorescence liftimes plotted agaisnt Car S_1 energy.

6.4 The switch

We look to the Förster equation to describe the Q_y-S_1 interaction. It is dependent on both coupling as well as spectral overlap and so for the interaction to reduce, one of these parameters must be reduced. The spectral overlap depends on the spectral density as well as the position or energy of the state. As we have described in section 4.2.1, the S_1 energy is particularly hard to determine owing to its two-electron nature. This caused us to question if the actual energy could be at some cusp point where natural changes in the S_1 energy could reduce the spectral overlap enough to shut off the Car-Chl interaction. Our new spectral density which replaced the extremely broad over-damped Brownian oscillator made this possible as the sides are much steeper.

Measurements of the Lut S_1 energy range from 14050 - 15300 cm^{-1} depending on the conditions and the method used. We use the most recent Walla two-photon absorption, measured in native LHCII which gave an energy of 15300 cm−1[176]. However, this value is the centre point of a single peak fitting to the complex data. When we use our own fitting to create vibrational structure, we notice that the first peak which represents the 0-0 transition is $\sim$ 1300 cm−1 lower in energy. This value was determined from the average of the two Raman peaks corresponding to C-C and C=C stretching. We are therefore left with a Lut S_1 energy of $\sim$ 14000 cm−1. From this we use our calculated Car energies to scale the rest of the Cars by the ratio between our calculated and this experimental Lut energy. we then calculate various parameters in a range ($\pm$500) around this point and display them according to the Lut energy.

Figure 6.12c shows the change in lifetime of LHCII and CP29 when varying the Car energy. We can see that there is very little change ($\sim$ 10%), even when the Car energy is varied by as much as 500 cm−1. This is also displayed in the decay traces when the $\pm$500 cm^{-1} is applied (figure 6.9d). We would not expect the Car energy to be able to climb or fall more than this, even given the natural inaccuracies in the starting point. The invariance is a result of the similarities in the Q_y and S_1 energy as well as the relatively broad and flat top of the S_1 spectral density. The detail of the triple peak can be faintly detected in the lifetime relationship with energy but much of the definition has been lost as the various Cars have slightly different energies. We can also see from figure 6.12b that the quenching proportions are not greatly affected by the scaling

energy even though they all have different S_1 levels. The greatest difference in energy between the lowest energy Car (Lut) and the highest (Neo) is ~ 700 cm^{-1} and the Chl Q_y fluorescence peaks all lie well within the broad Car absorption peaks for either. From this we conclude that variations in the state energy levels is very unlikely to play a significant role in NPQ.

This indicates that in order for the Chl-Car interaction to be switched, giving the dissipative and light harvesting states, the coupling must be variable within the protein. We have already seen in chapter 5 how this is possible, proposing that a change in mutual orientations of the molecule is probably the cause with potential effects from Car distortions playing a role. We wanted to investigate how much the couplings would have to be reduced as well as on how many of the quenching pathways. However, with our static structures we had no way of naturally varying the couplings. We therefore decided to reduce the couplings in simple *ad hoc* ways to give an early indication of what is needed for the switch (table 6.3). Scheme **A** represents the system as it was calculated and scheme **B** has had the couplings uniformly reduced by a scaling factor of 0.2. This rather large scale reduction was necessary for the overall lifetime to reach close to the expected lifetime for a light harvesting protein of ~ 2 ns. Obviously, the uniformity of this reduction is unrealistic but it is notable that the coupling needs to reduced until the Car-Chl interaction is almost completely turned off for light-harvesting function. It is only because of the large, rigorously forbidden two-electron portion of the S_1 which makes this possible. Schemes **C**, **D** and **E** have selectively decoupled the Neo-Chl, Lut621-Chl and Lut620-Chl interactions respectively. The decoupling of Vio has not been considered as it contributes so little to overall quenching. The removal of Neo has had very little effect on the overall quenching as to be expected as it has the most minor of the three main quenching pigments. Surprisingly the removal of one of the Luts also has little effect on the lifetime. The energy seems to simple redistribute to be quenched by the remaining pigments. Effectively if one Car is removed, this increases the amount of energy left in the Chl pool. As the probability transfer to the remaining Cars is proportional to probability density on the Chl, there is increased transfer to the Cars. Even more surprising is that scheme **F**, which has both of the Luts removed, has only a limited effect on the lifetime while most NPQ models would have predicted a light harvesting state. We have already mentioned how the quenching yield of Neo may be inflated in our model but it still shows that the bulk reorganisation of the protein should have an affect on all the quenching

pigments to reach the relatively long light-harvesting lifetimes.

Scheme	Lifetime (ps)	Details
A	169	Original couplings
B	1812	Couplings scaled down
C	205	No Neo
D	232	No Lut621
E	245	No Lut620
F	417	No Lut620 and Lut621

Table 6.3: Chl fluorescence lifetimes of LHCII with *ad hoc* alterations to the Chl-Car couplings

6.5 LHCII vs CP29

There has been a number of conflicting ideas on the site of NPQ as discussed in section 6.1.2. Our FLIM lifetime measurements of CP29 corroborate with the various models of NPQ which predict quenching in the minor antenna and with our model, we were able to investigate the mechanism. The structural homology between LHCII and CP29 would indicate very similar processes in both. However, there are a few discrepancies in the Chl sites as well as key differences in the Cars. CP29 lacks the peripheral Vio and has a centrally bound Vio at the L2 site instead of the Lut621 in LHCII (figure 6.13).

If we compare the structural similarities at the three CP29 Car binding sites we can see just how similar the two proteins are. The Cars in figure 6.14a have been overlapped with the Chl positions marked in red for CP29 and blue for LHCII. While the Chl positions mostly overlap, we have already seen how small differences in mutual orientation can create significant discrepancies in the couplings. We have plotted the Car-Chl couplings in LHCII against those in CP29 for all pairs preserved across both proteins (figure 6.14c). The expected interactions are significantly large > 2 cm^{-1} in both, with the remaining majority being between distant pairs resulting in negligible interaction. The three important Neo-Chl couplings are with Chl a604, Chl b606 and Chl b608 (in CP29: ~ 5, ~ 9 and ~ 10 cm^{-1} respectively). This is very similar to LHCII ($\Delta J \approx 0.5 - 2$ cm^{-1}). There is a slight discrepancy between the two proteins at the L2 site with the Vio of CP29 coupling to Chl a602 (~ 4 cm^{-1}) and Chl a603 (~ 5 cm^{-1}) but the Lut in LHCII only really coupling to Chl a603 (~ 7 cm^{-1}). This could be explained by the change

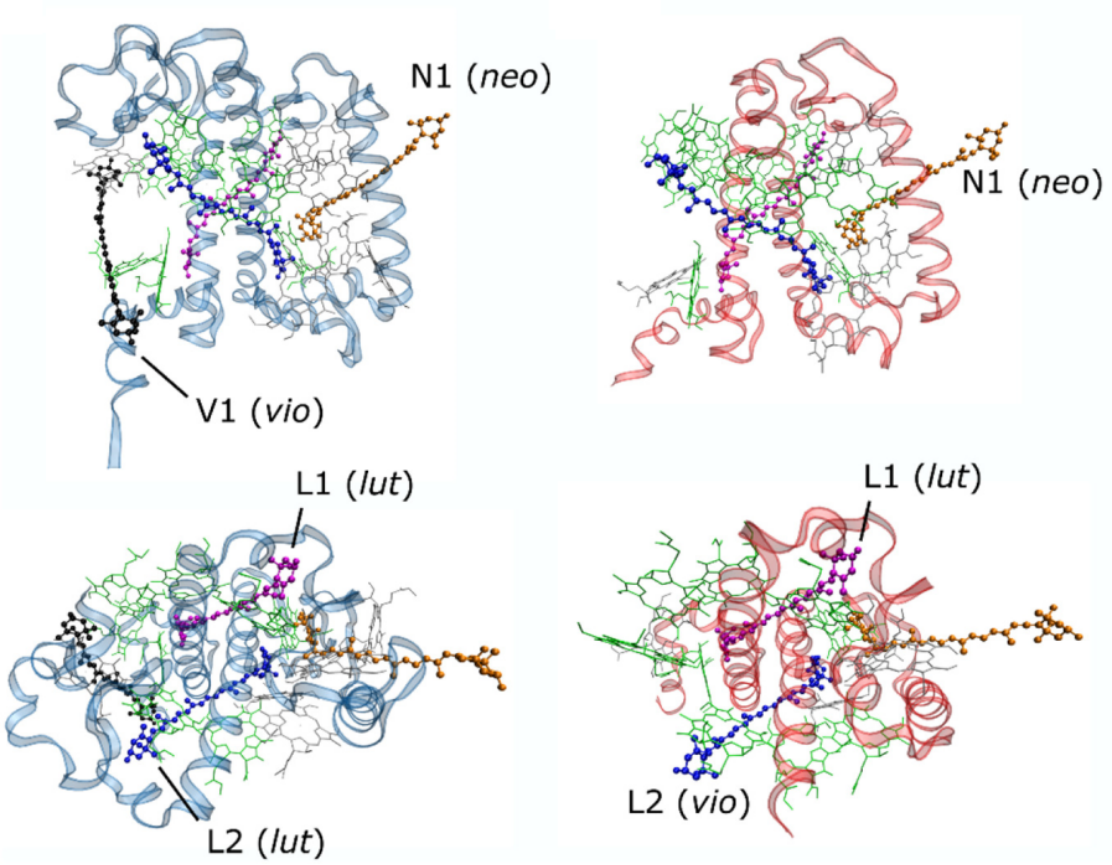

Figure 6.13: A schematic image of LHCII (blue) and CP29 (red) from two different angles. The top images are observed from the plane of the membrane with the bottom being the stromal side. The bottom images are looking down from the opposite side. Car domains are highlighted and Chl *a*s and *b*s are represented by green and grey respectively

in Car but I believe this to be unlikely as both Cars have almost identical excited states and because there is a similar discrepancy at the L1 site where there is a Lut in both proteins. The L1 domain shows the largest structural difference between CP29 and LHCII (figure 6.14) and this has manifested into the largest coupling changes. In LHCII, the Lut is only significantly coupled to Chl $a612$ (~ 9 cm^{-1}) with interactions with other neighbouring Chl (Chl $a610$ - ~ 3 cm^{-1} and Chl $a613$ - ~ 2 cm^{-1}) being almost negligible. In CP29 there is a drastic reduction in the Chl $a612$ (~ 4 cm^{-1}) coupling with a concomitant rise in the other two (Chl $a610$ - ~ 7 cm^{-1} and Chl $a613$ - ~ 4 cm^{-1}). It should be noted that we do not expect these couplings to be exact, nor necessarily preserved over time. They simply indicate typical Car-Chl interactions at the main Car sites.

There is a marked difference in the L1 and L2 sites, with the coupling being predominated by one interaction in LHCII and spread over multiple in CP29. This is particularly interesting as we have mentioned how in LHCII, a small change in the position of the Car may be responsible for the reduction in coupling we associate with the light-harvesting state. However, we now see that this movement may also increase the interaction with another nearby Chl. In CP29, all of the significant Car-Chl interactions would need to be reduced which become much more complicated due to how many there are. We can also predict that the Cars in membrane-LHCII may form these extra interactions due to the structural homology and natural thermodynamic movements. If we also consider how each quenching site is important and must be reduced in order for light-harvesting, we can conclude that the light-harvesting structure must be very specific or particular. This is in contrast with the typical line of thought that a special conformation turns the Car-Chl interaction on, resulting in a dissipative state. This will be discussed further in chapter 7.

The final point with respect to couplings is the similarities between the Chl dynamics of both structures. Figure 6.14b shows that while some Chl-Chl couplings may differ, the larger interactions are preserved in both. If we look at the dynamics of both proteins, the coupling differences have not had a significant effect compared to the Chl a/b located at each site. With the entire Chl pool being well connected, the energy levels have dominated the dynamics and a simple Böltzman distribution is quickly established. For this reason the most important factor for excitation probability density is the Q_y energy difference between Chl a and b. It should be

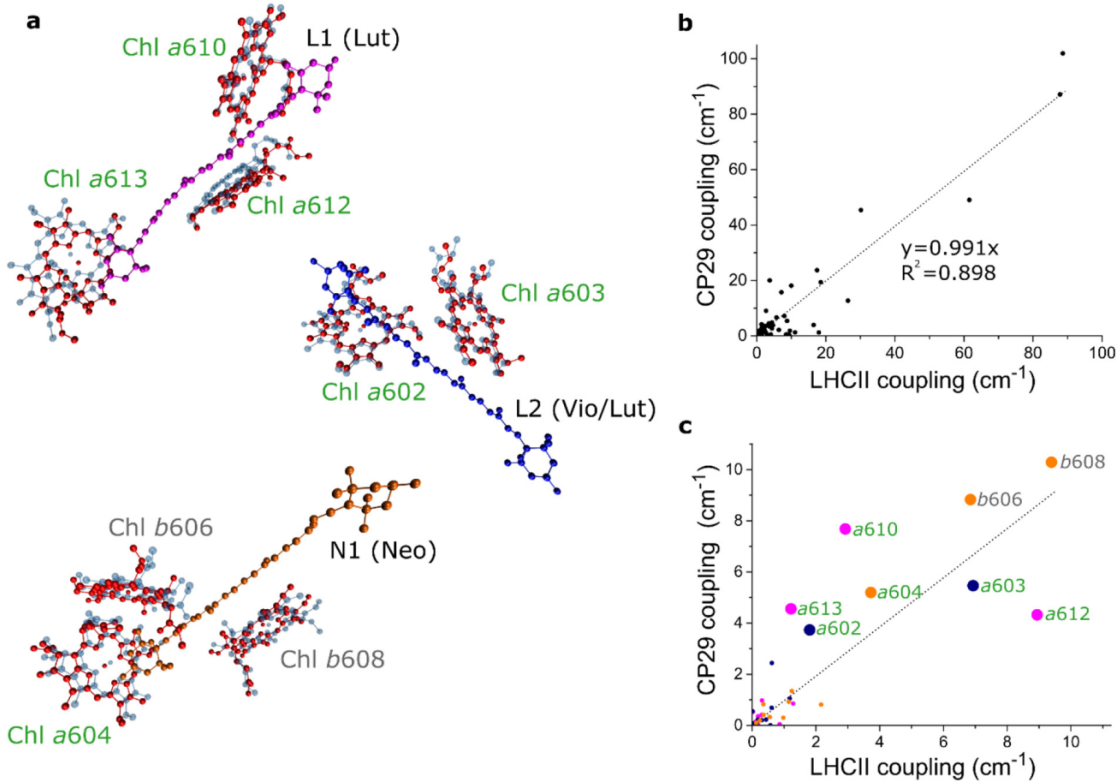

Figure 6.14: A comparison of the pigment interactions between LHCII and CP29: **a**. The three Car domains in CP29 with the positions of the Chl relative to the Car in red for CP29 and blue for LHCII. **b** The Chl-Chl couplings where the same interaction exists in both proteins, plotted against each other. The line of best fit is displayed to show the similarities between the two structures. **c**. The Chl-Car couplings in each protein plotted against each other. Key interactions are presented in bold with the Chl labelled. The colours represent the different Cars: L1 - magenta, L2 - blue, N - orange.

noted that while there is less population density on the Chl b pigments, it is not reduced to ~ 0.

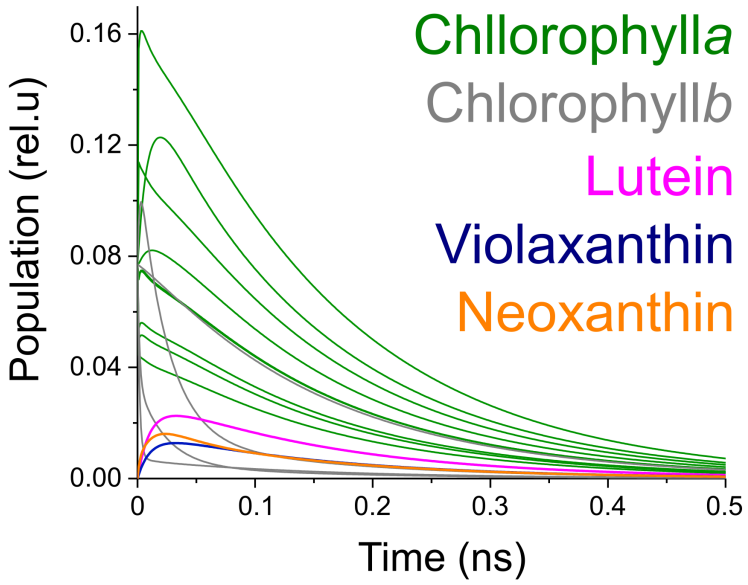

Figure 6.15: The population density for the excitation to be located on each pigment in CP29 over time.

These detailed changes have resulted in very little difference to the lifetime of the protein or the quantum yield of the specific quencher. The only noticeable change has been an increase in the quenching yield of the L1 site. This is partially because of an overall increase in the L1-Chl couplings compared to L2 or Neo and partly because the slightly higher energy of the CP29 Vio S_1 (rather than Lut in LHCII) at the L2 position has resulted in slower energy transfer from the Chl pool. However, it is notable that there is still significant quenching at the L1, L2 and N site in both proteins. The longer lifetime of CP29 is probably due to the slower energy transfer to the Vio at the L2 site as well as the small reduction in quenching associated with the missing peripheral Vio. However, it should be noted that while our calculated CP29 lifetime matches the experimental very well, this is not the case for LHCII.

6.6 The lifetime

The crystallization of CP29 leads to a strongly quenched state $\tau \sim 177$ ps. This matches our calculations (~ 200 ps) very well as we are not attempting to reproduce quantitative data

but instead follow general trends such as deep quenching. There is, however, a considerable discrepancy between our calculated lifetime of LHCII ($\sim$ 150 ps) and the measurements of Pascal *et al.*[193] of $\sim$ 890 ps.

There is a degree of uncertainty in the treatment of the S_1 state in our model due to the difficulty in directly observing it. The reported experimental range of energies is 14050 - 15300 cm^{-1} and these all use a single broad peak to describe the state with the centre point being the energy. One might therefore expect this to be a potential source of error for our calculated lifetime but we have seen that the lifetime is relatively invariant to the S_1 energy. Therefore, the more reasonable explanation for our failure to reproduce the lifetime measured by Pascal *et al.*[193] is an overestimate of the Chl-Car couplings. This could be an issue with how we scaled the couplings to the dipole moments. For the Chls, scaling is simple as experimentally reported dipoles are available. However, it poses a problem with the Cars as all we know is that the dipoles are approximately zero ($\mu =\sim$ 0 D). We have scaled to our calculated dipoles but as they are so low, small changes in the dipole moment can have a significant effect on the scaled couplings. Another possibility for the overestimate is that the optimisation step, necessary for excited state calculations, has removed some important fine detail in the structure. We have already seen how small structural differences can result in large variations in coupling. It is possible that this structural detail was present in the LHCII crystal but not in the CP29 resulting in the different measured lifetimes but similar calculated ones between the two proteins.

Barros *et al.*[188] reported a multi-exponential fit for the lifetime of LHCII crystals with a short lifetime component of $\sim$ 270 ps and two longer components of $\sim$ 900 ps and $\sim$ 3.8 ns although the short lifetime was attributed to quenching processes outside of the LHCII protein. van Oort *et al.*[232] repeated these measurements on crystals with different morphologies. They provided both a mono- and bi-exponential fitting with the latter giving the better fit. It was composed of a deeply quenched ($\tau \sim 330 - 480$ ps) component with an amplitude of $75 - 90\%$ and a slower component ($\tau \sim 750 - 1000$ ps). Crucially the deeply quenched component was determined to have arisen from quenching mechanisms within the protein. They mention that this bi-exponentiality may have arisen due to baseline effects giving a mono-exponential lifetime of ($\tau \sim 440 - 570$ ps). This still represents a deeply quenched state, with a shorter lifetime than the Pascal *et al.*[193] measurements. They attribute this difference to technical improvements since

the Pascal study. We propose that it is reasonable to compare our results relatively favourably to these newer measurements due to the similarities of the crystals and the natural deviation from the original structure during optimisation. This also fits with our suggestion that the lifetime and NPQ mechanisms would be similar in CP29 and LHCII due to their similar structures.

Chapter 7

Conclusions

The Chl dynamics within LHCII and CP29 have been well documented, both experimentally and theoretically. Their excited state energetics are characterised by two key properties. Firstly, the Q_y energy of the Chl bs is significantly higher than that of the Chl as. This results in a rapid depopulation of the Chl b level, happening on a timeframe of $\sim 5 - 500$ ps, depending on the energy of the specific Chl b. The second is that within the Chl a block, one or a group of them will be the lowest in energy. These will take a higher proportion of the excitation energy. In LHCII, a cluster of three Chl as near the L1 site have the lowest energy Q_y state. Energy is localised here and is funneled from protein to protein towards the RC. For this reason it is called the terminal emitter.

In a Chl only model of a single protein, the system will rapidly reach thermal equilibrium and quench slowly with a lifetime of 4 ns. If there is a Car within Van der Waals contact of a Chl, unless there is some specific mutual orientation, it will couple. This then leads to energy transfer, dependent on the energy probability density of the Chl, and a consequential decrease in the lifetime of the system. My model shows that all Cars will therefore quench to some degree, with the two Luts quenching considerably more due to their proximity to Chl as with high excitation probability density. This is in contrast to many models which predict specific Cars as the quenching sites and specific interactions needed to turn the quenching pathway on.

Our models of LHCII and CP29 do not include CT transfer states due to the non-adiabatic

nature of these states. There would therefore need to be considerable improvements to current quantum chemistry methods to treat the S_1 state. We have also excluded excitonic interactions between Chl and Car. The transition density of the S_1 state is almost zero due to its predominantly 2-electron nature. This is robust against distortions as it is only broken by disrupting the alternacy symmetry. Stretching modes which do this such as C-C and C=C stretching are particularly high in energy and are unlikely to be highly populated, resulting in perpetually low Chl-Car couplings. For excitonic effects to become significant

$$J_{S_1-Q_y} >> |\varepsilon_{S_1} - \varepsilon_{Q_y}| \tag{7.1}$$

must be true. This provides only a very narrow window for the fluctuating energies to be within. For this reason, I believe that the excitonic effects are likely to be rapidly dephased due to environment/solvent effects. Our models show that slow transfer to the Car S_1 state is an effective quenching mechanism without any excitonic interactions. While we have some discrepancies in our $S_1 \rightarrow Q_y$ transfer and our LHCII lifetime, the Chl fluorescene lifetime of both complexes dropped to levels of deep quenching. These slow processes are more consistent with the timeframe of NPQ and are supported by the Chemeliov *et al.*[220] three-state model of NPQ in the membrane.

Our mechanism of quenching through slow, incoherent transfer from Chl *a* to Car has been proposed by many groups to explain various transient absorption spectra. It is consistent with the findings of Belgio *et al.*[215] who predict that quenching occurs at many slow trapping sites which are outcompeted by the open RC. The traps in our models of LHCII and CP29 are highly effective at reducing the lifetime of the system but at $\sim 150-200$ ps are much slower than the rate of inter-protein transfer ($\sim 15-25$ ps)[233]. This mechanism, while still debated in higher plant proteins, has been unambiguously observed in other light harvesting systems. Cyanobacteria have a set of light harvesting proteins called high light-inducible proteins (Hlip) of which HliD has been found to contain Chl a/b and β-carotene. This is an ancestor of LHCII and is a simple enough system to directly observe quenching via direct energy transfer from $Q_y \rightarrow S_1$[234]. This at least provides proof of principle for our quenching mechanism.

This model of quenching is quite simple with slow incoherent processes dominating. our

simple model for quenching is consistent in both LHCII and CP29 as a result of the high degree of structural homology. There are some differences in the Chl dynamics but these would have to be extreme to have any impact on the quenching pathways. We see variation in the Car species which also seems to have little impact as the key characteristics: an almost zero transition density and a short lived S_1 state, are present in each. For these reasons we do not expect totally different mechanisms of NPQ in the other minor antenna, with changes to the Chl dynamics and Car composition only making small impacts on the quenching pathways.

Not only are the proteins packed with so many Chls that one would expect considerable Chl only quenching mechanisms, they are also in close proximity to Cars, which we know are energetically connected due to their role as light harvesters. The question therefore becomes, how does the plant arrange these pigments so as to light harvest at all? Within the Chl only model it does this by very specific spatial arrangements as well as energetic funnelling in order to shuttle excited state energy to the RC as fast as possible. We are then left with how the plant avoids the problem of Cars quenching any energy on its way to the RC. In light harvesting conditions, the energy traps are so slow as to give a LHCII lifetime of 2 ns when the RC is closed (or disconnected). Our modelling has shown that it is essential that the coupling between both Luts and their nearby Chls are drastically reduced for this to happen. We know that this cannot happen via some energetic change in the Car excited states as the spectral density (DOS) is broad. It therefore has to be either a change in the transition density moments, which is quite hard to achieve as the state transition is robustly forbidden, or a movement in the mutual orientations of the pigments. This would also seem unlikely as the Cars are surrounded by pigments and so a change in position to reduce the coupling between one pair may well increase the coupling in another. We see an example of this in CP29 where the main Car-Chl pair couplings have reduced (compared to LHCII) but other Car-Chl pairs have increaed to compensate. However, the initial MD work by Balevicius Jnr. *et al.*[198] shows how sensitive and ordered the changes in coupling can be to key movements of the pigments. We know from single-molecular spectroscopy that the antenna proteins can exist in distinct and stable light harvesting and quenched states. We therefore contend that the plant has a specific arrangement of its Cars and nearby Chls to allow for light harvesting which is energetically protected. This favourable state is then broken by protonation and/or aggregation to allow the large number of slow, naturally dissipative processes

to provide photoprotection when necessary. We do not attempt to offer details on this specific arrangement of pigments as the myriad of changes in the spatial relationships of the array of pigments are too complex to reduce down to single coordinate schemes. However, we suggest that a targeted MD approach towards finding the 'light-harvesting state' would prove a particularly fruitful approach to understanding the switch mechanism.

7.1 Approaching the light harvesting state

The most significant progress in producing a structure for light harvesting state of LHCII to date is the work of Liguori *et al.*[231]. They produced a series of 1 μs MD simulations, starting from an equilibrated crystal structure. They observe significant movement in the most commonly proposed quenching site of the L1. This is coupled to movements of Neo which have been significantly linked to the switch[112]. However, these MD runs are unlikely to have reached the light harvesting state. While the simulation was run for 1 μs, the states are typically metastable at $\tau \sim 1-10$ s. However, we do agree that certain movements, consistent across all runs, suggest the structures are moving in a particular direction on the PES. This could be towards the light harvesting state and a study of the S_1-Q_y couplings would be particularly interesting.

Our own group's investigation into this area, in collaboration with Mennucci and co-workers, is rather limited and we do not claim to move towards the light-harvesting structure. Rather we show the typical variation in the interactions of a couple of key Car-Chl pairs over time. We wanted to investigate the stability of the mutual orientation between the key Lut-Chl interactions. A 1 μs simulation of the LHCII trimer was run with 1000 snapshots taken at every 1 ns. On everyone of these, planar Lut and Chl *a* was superimposed onto the Lut620 and Chl *a*612 and Lut621 and Chl *a*603 positions. This was done so as to have properly optimised structures, suitable for excited state calculations. We then calculated couplings and show a fairly dispersed set of results which averages at $\sim$ 3 cm^{-1}[198]. With such variable results, it is clear that a single structure could be very misleading. We used these couplings to make up a simple model giving a lifetime of the protein from FRET rates. The results show a period of particularly high fluctuations until the system seems to find a more stable conformation. At this point we still see fluctuations but the structure clearly stays in a quenched state ($\sim$ 858 ps) throughout.

It is worth noting that these only take the mutual orientation and distance relationship of the pigments into consideration and any detail from distortions to the conjugated chains is lost.

It is clear that a MD simulation which focuses on maintaining structures suitable for S_1 calculations is needed. This should be paired with the formulation of software to calculate S_1-Q_y couplings, quickly enough to be feasible for the many snapshots of a long run. With this we could supplant the use of single structure crystal structures, giving results which avoid errors due to an unusual starting structure. It would also enable us to search for the illusive light harvesting structure. We have argued that this structure is 'special' and have shown how easy it is for movements of the pigments to enable quenching via the Cars. It would therefore be very convincing if we could calculate the lifetime of a structure over time where the average was in the light harvesting range of ~ 2 ns. The protein states are metastable at $\tau \sim 1 - 10$ s which is out of the realistic range for MD trajectories without significant resources. We therefore suggest a 'steered'[235, 236] simulated annealing approach where we artificially alter the conditions to encourage rapid switching to the light harvesting state. At this point the trajectory can then be stabilised in realistic conditions.

Appendix A

List of abbreviations

AM1	Austin model 1
ATP	adenesine tri-phosphate
BChl	Bacterial Chlorophyll
BLA	bond-length alternation
Car	Carotenoid
CASSCF	complete active space self-consistent field
Chl	Chlorophyll
CNDO	complete neglect of differential overlap
CSF	configuration state functions
CT	Charge transfer
Cyt	Cytochrome
DoF	Degrees of Freedom
DFT	Density Functional Theory
DOS	Density of States
ETC	electron transport chain
FAB	filamentous anoxygenic bacteria
Fd	ferredoxin
FLIM	fluorescence lifetime imaging
FNR	Ferredoxin $NADP^+$ Reductase
FRET	Förster resonance energy transfer
GGA	Generalised gradient approximation
HF	Hartree-Fock
HliP	high light-inducible proteins
HMO	Hückel molecular orbital
HOMO	Highest occupied molecular orbital
INDO	intermediate neglect of differential overlap
KS	Kohn-Sham
LDA	Local density approximation
LH1	light harvesting 1
LH2	light harvesting 2

LHCII	Light Harvesting Complex II
LUMO	Lowest unoccupied molecular orbital
Lut	Lutein
MD	Molecular Dynamics
MIND0	modified intermediate neglect of differential overlap
MNDO	modified neglect of differential overlap
MO	Molecular orbital
NADP	Nicotinamide adenine dinucleotide phosphate
NDDO	neglect of diatomic differential overlap
Neo	Neoxanthin
NPQ	Non-photochemical quenching
OEC	oxygen evolving complex
ox	oxidised
PAR	photosyntheitcally active region
PCP	Peridinin-Chlorophyll-protein
PES	potential energy surface
PMX	Protein model
PPP	Pariser Par Pople
PSI	Photosystem I
PSII	Photo-System II
Q	quinone
RC	reaction centre
red	reduced
RSDM	reduced system density matrix
SAC-CI	symmetry-adapted cluster configuration interaction
TD-DFT	Time dependent density functional theory
TDM	transition density matrix
TDM	transition density moment
Vio	Violaxanthin
ZDO	Zero differential overlap
Zea	Zeaxanthin
vac	vacuum

Bibliography

[1] Falkowski P., R. J. *Aquatic Photosynthesis, 2nd Edn.*; Princeton Univ. Press: Princeton, NJ, 2007.

[2] R.E., B. *Molecular Mechanisms of Photosynthesis*; Wiley Blackwell: Chichester, 2014.

[3] Green B.R., P. W. *Light Harvesting Antennas*; Kluwer Academic Press: Dordrecht, 2003.

[4] Boone D.R., C. R. W., Garrity G.M. *Bergey's Manual of Systematic Bacteriology: Volume One: The Archaea and the Deeply Branching and Phototrophic Bacteria 2nd Edn.*; Springer: Dordrecht, 2001.

[5] Dworkin M., R. E., Falkow S. *The Prokaryotes 3rd Edn.*; Springer: Berlin, 2006.

[6] Blankenship R.E., B. C., Madigan M.T. *Anoxygenic Photosynthetic Bacteria*; Kluwer Academic Press: Dordrecht, 1995.

[7] Hunter C.N., T. M. B. J., Daldal F. *The Purple Phototrophic Bacteria*; Springer: Dordrecht, 2008.

[8] D.A., B. *The Molecular Biology of Cyanobacteria*; Kluwer Academic Press: Dordrecht, 1994.

[9] L., M. *Symbiosis in Cell Evolution: Microbial Cummunities in the Archean and Proterozoic Eons*; W. H. Freeman: San Francisco, 1993.

[10] Keeling, P. J. *Philosophical Transactions of the Royal Society B-biological Sciences* **2010**, *365*, 729–748.

[11] Wydrzynski T.J., S. K. *Photosystem II: The Light-Driven Water: Plastoquinone Oxidoreductase*; Springer: Dordrecht, 2005.

[12] Nelson, N.; Yocum, C. F. *Annual Review of Plant Biology* **2006**, *57*, 521–565.

[13] Dekker, J.; Boekema, E. *Biochimica Et Biophysica Acta-bioenergetics* **2005**, *1706*, 12–39.

[14] Wei, X.; Su, X.; Cao, P.; Liu, X.; Chang, W.; Li, M.; Zhang, X.; Liu, Z. *Nature* **2016**, *534*, 69+.

[15] Vinyard, D. J.; Ananyev, G. M.; Dismukes, G. C. In *Annual Review of Biochemistry, Vol 82*; Kornberg, RD,, Ed.; Annual Review of Biochemistry; 2013; Vol. 82; pp 577–606.

[16] Debus, R. *Biochimica Et Biophysica Acta-bioenergetics* **1992**, *1102*, 269–352.

[17] Styring, S.; Sjoholm, J.; Mamedov, F. *Biochimica Et Biophysica Acta-bioenergetics* **2012**, *1817*, 76–87.

[18] Baniulis, D.; Yamashita, E.; Zhang, H.; Hasan, S. S.; Cramer, W. A. *Photochemistry and Photobiology* **2008**, *84*, 1349–1358.

[19] E.L., G. *Plastocyanin: Structure, Location, Diffusion and Electron Transfer Mechanism. In: Oxygenic Photosynthesis: The Light Reactions*; Kluwer Academic Press: Dordrecht, 1996.

[20] Haehnel, W.; Ratajczak, R.; Robenek, H. *Journal of Cell Biology* **1989**, *108*, 1397–1405.

[21] Holzwarth, A.; Muller, M.; Niklas, J.; Lubitz, W. *Biophysical Journal* **2006**, *90*, 552–565.

[22] Golbeck, J. *Photosynthesis Research* **1999**, *61*, 107–144.

[23] D.B., K. *Ferredoxin and ferredoxin-dependent enzymes. In: Oxygenic Photosynthesis: The Light Reactions*; Kluwer Academic Press: Dordrecht, 1996.

[24] Collins A.M., B. R., Wen J. *Photo-synthetic Light Harvesting Complexes*; Royal Soc. of Chemistry: Cambridge, 2012.

[25] T., F. *Annalytical Physics* **1948**, *437*, 55–75.

[26] H., S. *Chlorophylls*; CRC Press: Boca Raton, Fl, 1991.

[27] M., G. *J. Molec. Spectroscopy* **1961**, *3*, 138–163.

[28] Frank H., B. G. C. R., Young A.J. *The Photochemistry of Carotenoids: Applications in Biology*; Kluwer Academic Press: Dordrecht, 2000.

[29] Polivka T., F. H. *Acc. Chem. Res.* **2010**, *43*, 1125–1134.

[30] van Amerongen, H.; van Grondelle, R. *Journal of Physical Chemistry B* **2001**, *105*, 604–617.

[31] Oustromov E.E., C. R. S. G., Mulvaney R.M. *Science* **2013**, *340*, 52–56.

[32] Sundstrom, V.; Pullerits, T.; van Grondelle, R. *Journal of Physical Chemistry B* **1999**, *103*, 2327–2346.

[33] Cogdell, R. J.; Gall, A.; Koehler, J. *Quarterly Reviews of Biophysics* **2006**, *39*, 227–324.

[34] van Grondell R. Novoderezhkin V.I., *Spectroscopy and dynamics of excitation transfer and trapping in purple bacteria. In: The Purple Phototrophic Bacteria*; Springer: Dordrecht, 2009.

[35] Fleming, G.; vanGrondelle, R. *Current Opinion in Structural Biology* **1997**, *7*, 738–748.

[36] Polivka, T.; Frank, H. A. *Accounts of Chemical Research* **2010**, *43*, 1125–1134.

[37] Harel, E.; Engel, G. S. *Proceedings of the National Academy of Sciences of the United States of America* **2012**, *109*, 706–711.

[38] Hildner, R.; Brinks, D.; Nieder, J. B.; Cogdell, R. J.; van Hulst, N. F. *Science* **2013**, *340*, 1448–1451.

[39] Bautista, J.; Hiller, R.; Sharples, F.; Gosztola, D.; Wasielewski, M.; Frank, H. *Journal of Physical Chemistry a* **1999**, *103*, 2267–2273.

[40] Rhee, K.; Morriss, E.; Barber, J.; Kuhlbrandt, W. *Nature* **1998**, *396*, 283–286.

[41] KUHLBRANDT, W.; WANG, D.; FUJIYOSHI, Y. *Nature* **1994**, *367*, 614–621.

[42] Liu, Z.; Yan, H.; Wang, K.; Kuang, T.; Zhang, J.; Gui, L.; An, X.; Chang, W. *Nature* **2004**, *428*, 287–292.

[43] Bassi, R.; Sandona, D.; Croce, R. *Physiologia Plantarum* **1997**, *100*, 769–779.

[44] Caffarri, S.; Passarini, F.; Bassi, R.; Croce, R. *FEBS Letters* **2007**, *581*, 4704–4710.

[45] Caffarri, S.; Tibiletti, T.; Jennings, R. C.; Santabarbara, S. *Current Protein & Peptide Science* **2014**, *15*, 296–331.

[46] Novoderezhkin, V.; Palacios, M.; van Amerongen, H.; van Grondelle, R. *Journal of Physical Chemistry B* **2004**, *108*, 10363–10375.

[47] Novoderezhkin, V.; Palacios, M.; van Amerongen, H.; van Grondelle, R. *Journal of Physical Chemistry B* **2005**, *109*, 10493–10504.

[48] Mozzo, M.; Passarini, F.; Bassi, R.; van Amerongen, H.; Croce, R. *Biochimica Et Biophysica Acta-bioenergetics* **2008**, *1777*, 1263–1267.

[49] Mueh, F.; Lindorfer, D.; Busch, M. S. A.; Renger, T. *Physical Chemistry Chemical Physics* **2014**, *16*, 11848–11863.

[50] Powles, S. *Annual Review of Plant Physiology and Plant Molecular Biology* **1984**, *35*, 15–44.

[51] Barber, J. *Australian Journal of Plant Physiology* **1995**, *22*, 201–208.

[52] Telfer, A.; He, W.; Barber, J. *Biochimica Et Biophysica Acta-bioenergetics* **1990**, *1017*, 143–151.

[53] Ohad, I.; Kyle, D.; Arntzen, C. *Journal of Cell Biology* **1984**, *99*, 481–485.

[54] Ruban, A. V.; Johnson, M. P.; Duffy, C. D. P. *Biochimica Et Biophysica Acta-bioenergetics* **2012**, *1817*, 167–181.

[55] Koller, D. *Plant Cell and Environment* **1990**, *13*, 615–632.

[56] Chow, W.; Anderson, J.; Hope, A. *Photosynthesis Research* **1988**, *17*, 277–281.

[57] Kloppstech, K. *Physiologia Plantarum* **1997**, *100*, 739–747.

[58] Pospisil, P. *Biochimica Et Biophysica Acta-bioenergetics* **2012**, *1817*, 218–231.

[59] Croce, R.; Weiss, S.; Bassi, R. *Journal of Biological Chemistry* **1999**, *274*, 29613–29623.

[60] Weis, E.; Berry, J. *Biochimica Et Biophysica Acta-bioenergetics* **1987**, *894*, 198–208.

[61] Wraight, C.; Crofts, A. *European Journal of Biochemistry* **1970**, *17*, 319–&.

[62] Belgio, E.; Johnson, M. P.; Juric, S.; Ruban, A. V. *Biophysical Journal* **2012**, *102*, 2761–2771.

[63] Genty, B.; Briantais, J.; Baker, N. *Biochimica Et Biophysica Acta-bioenergetics* **1989**, *990*, 87–92.

[64] Schreiber, U. *Photosynthesis Research* **1986**, *9*, 261–272.

[65] Ruban, A. V.; Johnson, M. P. *Photosynthesis Research* **2009**, *99*, 173–183.

[66] Allen, J.; Forsberg, J. *Trends in Plant Science* **2001**, *6*, 317–326.

[67] Horton, P.; Ruban, A. *Photosynthesis Research* **1992**, *34*, 375–385.

[68] Horton, P.; Ruban, A.; Walters, R. *Annual Review of Plant Physiology and Plant Molecular Biology* **1996**, *47*, 655–684.

[69] Oxborough, K.; Horton, P. *Biochimica et Biophysica Acta* **1988**, *934*, 135–143.

[70] Krause, G. *Biochimica Et Biophysica Acta-bioenergetics* **1974**, *333*, 301–313.

[71] Krause, G.; Weis, E. *Annual Review of Plant Physiology and Plant Molecular Biology* **1991**, *42*, 313–349.

[72] Krieger, A.; Moya, I.; Weis, E. *Biochimica Et Biophysica Acta-bioenergetics* **1992**, *1102*, 167–176.

[73] Mullineaux, C.; Ruban, A.; Horton, P. *Biochimica Et Biophysica Acta-bioenergetics* **1994**, *1185*, 119–123.

[74] Ruban, A.; Young, A.; Horton, P. *Biochemistry* **1996**, *35*, 674–678.

[75] Ballottari, M.; Girardon, J.; Betterle, N.; Morosinotto, T.; Bassi, R. *Journal of Biological Chemistry* **2010**, *285*, 28309–28321.

[76] Andersson, J.; Walters, R.; Horton, P.; Jansson, S. *Plant Cell* **2001**, *13*, 1193–1204.

[77] Kovacs, L.; Damkjaer, J.; Kereiche, S.; Ilioaia, C.; Ruban, A. V.; Boekema, E. J.; Jansson, S.; Horton, P. *Plant Cell* **2006**, *18*, 3106–3120.

[78] de Bianchi, S.; Dall'Osto, L.; Tognon, G.; Morosinotto, T.; Bassi, R. *Plant Cell* **2008**, *20*, 1012–1028.

[79] Jahns, P.; Junge, W. *European Journal Of Biochemistry* **1990**, *193*, 731–736.

[80] Betterle, N.; Ballottari, M.; Zorzan, S.; de Bianchi, S.; Cazzaniga, S.; Dall'Osto, L.; Morosinotto, T.; Bassi, R. *Journal of Biological Chemistry* **2009**, *284*, 15255–15266.

[81] Johnson, M. P.; Goral, T. K.; Duffy, C. D. P.; Brain, A. P. R.; Mullineaux, C. W.; Ruban, A. V. *Plant Cell* **2011**, *23*, 1468–1479.

[82] Demmigadams, B. *Biochimica Et Biophysica Acta-bioenergetics* **1990**, *1020*, 1–24.

[83] Eskling, M.; Arvidsson, P.; Akerlund, H. *Physiologia Plantarum* **1997**, *100*, 806–816.

[84] Demmigadams, B.; Winter, K.; Kruger, A.; Czygan, F. *Plant Physiology* **1989**, *90*, 881–886.

[85] Demmigadams, B.; Winter, K.; Kruger, A.; Czygan, F. *Plant Physiology* **1989**, *90*, 894–898.

[86] Rees, D.; Noctor, G.; Ruban, A.; Crofts, J.; Young, A.; Horton, P. *Photosynthesis Research* **1992**, *31*, 11–19.

[87] Horton, P.; Ruban, A.; Wentworth, M. *Philosophical Transactions of the Royal Society of London Series B-Biological Sciences* **2000**, *355*, 1361–1370.

[88] Ruban, A.; Horton, P.; Young, A. *Journal of Photochemistry and Photobiology B-biology* **1993**, *21*, 229–234.

[89] Ruban, A.; Horton, P. *Plant Physiology* **1999**, *119*, 531–542.

[90] Horton, P.; Wentworth, M.; Ruban, A. *FEBS Letters* **2005**, *579*, 4201–4206.

[91] Funk, C.; Schroder, W.; Napiwotzki, A.; Tjus, S.; Renger, G.; Andersson, B. *Biochemistry* **1995**, *34*, 11133–11141.

[92] Funk, C.; Adamska, I.; Green, B.; Andersson, B.; Renger, G. *Journal of Biological Chemistry* **1995**, *270*, 30141–30147.

[93] Fan, M.; Li, M.; Liu, Z.; Cao, P.; Pan, X.; Zhang, H.; Zhao, X.; Zhang, J.; Chang, W. *Nature Structural & Molecular Biology* **2015**, *22*, 729–U115.

[94] Li, X.; Gilmore, A.; Niyogi, K. *Journal of Biological Chemistry* **2002**, *277*, 33590–33597.

[95] Kiss, A. Z.; Ruban, A. V.; Horton, P. *Journal of Biological Chemistry* **2008**, *283*, 3972–3978.

[96] Teardo, E.; de laureto, P. P.; Bergantino, E.; Dalla Vecchia, F.; Rigoni, F.; Szabo, D.; Giacometti, G. M. *Biochimica Et Biophysica Acta-bioenergetics* **2007**, *1767*, 703–711.

[97] Dominici, P.; Caffarri, S.; Armenante, F.; Ceoldo, S.; Crimi, M.; Bassi, R. *Journal of Biological Chemistry* **2002**, *277*, 22750–22758.

[98] Ruban, A.; Young, A.; Horton, P. *Biochimica Et Biophysica Acta-bioenergetics* **1994**, *1186*, 123–127.

[99] Barber, J.; Mills, J.; Nicolson, J. *FEBs Letters* **1974**, *49*, 106–110.

[100] Ruban, A.; Young, A.; Pascal, A.; Horton, P. *Plant Physiology* **1994**, *104*, 227–234.

[101] Kramer, D.; Sacksteder, C.; Cruz, J. *Photosynthesis Research* **1999**, *60*, 151–163.

[102] Dall'Osto, L.; Caffarri, S.; Bassi, R. *Plant Cell* **2005**, *17*, 1217–1232.

[103] Johnson, M. P.; Ruban, A. V. *Journal of Biological Chemistry* **2009**, *284*, 23592–23601.

[104] Gilmore, A.; Hazlett, T.; Govindjee, *Proceedings of the National Academy of Sciences of the United States of America* **1995**, *92*, 2273–2277.

[105] Miloslavina, Y.; Wehner, A.; Lambrev, P. H.; Wientjes, E.; Reus, M.; Garab, G.; Croce, R.; Holzwarth, A. R. *FEBS Letters* **2008**, *582*, 3625–3631.

[106] Ma, Y.; Holt, N.; Li, X.; Niyogi, K.; Fleming, G. *Proceedings of the National Academy of Sciences of the United States of America* **2003**, *100*, 4377–4382.

[107] Liao, P.-N.; Holleboom, C.-P.; Wilk, L.; Kuehlbrandt, W.; Walla, P. J. *Journal of Physical Chemistry B* **2010**, *114*, 15650–15655.

[108] Dreuw, A.; Fleming, G.; Head-Gordon, M. *Biochemical Society Transactions* **2005**, *33*, 858–862.

[109] Holt, N.; Zigmantas, D.; Valkunas, L.; Li, X.; Niyogi, K.; Fleming, G. *Science* **2005**, *307*, 433–436.

[110] Avenson, T. J.; Ahn, T. K.; Zigmantas, D.; Niyogi, K. K.; Li, Z.; Ballottari, M.; Bassi, R.; Fleming, G. R. *Journal of Biological Chemistry* **2008**, *283*, 3550–3558.

[111] Ahn, T. K.; Avenson, T. J.; Ballottari, M.; Cheng, Y.-C.; Niyogi, K. K.; Bassi, R.; Fleming, G. R. *Science* **2008**, *320*, 794–797.

[112] Ruban, A. V.; Berera, R.; Ilioaia, C.; van Stokkum, I. H. M.; Kennis, J. T. M.; Pascal, A. A.; van Amerongen, H.; Robert, B.; Horton, P.; van Grondelle, R. *Nature* **2007**, *450*, 575–U22.

[113] L., D. D. *Journal of Chemical Physics* **1953**, *21*, 836–850.

[114] Mueller, M. G.; Lambrev, P.; Reus, M.; Wientjes, E.; Croce, R.; Holzwarth, A. R. *Chemphyschem* **2010**, *11*, 1289–1296.

[115] Ruban, A.; Rees, D.; Noctor, G.; Young, A.; Horton, P. *Biochimica Et Biophysica Acta-bioenergetics* **1991**, *1059*, 355–360.

[116] Ruban, A.; Horton, P. *Biochimica Et Biophysica Acta-bioenergetics* **1992**, *1102*, 30–38.

[117] Born, M.; Oppenheimer, R. *Annalen der Physik* **1927**, *389*, 457–484.

[118] Schrödinger, E. *Annalen der Physik* **1926**, *384*, 361–376.

[119] Pauli, W. *Zeitschrift für Physik* **1925**, *31*, 765–783.

[120] Slater, J. C. *Phys. Rev.* **1929**, *34*, 1293–1322.

[121] Hartree, D. R. *Mathematical Proceedings of the Cambridge Philosophical Society* **1928**, *24*, 89–110.

[122] Fock, V. *Zeitschrift für Physik* **1930**, *61*, 126–148.

[123] Fock, V. *Zeitschrift für Physik* **1930**, *62*, 795–805.

[124] Roothaan, C. C. J. *Rev. Mod. Phys.* **1951**, *23*, 69–89.

[125] Sherrill, C. D.; Schaefer, H. F. In *The Configuration Interaction Method: Advances in Highly Correlated Approaches*; Löwdin, P.-O., Sabin, J. R., Zerner, M. C., Brändas, E., Eds.; Advances in Quantum Chemistry; Academic Press, 1999; Vol. 34; pp 143 – 269.

[126] Hegarty, D.; Robb, M. *MOLECULAR PHYSICS* **1979**, *38*, 1795–1812.

[127] Buenker, R. J.; Peyerimhoff, S. D.; Butscher, W. *Molecular Physics* **1978**, *35*, 771–791.

[128] Hohenberg, P.; Kohn, W. *Phys. Rev.* **1964**, *136*, B864–B871.

[129] Kohn, W.; Sham, L. J. *Phys. Rev.* **1965**, *140*, A1133–A1138.

[130] Kohn, W.; Sham, L. J. *Phys. Rev.* **1965**, *140*, A1133–A1138.

[131] Parr, R. G. In *Horizons of Quantum Chemistry*; Fukui, K., Pullman, B., Eds.; Springer Netherlands: Dordrecht, 1980; pp 5–15.

[132] Becke, A. D. *Phys. Rev. A* **1988**, *38*, 3098–3100.

[133] Lee, C.; Yang, W.; Parr, R. G. *Phys. Rev. B* **1988**, *37*, 785–789.

[134] Miehlich, B.; Savin, A.; Stoll, H.; Preuss, H. *Chemical Physics Letters* **1989**, *157*, 200 – 206.

[135] Adamo, C.; Barone, V. *The Journal of Chemical Physics* **1998**, *108*, 664–675.

[136] Perdew, J. P. *Electronic Structure of Solids*; Ed. P. Ziesche and H. Eschrig: Akademie Verlag, Berlin, 1991.

[137] Perdew, J. P.; Burke, K.; Ernzerhof, M. *Phys. Rev. Lett.* **1996**, *77*, 3865–3868.

[138] Tao, J.; Perdew, J. P.; Staroverov, V. N.; Scuseria, G. E. *Phys. Rev. Lett.* **2003**, *91*, 146401.

[139] Bauernschmitt, R.; Ahlrichs, R. *Chemical Physics Letters* **1996**, *256*, 454 – 464.

[140] Spezia, R.; Knecht, S.; Mennucci, B. *Physical Chemistry Chemical Physics* **2017**, *19*, 17156–17166.

[141] Hückel, E. *Zeitschrift fur Physik* **1931**, *70*, 204–286.

[142] Hückel, E., *Zeitschrift für Physik* **1930**, *60*, 423–456.

[143] Pariser, R.; Parr, R. G. *The Journal of Chemical Physics* **1953**, *21*, 466–471.

[144] Pariser, R.; Parr, R. G. *The Journal of Chemical Physics* **1953**, *21*, 767–776.

[145] Pople, J. A. *Trans. Faraday Soc.* **1953**, *49*, 1375–1385.

[146] Pople, J.; Beveridge, D. *McGraw–Hill* **1970**,

[147] Dewar, M. J. S.; Thiel, W. *Journal of the American Chemical Society* **1977**, *99*, 4899–4907.

[148] Ridley, J.; Zerner, M. *Theoretica chimica acta* **1973**, *32*, 111–134.

[149] Dewar, M. J. S.; Zoebisch, E. G.; Healy, E. F.; Stewart, J. J. P. *Journal of the American Chemical Society* **1985**, *107*, 3902–3909.

[150] Anders, E.; Koch, R.; Freunscht, P. *Journal of Computational Chemistry* **1993**, *14*, 1301–1312.

[151] Kusumoto, T.; Kosumi, D.; Uragami, C.; Frank, H. A.; Birge, R. R.; Cogdell, R. J.; Hashimoto, H. *Journal of Physical Chemistry A* **2011**, *115*, 2110–2119.

[152] Macernis, M.; Sulskus, J.; Duffy, C. D. P.; Ruban, A. V.; Valkunas, L. *Journal of Physical Chemistry A* **2012**, *116*, 9843–9853.

[153] Dapprich, S.; Komáromi, I.; Byun, K.; Morokuma, K.; Frisch, M. *Journal of Molecular Structure* **1999**, *462*, 1–21.

[154] Vreven, T.; Morokuma, K.; Farkas, O.; Schlegel, H.; Frisch, M. *Journal of Computational Chemistry* **2003**, *24*, 760–769.

[155] Vreven, T.; Byun, K.; Komáromi, I.; Dapprich, S.; Montgomery Jr., J.; Morokuma, K.; Frisch, M. *Journal of Chemical Theory and Computation* **2006**, *2*, 815–26.

[156] Frenkel, J. *Phys. Rev.* **1931**, *37*, 17–44.

[157] Ghosh, P. N. *Solid State Communications* **1976**, *19*, 639 – 642.

[158] Krueger, B. P.; Scholes, G. D.; Fleming, G. R. *The Journal of Physical Chemistry B* **1998**, *102*, 5378–5386.

[159] Redfield, A. In *Advances in Magnetic Resonance*; Waugh, J. S., Ed.; Advances in Magnetic and Optical Resonance; Academic Press, 1965; Vol. 1; pp 1 – 32.

[160] Britton, L.-J. S. P. H., G. *In Carotenoids*; Birkhäuser Verlag: Basel, 1995.

[161] Polivka, T.; Sundstrom, V. *Chemical Reviews* **2004**, *104*, 2021–2071.

[162] Schlucker, S.; Szeghalmi, A.; Schmitt, M.; Popp, J.; Kiefer, W. *Journal of Raman Spectroscopy* **2003**, *34*, 413–419.

[163] Hemley, R.; Kohler, B. *Biophysical Journal* **1977**, *20*, 377–382.

[164] Christensen, R.; Goyette, M.; Gallagher, L.; Duncan, J.; DeCoster, B.; Lugtenburg, J.; Jansen, F.; van der Hoef, I. *Journal of Physical Chemistry A* **1999**, *103*, 2399–2407.

[165] Cosgrove, S.; Guite, M.; Burnell, T.; Christensen, R. *Journal of Physical Chemistry* **1990**, *94*, 8118–8124.

[166] Decoster, B.; Christensen, R.; Gebhard, R.; Lugtenburg, J.; Farhoosh, R.; Frank, H. *Biochimica Et Biophysica Acta-bioenergetics* **1992**, *1102*, 107–114.

[167] Chynwat, V.; Frank, H. *Chemical Physics* **1995**, *194*, 237–244.

[168] Shima, S.; Ilagan, R.; Gillespie, N.; Sommer, B.; Hiller, R.; Sharples, F.; Frank, H.; Birge, R. *Journal of Physical Chemistry A* **2003**, *107*, 8052–8066.

[169] Polivka, T.; Herek, J.; Zigmantas, D.; Akerlund, H.; Sundstrom, V. *Proceedings of the National Academy of Sciences of the United States of America* **1999**, *96*, 4914–4917.

[170] Andersson, P.; Bachilo, S.; Chen, R.; Gillbro, T. *Journal of Physical Chemistry* **1995**, *99*, 16199–16209.

[171] Hashimoto, H.; Koyama, Y.; Hirata, Y.; Mataga, N. *Journal of Physical Chemistry* **1991**, *95*, 3072–3076.

[172] Sashima, T.; Nagae, H.; Kuki, M.; Koyama, Y. *Chemical Physics Letters* **1999**, *299*, 187–194.

[173] Frank, H.; Cua, A.; Chynwat, V.; Young, A.; Gosztola, D.; Wasielewski, M. *Photosynthesis Research* **1994**, *41*, 389–395.

[174] Zimmermann, J.; Linden, P.; Vaswani, H.; Hiller, R.; Fleming, G. *Journal of Physical Chemistry B* **2002**, *106*, 9418–9423.

[175] Walla, P.; Linden, P.; Hsu, C.; Scholes, G.; Fleming, G. *Proceedings of the National Academy of Sciences of the United States of America* **2000**, *97*, 10808–10813.

[176] Walla, P.; Linden, P.; Ohta, K.; Fleming, G. *Journal of Physical Chemistry A* **2002**, *106*, 1909–1916.

[177] Walla, P.; Yom, J.; Krueger, B.; Fleming, G. *Journal of Physical Chemistry B* **2000**, *104*, 4799–4806.

[178] Fox, K. F.; Bricker, W. P.; Lo, C.; Duffy, C. D. P. *Journal of Physical Chemistry B* **2015**, *119*, 15550–15560.

[179] Duffy, C. D. P.; Chmeliov, J.; Macernis, M.; Sulskus, J.; Valkunas, L.; Ruban, A. V. *Journal of Physical Chemistry B* **2013**, *117*, 10974–10986.

[180] Chmeliov, J.; Bricker, W. P.; Lo, C.; Jouin, E.; Valkunas, L.; Ruban, A. V.; Duffy, C. D. P. *Physical Chemistry Chemical Physics* **2015**, *17*, 15857–15867.

[181] Balevicius, V., Jr.; Abramavicius, D.; Polivka, T.; Pour, A. G.; Hauer, J. *Journal of Physical Chemistry Letters* **2016**, *7*, 3347–3352.

[182] Ruban, A.; Pascal, A.; Robert, B.; Horton, P. *Journal of Biological Chemistry* **2001**, *276*, 24862–24870.

[183] Gradinaru, C.; Kennis, J.; Papagiannakis, E.; van Stokkum, I.; Cogdell, R.; Fleming, G.; Niederman, R.; van Grondelle, R. *Proceedings Of The National Academy Of Sciences Of The United States Of America* **2001**, *98*, 2364–2369.

[184] Chabera, P.; Fuciman, M.; Hribek, P.; Polivka, T. *Physical Chemistry Chemical Physics* **2009**, *11*, 8795–8803.

[185] Tavan, P.; Schulten, K. *Physical Review B* **1987**, *36*, 4337–4358.

[186] Polivka, T.; Zigmantas, D.; Frank, H.; Bautista, J.; Herek, J.; Koyama, Y.; Fujii, R.; Sundstrom, V. *Journal of Physical Chemistry B* **2001**, *105*, 1072–1080.

[187] Sashima, T.; Koyama, Y.; Yamada, T.; Hashimoto, H. *Journal of Physical Chemistry B* **2000**, *104*, 5011–5019.

[188] Barros, T.; Royant, A.; Standfuss, J.; Dreuw, A.; Kuhlbrandt, W. *EMBO Journal* **2009**, *28*, 298–306.

[189] Ilioaia, C.; Johnson, M. P.; Horton, P.; Ruban, A. V. *Journal of Biological Chemistry* **2008**, *283*, 29505–29512.

[190] Kruger, T. P. J.; Novoderezhkin, V. I.; Ilioaia, C.; van Grondelle, R. *Biophysical Journal* **2010**, *98*, 3093–3101.

[191] Yan, H.; Zhang, P.; Wang, C.; Liu, Z.; Chang, W. *Biochemical and Biophysical Research Communications* **2007**, *355*, 457–463.

[192] Pandit, A.; Morosinotto, T.; Reus, M.; Holzwarth, A. R.; Bassi, R.; de Groot, H. J. M. *Biochimica Et Biophysica Acta-bioenergetics* **2011**, *1807*, 437–443.

[193] Pascal, A.; Liu, Z.; Broess, K.; van Oort, B.; van Amerongen, H.; Wang, C.; Horton, P.; Robert, B.; Chang, W.; Ruban, A. *Nature* **2005**, *436*, 134–137.

[194] Kroener, D.; Goetze, J. P. *Journal of Photochemistry and Photobiology B-biology* **2012**, *109*, 12–19.

[195] Goetze, J. P.; Kroener, D.; Banerjee, S.; Karasulu, B.; Thiel, W. *Chemphyschem* **2014**, *15*, 3391–3400.

[196] Dreuw, A.; Fleming, G.; Head-Gordon, M. *Physical Chemistry Chemical Physics* **2003**, *5*, 3247–3256.

[197] Dreuw, A. *Journal of Physical Chemistry A* **2006**, *110*, 4592–4599.

[198] Balevicius, V., Jr.; Fox, K. F.; Bricker, W. P.; Jurinovich, S.; Prandi, I. G.; Mennucci, B.; Duffy, C. D. P. *Scientific Reports* **2017**, *7*, 13956.

[199] Beddard, G.; Porter, G. *Nature* **1976**, *260*, 366–367.

[200] Frank, H. A.; Bautista, J. A.; Josue, J. S.; Young, A. J. *Biochemistry* **2000**, *39*, 2831–2837.

[201] Polivka, T.; Herek, J. L.; Zigmantas, D.; Akerlund, H.-E.; Sundstrom, V. *Proceedings of the National Academy of Sciences* **1999**, *96*, 4914–4917.

[202] Polivka, T.; Zigmantas, D.; Sundstrom, V.; Formaggio, E.; Cinque, G.; Bassi, R. *Biochemistry* **2002**, *41*, 439–450.

[203] Liao, P.-N.; Bode, S.; Wilk, L.; Hafi, N.; Walla, P. J. *Chemical Physics* **2010**, *373*, 50–55.

[204] Bode, S.; Quentmeier, C. C.; Liao, P.-N.; Hafi, N.; Barros, T.; Wilk, L.; Bittner, F.; Walla, P. J. *Proceedings of the National Academy of Sciences of the United States of America* **2009**, *106*, 12311–12316.

[205] Amarie, S.; Standfuss, J.; Barros, T.; Kuehlbrandt, W.; Dreuw, A.; Wachtveitl, J. *Journal of Physical Chemistry B* **2007**, *111*, 3481–3487.

[206] Amarie, S.; Wilk, L.; Barros, T.; Kühlbrandt, W.; Dreuw, A.; Wachtveitl, J. *Biochimica et Biophysica Acta - Bioenergetics* **2009**, *1787*, 747 – 752.

[207] Avenson, T. J.; Ahn, T. K.; Niyogi, K. K.; Ballottari, M.; Bassi, R.; Fleming, G. R. *Journal of Biological Chemistry* **2009**, *284*, 2830–2835.

[208] Li, Z.; Ahn, T. K.; Avenson, T. J.; Ballottari, M.; Cruz, J. A.; Kramer, D. M.; Bassi, R.; Fleming, G. R.; Keasling, J. D.; Niyogi, K. K. *The Plant Cell* **2009**, *21*, 1798–1812.

[209] van Amerongen, H.; van Grondelle, R.; Valkunas, L. *Photosynthetic Excitons*; World Scientific, 2000.

[210] van Oort, B.; Roy, L. M.; Xu, P.; Lu, Y.; Karcher, D.; Bock, R.; Croce, R. *The Journal of Physical Chemistry Letters* **2018**, *9*, 346–352.

[211] Miloslavina, Y.; de Bianchi, S.; Dall'Osto, L.; Bassi, R.; Holzwarth, A. R. *Journal of Biological Chemistry* **2011**, *286*, 36830–36840.

[212] Holleboom, C.-P.; Gacek, D. A.; Liao, P.-N.; Negretti, M.; Croce, R.; Walla, P. J. *Photosynthesis Research* **2015**, *124*, 171–180.

[213] Dall'Osto, L.; Cazzaniga, S.; Bressan, M.; Palecek, D.; Zidek, K.; Niyogi, K. K.; Fleming, G. R.; Zigmantas, D.; Bassi, R. *Nature Plants* **2017**, *3*, 17033.

[214] Holzwarth, A. R.; Miloslavina, Y.; Nilkens, M.; Jahns, P. *Chemical Physics Letters* **2009**, *483*, 262–267.

[215] Belgio, E.; Kapitonova, E.; Chmeliov, J.; Duffy, C. D. P.; Ungerer, P.; Valkunas, L.; Ruban, A. V. *Nature Communications* **2014**, *5*, 4433.

[216] van Oort, B.; van Hoek, A.; Ruban, A. V.; van Amerongen, H. *FEBS Letters* **2007**, *581*, 3528–3532.

[217] van Oort, B.; van Hoek, A.; Ruban, A. V.; van Amerongen, H. *Journal of Physical Chemistry B* **2007**, *111*, 7631–7637.

[218] Palacios, M.; Frese, R.; Gradinaru, C.; van Stokkum, I.; Premvardhan, L.; Horton, P.; Ruban, A.; van Grondelle, R.; van Amerongen, H. *Biochimica Et Biophysica Acta-bioenergetics* **2003**, *1605*.

[219] Creemers, T.; De Caro, C.; Visschers, R.; van Grondelle, R.; Volker, S. *Journal Of Physical Chemistry B* **1999**, *103*, 9770–9776.

[220] Chmeliov, J.; Valkunas, L.; Krueger, T. P. J.; Ilioaia, C.; van Grondelle, R. *New Journal of Physics* **2013**, *15*.

[221] Pan, X.; Li, M.; Wan, T.; Wang, L.; Jia, C.; Hou, Z.; Zhao, X.; Zhang, J.; Chang, W. *Nature Structural & Molecular Biology* **2011**, *18*, 309–U94.

[222] Novoderezhkin, V.; Marin, A.; van Grondelle, R. *Physical Chemistry Chemical Physics* **2011**, *13*, 17093–17103.

[223] Mueh, F.; Renger, T. *Biochimica Et Biophysica Acta-bioenergetics* **2012**, *1817*, 1446–1460.

[224] Curutchet, C.; Mennucci, B. *Chemical Reviews* **2017**, *117*, 294–343.

[225] Prandi, I. G.; Viani, L.; Andreussi, O.; Mennucci, B. *Journal Of Computational Chemistry* **2016**, *37*, 981–991.

[226] Andreussi, O.; Knecht, S.; Marian, C. M.; Kongsted, J.; Mennucci, B. *Journal of Chemical Theory and Computation* **2015**, *11*, 655–666.

[227] Knox, R.; Spring, B. *Photochemistry And Photobiology* **2003**, *77*, 497–501.

[228] Polivka, T.; Zigmantas, D.; Sundstrom, V.; Formaggio, E.; Cinque, G.; Bassi, R. *Biochemistry* **2002**, *41*, 439–450.

[229] Josue, J.; Frank, H. *Journal Of Physical Chemistry A* **2002**, *106*, 4815–4824.

[230] Fox, K. F.; Balevicius, V., Jr.; Chmeliov, J.; Valkunas, L.; Ruban, A. V.; Duffy, C. D. P. *Physical Chemistry Chemical Physics* **2017**, *19*, 22957–22968.

[231] Liguori, N.; Periole, X.; Marrink, S. J.; Croce, R. *Scientific Reports* **2015**, *5*.

[232] van Oort, B.; Marechal, A.; Ruban, A. V.; Robert, B.; Pascal, A. A.; de Ruijter, N. C. A.; van Grondelle, R.; van Amerongen, H. *Physical Chemistry Chemical Physics* **2011**, *13*, 12614–12622.

[233] Bennett, D. I. G.; Amarnath, K.; Fleming, G. R. *Journal of the American Chemical Society* **2013**, *135*, 9164–9173.

[234] Staleva, H.; Komenda, J.; Shukla, M. K.; Slouf, V.; Kana, R.; Polivka, T.; Sobotka, R. *Nature Chemical Biology* **2015**, *11*, 287–U96.

[235] Johnson, M. P.; Perez-Bueno, M. L.; Zia, A.; Horton, P.; Ruban, A. V. *Plant Physiology* **2009**, *149*, 1061–1075.

[236] Belgio, E.; Duffy, C. D. P.; Ruban, A. V. *Physical Chemistry Chemical Physics* **2013**, *15*, 12253–12261.